



Zhu, Yu (2018) *Synthesis and characterisation of Zn₂NF*. MSc(R) thesis.

<https://theses.gla.ac.uk/8931/>

Copyright and moral rights for this work are retained by the author

A copy can be downloaded for personal non-commercial research or study, without prior permission or charge

This work cannot be reproduced or quoted extensively from without first obtaining permission in writing from the author

The content must not be changed in any way or sold commercially in any format or medium without the formal permission of the author

When referring to this work, full bibliographic details including the author, title, awarding institution and date of the thesis must be given

Enlighten: Theses

<https://theses.gla.ac.uk/>
research-enlighten@glasgow.ac.uk

Synthesis and characterisation of Zn_2NF



University of Glasgow | School of Chemistry

Yu Zhu

Materials Science and Engineering, BEng

Submitted in fulfilment of the requirements for the

Degree of Master of Science (R)

School of Chemistry

College of Science and Engineering

University of Glasgow

December 2017

Abstract

This work concerned the synthesis and characterisation of zinc nitride fluoride and an array of N, F co-doped ZnO materials. The synthesis of bulk Zn_2NF requires a high purity zinc nitride (Zn_3N_2) precursor, which is impossible to obtain commercially. For this reason, an important point of the project involved the synthesis of Zn_3N_2 by thermal ammonolysis of pure zinc powder. Compared to methods reported in literature, the synthetic reaction was improved by acting principally on the cooling phase of the reaction. Rapid quenching dramatically reduced the amount of impurities (mainly ZnO). The origin of the oxide impurities in Zn_3N_2 was also investigated and as point of this study. The interactions of molten zinc with ammonia were examined as synthesis parameters.

Zn_2NF was successfully synthesised, although no evidence of the previously reported low-temperature orthorhombic phase was observed. The pure material was obtained only when high-purity, oxygen-free atmospheres were used in the preparation. Despite the decrease in band gap compared to ZnO, the potential photocatalytic properties and performance of the material are negatively affected by oxidative reactions occurring in the presence of water, leading to the gradual formation of ZnO from Zn_2NF .

Doping procedures successfully reduced the band gap of ZnO, demonstrating that insertion of fluorine could be achieved more readily compared to nitrogen. Among the different procedures, ammonolysis of ZnF_2 or ZnO in combination with NH_4F led to the simultaneous inclusion of the two non-metals, in some cases altering the original crystal structure of ZnO.

Acknowledgement

Firstly, I would like to thank University of Glasgow giving me the chance study in the UK and doing research as well as Prof. Duncan H. Gregroy for his guidance and help over the past one year. It was really a great honour to study in this group and to learn so many skills and concepts. Meanwhile, a special thanks is due to Mr. Mauro Davide Cappelluti who gave me so much help in this year whether in experiment, study or daily life. Without him, this project would not have reached a conclusion. I learned a lot from him, not only the experiment skills, analysis knowledge and software operation, but also the spirit for doing research and how to face the difficulties in life.

I also want to thank to other group members for helping me during this year: Simon and Hallam for experiment operation, data analysis and thesis problems; Ayesha and Jawza for data analysis, and all other group members. The year I study in Glasgow is unforgettable and amazing. I will miss the time we spent together.

At last, let me thank all of you again and my friends and my family. Thank you so much for supporting me this year!

Summary

Synthesis and characterisation of Zn ₂ NF	1
Abstract.....	2
Acknowledgement	3
Chapter 1: Introduction	1
1.1 Nitride materials.....	1
1.1.2 Classification of nitride materials.....	2
1.1.3 Synthesis and applications of nitride materials	4
1.2 Nitride Halides	7
1.3 Zinc nitride	10
1.4 Zinc nitride halides.....	13
1.4.1 Zinc nitride fluorides	14
1.4.2 Nitride fluorides and doping.....	15
1.5 Photocatalytic materials	16
1.6 Objectives and scope of this work.....	18
Chapter 2: Experimental Methods.....	21
2.1 Ammonolysis reactions.....	21
2.2 Crystallography.....	22
2.2.1 PXRD.....	26
2.2.2 Rietveld Refinement	30
2.3 Scanning Electron Microscopy (SEM) and Energy Dispersive X-ray Spectroscopy (EDX)	34
2.3.1 Scanning Electron Microscopy	34
2.3.2 Energy Dispersive X-ray Spectroscopy (EDX)	37
2.4 UV-Vis Spectroscopy.....	37
2.4.1 Band gap measurement and calculation	38
2.4.2 UV-Vis absorbance of organic dye solutions.....	42
2.5 Thermal Analysis (TGA, DTG)	47
Chapter 3: Zinc nitride	52
3.1 Zinc nitride synthesis	52
3.1.1 ZnO re-crystallisation	59
3.1.2 Quenching/accelerated cooling.....	62
3.2 Morphological and elemental analysis	71
3.3 Band gap measurement.....	76
3.4 Zinc nitride Rietveld refinement	79
Chapter 4: Zinc nitride fluoride.....	82
4.1 Zinc nitride fluoride synthesis.....	82

4.2 Zn ₂ NF SEM and EDX	92
4.3 Zn ₂ NF thermal analysis.....	98
4.4 Optical properties	104
4.5 Zn ₂ NF photodegradation test	106
4.6 Zn ₂ NF refinement	112
Chapter 5: Doped-ZnO materials	115
5.1 Doped-ZnO materials synthesis and characterisation.....	115
5.2 Doped-ZnO materials: SEM and EDX analysis.....	123
5.3 Doped ZnO materials: band gap	126
Chapter 6: Conclusion and future work.....	130
6.1 Conclusion.....	130
6.2 Future work.....	132
Bibliography	134
Appendix	140

Chapter 1: Introduction

1.1 Nitride materials

The presence of nitrides as a distinct class of materials in solid-state chemistry is impossible to ignore, with different structures and properties that depend on the atoms associated with nitrogen in any given compound. Characterisation of nitrides has not been as exhaustive as for other classes of materials, such as oxides, with entire classes of nitrides still needing further investigation.^[1] The higher level of difficulty in the synthesis of nitrides compared to oxides, sulphides and halides is considered one of the main reasons of this incomplete characterisation. From a thermodynamic point of view, the N_2 triple bond has a binding energy of 941 kJ/mol, representing a much higher stability than an O_2 double bond (500 kJ/mol). Therefore, nitridation processes will generally require more energy for reactions to occur compared for example with oxidation reactions of similar elements.^[2] On the other hand, the decomposition of nitrides is much easier due to the lower free energy of formation compared with oxide counterparts. For instance, SiO_2 is stable at temperatures above 2000 °C when heated at atmospheric pressure, whereas Si_3N_4 decomposes at about 1900 °C under the same conditions. AlN decomposes at around 1800 °C, although Al_2O_3 can only be melted at 3000 °C.^[3] This characteristic of nitrides reduces the number of natural occurring compounds belonging to this class. Furthermore, considering the ionic forms, the N^{3-} anion requires more energy to form from atomic N (+2300 kJ/mol) than O^{2-} from atomic O (+700 kJ/mol) and S^{2-} from atomic S (+331 kJ/mol). These energetic values lead to a lower stability of nitrides compared to analogous types of oxides and sulphides containing the same elements.

Over the last several decades, academic studies and technological applications involving non-oxide materials have increasingly focused on nitride materials and their chemistry. Compounds like nitride-silicates, oxy-nitrides and nitride halides have gained more attention from both synthetic and property perspectives.^[4] Binary and ternary nitrides have been widely investigated and interestingly developed for industrial and technological applications.

1.1.2 Classification of nitride materials

Nitrides can be commonly classified in terms of how many elements form the respective compounds (eg. binary, ternary and quaternary) or by the class of the element with which they are associated (eg. alkali metals, halides, transition metals). In the following section, the most relevant compounds for sort of these classes are detailed.

Binary nitrides formed by alkali and alkaline earth metals, such as Li_3N and M_3N_2 ($\text{M} = \text{Ca}, \text{Be}, \text{Mg}$), can be considered as predominantly ionic compounds.⁴ The Li_3N structure was first reported in 1935 by Zintl and Brauer,^[5] while highly unstable Na_3N was firstly synthesized and reported only in 2002.^[6] Lithium nitride finds potential application in modified forms for lithium-ion battery technology, but is also used as a precursor for synthesis of ternary nitrides such as Li_3BN_2 and Li_3AlN_2 .^[7] Other alkali metals like K, Rb and Cs are not able to form stable nitrides, with their nitridation preferentially leading to azides (e.g. KN_3). Alkaline earth metal nitrides usually present an anti-bixbyite structure.^[8-10] Sr and Ba can also form as sub-nitrides of formula M_2N .

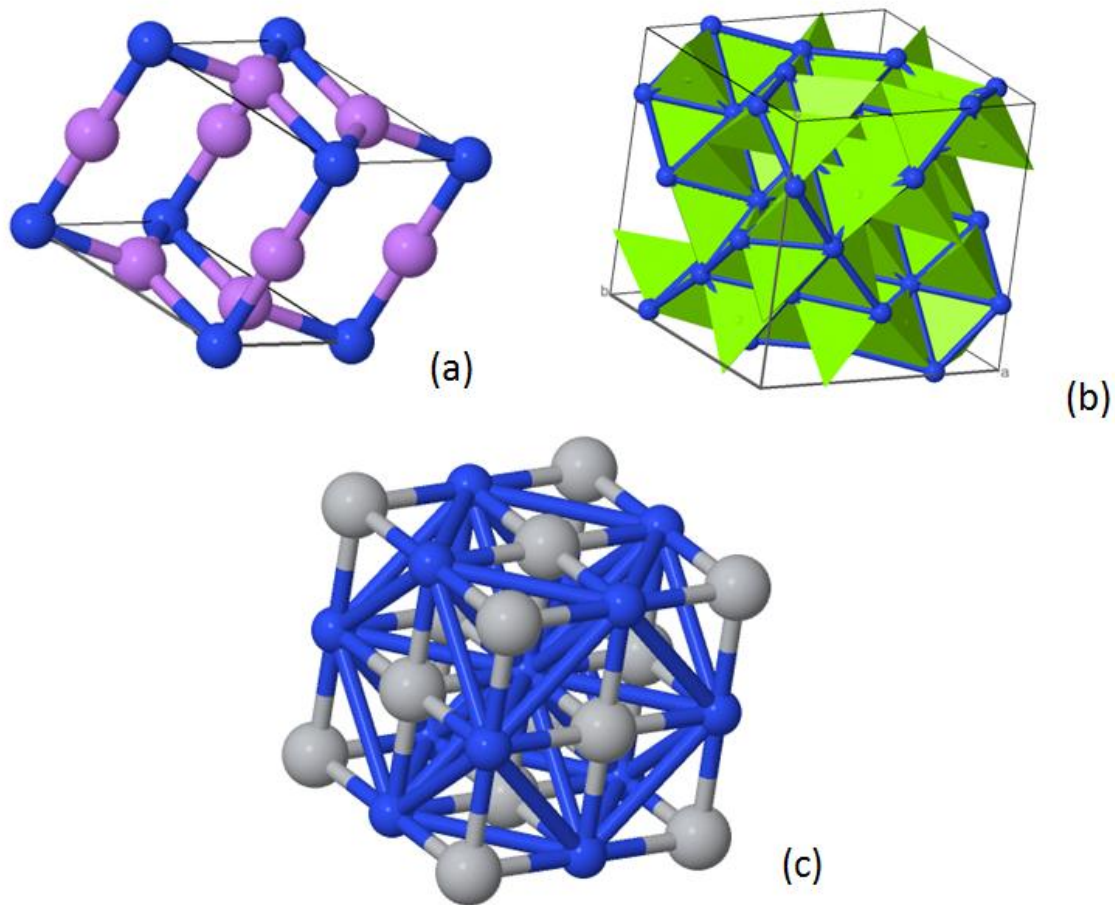


Figure 1.1: Example of nitride structures (a) Li_3N , (b) Mg_3N_2 , (c) TiN

Transition metal nitrides form mostly interstitial compounds in which an atom formed with a small enough radius occupies an interstitial hole in a metal lattice. Most of the early transition metal nitrides are reported as rock-salt structures described by the general formula MN ($\text{M}=\text{Ti}, \text{Cr}, \text{V}, \text{Nb}, \text{Hf}, \text{W}, \text{Ta}, \text{Zr}, \text{Mn}$). Other transition metals can form different structures such as anti-perovskite like M_4N ($\text{M}=\text{Fe}, \text{Mn}, \text{Ni}$) or anti-rutile structures, for example $\epsilon\text{-Ti}_2\text{N}$.^[11] Zn_3N_2 and Cd_3N_2 crystallise in the anti-bixbyite structure. However, not all transition metals can form stable nitrides. Heavier elements like $\text{Au}, \text{Pt}, \text{Tc}$ and Os are not reported to form nitrides whereas others are very unstable (eg. Ag_3N is explosive under certain conditions).^[4] Transition metal nitrides are probably the most interesting binary nitrides in terms of application. For

instance, TiN nanoparticles have been used in electrochemical applications as a cathode material.^[12] NbN and FeN have gained attention for their superconducting properties,^[13] whereas VN is important for its tribological properties, for example in composite films with Ag.^[14]

Ternary nitrides can be classified into two main categories: intermetallic and ionic/covalent compounds. Intermetallic nitrides are mainly formed by metal-metal interactions with nitrogen atoms, presenting a structure in which metal atoms constitute the framework and nitrogen atoms occupy interstitial positions. Conversely, ionic/covalent ternary nitrides present an opposite structure, with interstitial metal atoms or ions in a nitrogen or nitrate array. For lithium combined with group II elements, the formation of ternary nitride is facilitated with nitrogen atoms in the structure LiMN (M= Mg, Ca, Sr, Be). For example, LiBeN was firstly reported by Brice *et al.* and synthesized from Li₃N and Be₃N₂ under a nitrogen atmosphere at 580 °C.^[15] Then further nitrides with other alkaline metals were investigated, such as LiMgN, LiCaN and LiSrN, all with different crystal structures. Li₃N can also react with transition metals at high temperature forming intermetallic ternary compounds such as Li₅TiN₃, Li₇VN₄, Li₉CrN₅, Li₇MnN₄ and Li₃FeN₂,^[16] but also with p-block elements (Al, Ga, Si, P) forming ionic/covalent nitrides.^[17] Other binary nitrides such as Ca₃N₂ can react with several elements forming anti-perovskite structures Ca₃XN (X=P, As, Sb, Bi, Ge, Sn, Au, Pb).^[18] Reaction of Mg₃N₂ with p-block elements are also reported to form ionic/covalent compounds such as Mg₂PN₃, MgGeN₂ and Mg₃GaN₃.^[17]

1.1.3 Synthesis and applications of nitride materials

As already mentioned in the previous section, synthesis of binary nitrides generally requires more energy compared to other binary compounds such as

oxides or halides, mainly due to the energy barrier for the production of N^{3-} from N_2 . Synthesis reactions are also complicated by the adventitious presence of oxygen or water, which would both preferentially react with the starting materials rather than nitrogen, causing the formation of oxide or hydroxide impurities. For this reason, nitridation reactions should be performed in an oxygen-free atmosphere, such as a constant flow of inert gas or under vacuum. N_2 or NH_3 are often used as nitrogen sources for the synthesis of nitride materials. One of the most common synthesis procedures consists of the reaction of metal powders in the presence of these gases at high temperature producing binary nitrides. The reaction temperature and duration depend on the type of metal used. Oxides, halides and sulphides can also be used as precursors, likewise reacting at high temperature with NH_3 to form binary or ternary nitrides and gaseous by-products.^[19–21]

One of the most common reactions to form nitrides involves ammonolysis, the thermal decomposition of NH_3 . Gaseous ammonia dissociates at high temperature producing H_2 and N_2 . Ammonolysis is very effective for the nitridation of solid-state materials, also due to the reducing atmosphere due to the presence of H_2 , enhancing the reactivity of the material and preventing eventual oxidation side reactions. Furthermore, the dissociation of NH_3 is facilitated by the relatively low N-H bond energy (391 kJ/mol) compared with the more stable double bond in N_2 . Liquid ammonia can also be used due to its strong reducing power and it is particularly useful in some specific reactions with halides in the synthesis of binary nitrides (e.g. $SiCl_4$ to Si_3N_4).^[22] Among the non-gaseous sources of nitrogen, it is worth mentioning the decomposition of other nitrogen compounds, such as alkali metal binary azides (e.g. NaN_3).^[21]

Nitride materials find application in different technological and industrial areas. Nitrides are usually exploited for their thermal stability as refractory materials or for the production of cermets, such as TiN. Similarly, CrN coatings on ceramic materials provide protection against wear, corrosion, erosion and other physical damages.^[23] Transition metal nitrides have also been widely used in catalysis. Some examples are provided by hydrogenation reactions or synthesis of ammonia catalysed by vanadium nitride and vanadium oxynitride. Some intermetallic ternary nitrides such as $\text{Co}_3\text{Mo}_3\text{N}$, $\text{Fe}_3\text{Mo}_3\text{N}$ and $\text{Ni}_2\text{Mo}_3\text{N}$, have been successfully applied for the same purpose.^[24] Transition metal nitrides have also reported to show photocatalytic properties, such as Ta_3N_5 and the intermediate oxynitride structure, with relevant photoactivity under visible light due to their low band gap energy.^[25] The analogy with metal oxide semiconductors have been observed also in zirconium nitride, with electronic properties that have been exploited for the production of photovoltaic electronic devices.^[26]

Apart from transition metal nitrides, group IIIA nitride materials have also attracted great attention. This class of nitrides present very different electronic and optical properties depending on the p-block metal associated with the compound, with a wide range of applications available, specifically in optoelectronics. The selection of the nitride composition allows the band gap to be tuned from high energy values typical of insulating materials, such as in AlN (6.2 eV), to very low energies, for instance InN with a gap of 0.7 eV. GaN and InGaN have been widely employed to produce LEDs, with higher attention gained by these material because of the breakthrough discovery of blue emission.^[27] On the other hand, the insulating properties of AlN have been considered suitable for the production of gate dielectrics in field-effect transistors (FET).

Nitrides composed of non-metal elements are less common and rarely exist in nature. Silicon nitride (Si_3N_4) and boron nitride (BN) are two examples of this class. Si_3N_4 has been widely used as a ceramic presenting outstanding properties, including high thermal shock resistance, high strength and high oxidation resistance. BN films have shown to have enhanced field emission properties due to its negative electron affinity, making the material suitable for electronic devices, such as cold cathode emitters for miniature electric propulsion.^[28]

1.2 Nitride Halides

Most of the best known nitrides belong to the class of transition metal binary or ternary compounds. However, nitrides formed in combination with halogen elements constitute an unusual and interesting class of compound. Nitride halides are usually pseudo ternary compounds, combining nitrogen, a halogen and a metallic element belonging to the alkali, alkaline earth group or in some cases, transition metals.

Nitride fluorides represent one of the most common groups among nitride halides. The concept of simultaneous co-doping of oxides with nitrogen and fluorine is at the origin of the design of nitride fluoride materials. The replacement of O^{2-} with the insertion of N^{3-} and F^- would in theory compensate the structural and electronic changes due to the substitution, preserving properties such as electronegativity and atom space, but also bestowing new properties on the material, such as modification of the optical properties.

Alkaline earth nitride halides are quite well documented, forming ternary compounds with formula A_2NX (A= Ca, Ba, Sr; X=F, Cl, Br and I). These

compounds frequently present anti- α -NaFeO₂ type crystalline structure.^[29] Magnesium nitride fluorides exist as either Mg₃NF₃ or Mg₂NF.^[30] Ca₂NCl and Ca₂NBr were first reported in 1962 by Emons and Mitarh,^[31] but even more complex compositions and structures exist including quaternary systems such as Ca-N-X-X' (X, X'=Cl, Br, I), initially reported by Gregory *et al.* in 2005.^[32] Nitride halides with heavier alkaline earths have been also reported such as strontium nitride chloride and alkaline bromide (Sr₂NCl and Sr₂NBr, first reported in 2002^[29]) and barium, for which ternary structures have been reported with all four principal halides^{[33],[34]} and also quaternary compounds Ba₂N(X,X'), similar to the ones reported for Ca.^[35]

Of the alkali metals, only lithium nitride halides have been investigated first by Sattlegger and Hahn in 1964.^[36] These materials are good Li-ion conductors, and in principle promising materials for batteries.^[37] None of the other alkali metal elements form stable nitride halides because of the instability of the correspondent binary nitrides.

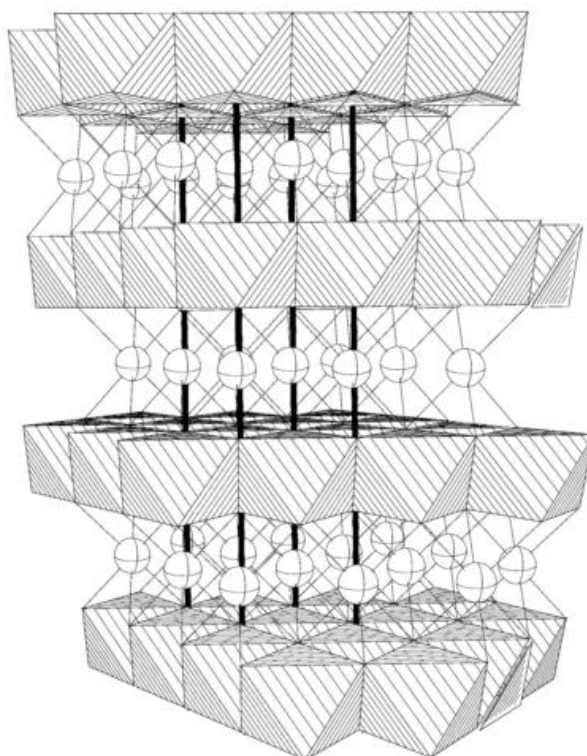


Figure 1.2 M_2NX ($M=Ca$ and Sr , $X=Cl$ and Br) crystal structure²⁹

Transition metal nitride halides have also been investigated for decades. The most representative materials of this category are nitride chlorides of Ce ($Ce_6Cl_{12}N_2$ and $CeNCl$),^[38] Y (Y_2Cl_3N)^[39] and Sc (Sc_5Cl_8N),^[40] Gd (Gd_2NCl_3),^[41] Mo ($MoNCl_3$) and W ($WNCl_3$).^[42] Apart from these, titanium and zirconium can form nitride halide structures with most of the halogens except fluorine, as discovered by Juza and Heners in 1962.^[43]

In this thesis project, we focused our attention on zinc nitride halides (Zn_2NX), firstly reported by Marchand *et al.* in 1970.^[44] The entire series of halides have been investigated in recent year,^[45] except for the nitride fluoride. The structure and properties of Zn_2NF have been only recently been the object of a detailed analysis by Lingampalli *et al.*^[46]

Nitride halides are produced following two general synthesis procedures. The first method involves reaction at high temperature of a metal nitride M_3N_2 and

a metal halide MX_2 ($\text{M}=\text{Zr}, \text{Zn}, \text{Ca}, \text{Mg}, \text{Sr}, \text{Ba}$. $\text{X}=\text{Cl}, \text{Br}, \text{I}$).^[47] The other method involves a direct nitridation of metal halides via thermal ammonolysis. The two approaches obviously differ in the source of nitrogen, with nitrides in the former and ammonia in the latter reaction. Other less common synthesis methods have been also reported using other sources of nitrogen, such as sub-nitrides, ammonium salts using N_2 gas directly.²⁹

1.3 Zinc nitride

Zn_3N_2 is a binary nitride associated with the II-V semiconductor group, together with Zn_3P_2 and Zn_3As_2 .⁴⁸ Zn_3N_2 was first synthesized by Juza *et al.* in 1940, who reported the formation of an anti-bixbyite type structure.^[49] Anti-bixbyite has a structure similar to Mn_2O_3 (bixbyite) with a reversed position between cations, occupying tetrahedral sites, and anions located in two different types of octahedral site.^[50] In 1997, Partin *et al.* refined the structure of Zn_3N_2 against neutron diffraction data, confirming the presence of zinc atoms in the tetrahedral powder holes within an approximately cubic close packed array of nitrogen atoms with two different sites N (1) and N (2), as shown in Figure 1.3^[51] The anti-bixbyite structure has also been observed in other divalent metal nitrides, including Ca_3N_2 , Mg_3N_2 , Be_3N_2 and Cd_3N_2 .

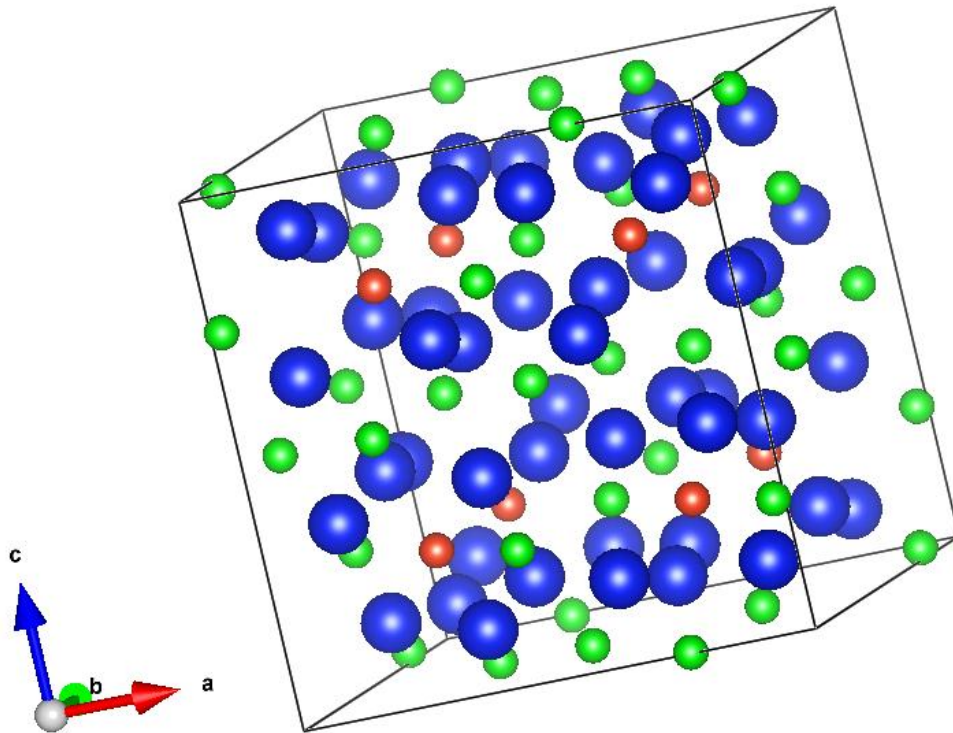


Figure 1.3 Zn_3N_2 anti-bixbyite crystal structure; blue spheres represent zinc atoms, green and red spheres represent N(2) and N(1) nitrogen atoms (drawn using VESTA software).

Different methods are reported for the synthesis of Zn_3N_2 , leading to different yield, crystalline phase composition, purity and morphology. Juza *et al.* firstly produced Zn_3N_2 via the thermal decomposition of $Zn(NH_2)_2$ but also by ammonolysis reactions with Zn powder, obtaining in both cases polycrystalline Zn_3N_2 powder.^[52] Several conditions for the ammonolysis synthesis of Zn_3N_2 have been explored during the past decades. Sakamoto *et al.* reported preparation of zinc oxynitride powders at 500 °C using different reaction times, varying from 24 - 168 hours.^[53] Paniconi *et al.* reported complete nitridation occurring from 4 - 30 hours.^[54] Zong *et al.* prepared Zn_3N_2 powder by performing the ammonolysis reaction with Zn powder at 600 °C, reducing the reaction time to only 120 minutes, despite longer times being generally reported in literature.^[55] The same authors reported the formation of Zn_3N_2 empty spherical structures by adopting the same reaction conditions.^[56]

Hollow structures of Zn_3N_2 produced via ammonolysis have also been reported by Khan *et al.*^[57]

Apart from ammonolysis, Futsuhara *et al.* prepared Zn_3N_2 films using reactive radio-frequency (RF) magnetron sputtering, using pure N_2 gas as a nitrogen source instead of ammonia.^[58] Zou *et al.* proceeded with a reverse approach, starting from Zn_3N_2 to partially oxidise the nitride producing ZnO:N films via reactive magnetron sputtering methods.^[59] Other types of Zn_3N_2 films have also been prepared on quartz substrates by reacting ammonia with zinc vapour at 410 °C.^[60] Zong *et al.* reported the synthesis of Zn_3N_2 nanowires in 2005.^[61]

Although synthesis of Zn_3N_2 by ammonolysis is a 70-year-old established method, the exact mechanism of the reaction is still not clear. Moreover, many of the properties of the material, such as its band gap are also ambiguous. Different synthesis methods can lead to different morphologies and different band gap values. The Zn_3N_2 film produced by Futsuhara *et al.* showed n-type semiconductor properties and a direct band gap of 1.23 eV.^[58] At the same time, Zn_3N_2 films have been investigated and found to show electronic mobility of $100 \text{ cm}^2\text{V}^{-1}\text{s}^{-1}$ at room temperature. Zn_3N_2 polycrystalline films, grown by metal-organic chemical vapour deposition (MO-CVD) methods, showed a band gap of 1.06 eV with a refractive index of $n=2.27-2.30$ at 600-690 nm^[62] whereas direct band gaps of 3.2eV have been reported^[60] in other polycrystalline films. Band gap values between 0.85-0.9 eV have been obtained by photoluminescence measurement of Zn_3N_2 powder.^[54]

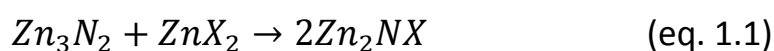
The electronic properties of Zn_3N_2 have been correlated with its crystal structure. Structural defects such as atom vacancies the interstitial atoms generally affect the electronic and optical properties. In the case of Zn_3N_2 , the presence as nitrogen atom vacancies leads to n-type conduction behaviour. Similarly, oxygen substitution at the nitrogen sites can also affect the

electronic properties, with higher oxygen concentration widening the optical band gap.^[63]

1.4 Zinc nitride halides

Zinc nitride halides, Zn_2NX ($X=Cl, Br, I$), are ternary compounds usually synthesised by reacting Zn_3N_2 with the zinc halide at high temperature. The two precursors are mixed in a 1:1 stoichiometric ratio.^[47] This class of materials was first discovered and synthesised in 1970 by Marchand *et al.*, who also reported the precise synthesis temperature and conditions.^[44] Zinc nitride halide can also be found as quaternary compounds $Zn_2NX_{1-y}X'_y$ ($X, X'=Cl, Br, I$; $0 < y < 1$), with two different halogens in the same compound.^[64]

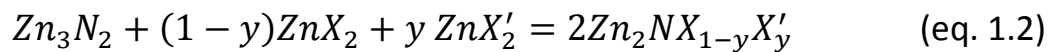
Synthesis of zinc nitride halides usually occurs by reaction in a mixed solid-liquid phase system, due to the relatively low melting point of the halide precursors (283 °C for $ZnCl_2$, 394 °C for $ZnBr_2$ and 446 °C for ZnI_2) compared to the synthesis temperature (500-550 °C).^[47] The only exception is represented by ZnF_2 , which is stable until 872 °C. Due to the 1:1 stoichiometric ratio, all nitride halide syntheses follow the simple reaction equation:



Nitride halides containing of Br, Cl and I all crystallise with orthorhombic structures. The thermal stability of these halides depends on the halogen used, with decomposition of Zn_2NCl and Zn_2NBr reported above 750 °C, whereas Zn_2NI decomposes at *ca.* 600 °C.

Synthesis of quaternary nitride halides $Zn_2NX_{1-y}X'_y$ has been reported only recently by Li *et al.* in 2016, in particular $Zn_2NCl_{0.47}Br_{0.53}$ and $Zn_2NBr_{0.62}I_{0.38}$, both crystallising with orthorhombic structures.^[64] The final composition of these

halides depend on the ratio of the different halides precursors in the synthesis reaction:



The reaction was performed at 550 °C for 20 hours, with the reactants sealed under vacuum in a quartz tube. ^[64]

1.4.1 Zinc nitride fluorides

Zn₂NF has been the least investigated halide until 2016, when Lingampalli et al. understood the potential application in water splitting of this material and of the possible intermediate structures between ZnO and the nitride fluoride. ^[46]

Zn₂NF was first synthesised in 1971 by Marchand *et al.*, together with Zn₂NBr. ^[65] Two different polymorphic structures have been reported for this nitride fluoride, both produced starting from stoichiometric mixture of Zn₃N₂ and ZnF₂, and three other compounds with a totally different structure and formula. The two polymorphs of Zn₂NF are labelled α-Zn₂NF and β-Zn₂NF, indicating the high-temperature and low-temperature crystalline phases, respectively. The low-temperature structure has lower symmetry (orthorhombic) compared to α-Zn₂NF, which crystallises in the tetragonal system. ^[46] Unlike the other nitride halides, the precursors of Zn₂NF are both in solid form during the reaction, due to the high melting point of ZnF₂ (872 °C) and the thermal decomposition temperature of Zn₃N₂, reported at 681 °C. ^[54] The formation temperature for the two different phases is 450 °C for α-Zn₂NF ^[65] and 350 °C for β-Zn₂NF. ^[46] The synthesis of the high-temperature phase has also been reported at 500 °C under vacuum. ^[46]

The allotropic structures are produced by non-stoichiometric reactions between Zn₃N₂ and ZnF₂, in particular Zn₉N₄F₆ (α-Zn₉N₄F₆ and β-Zn₉N₄F₆)

obtained by a 2:3 ratio between Zn_3N_2 and ZnF_2 . Conversely, $\text{Zn}_7\text{N}_4\text{F}_2$ is produced by an excess of nitride (2:1). $\text{Zn}_9\text{N}_4\text{F}_6$ decomposes at 460 °C into ZnF_2 , zinc and nitrogen. [65]

1.4.2 Nitride fluorides and doping

The combination of N^{3-} and F^- anions leads to an isoelectronic configuration by replacing two O^{2-} anions, although the difference in atomic radius causes distortions and other structural modifications. The first comparison of a nitride fluoride with the correspondent oxide material in terms of properties and applications was reported in 1969 by Andersson for Mg_2NF . [30]

Doping refers to the process involving insertion of a relatively low concentration of external elements (one or more) into the material structure, in order to modify or modulate the original properties. Several combinations of elements have been proposed as dopants (the term indicating the external elements) for the modification of the electronic and optical properties of semiconductors, including oxides (e.g. TiO_2 , ZnO). In particular, doping can be used to enhance the photocatalytic properties of semiconductors, by extending their response and photon absorption capacity towards visible light. The doping process is indeed responsible for the insertion of localised states between the two main electronic (valence and conduction) bands, lowering the effective energy of the band gap.

Considering a specific example, ZnO is an n-type semiconductor with a direct band gap of 3.37 eV. Individual nitrogen and fluorine doping of ZnO has been widely reported over the past decades. [59,66–68] The research interest moved towards the combination of N and F (co-doping), claiming a stabilizing effect of the structure due to the same overall electronic charge and compensation of

the difference in ionic radius (F^- is smaller than O^{2-} , which in turn is smaller than N^{3-}). A successful example of co-doping is given by $ZnO_{1-x}(N, F)_x$ reported by Rao *et al.* in 2013, improving the photocatalytic properties of the material compared to ZnO due to the efficient reduction of the material band gap.^[70] A progressive replacement of oxygen atoms with nitrogen and fluorine would lead in theory to a series of intermediate structures, ultimately achieving a pure Zn_2NF structure at $X=1$. Both intermediate $Zn_2NF-ZnO$ and doped-ZnO structures show potential application in visible-light photocatalysis or hydrogen generation by water splitting. A maximum band gap reduction to 2.75 eV for intermediate $Zn_2NF-ZnO$ and to 2.4 eV for doped ZnO has been already achieved, in both cases preserving the original structure of ZnO.^[46]

1.5 Photocatalytic materials

Photocatalytic properties are used in a wide variety of applications in different technological areas, such as degradation of organic molecules or pollutants, production of antibacterial materials, water splitting for hydrogen generation and waste gas reduction processes.^[70]

Inorganic semiconductors such as transition metal oxides, nitrides and sulphides are usually well known for their photocatalytic properties. The photocatalytic process involves the absorption of an external photon generating an electron-hole pair; an electron (e^-) is promoted in the conduction band (the lowest unoccupied electronic level in the material) from the valence band (the highest occupied electronic level), leaving a corresponding vacancy in the latter band. The vacancy is considered as a positive entity termed a hole (h^+). For the electron promotion to occur, the material should gain from the photon the necessary amount of energy

equivalent to the difference between the energy of the conduction and the valence bands, also defined as the energy band gap (of forbidden energy levels).

Holes and electrons can recombine (the electron comes back to the valence band) or migrate towards the material surface, where catalytic processes take place. Considering catalysis in an aqueous environment, the positive holes oxidise water molecules generating hydroxyl radicals ($\bullet\text{OH}$) and H^+ . Electrons react with adsorbed O_2 , producing other radical species (O^{2-} , $\text{HO}_2\bullet$ and ultimately H_2O_2). The radical species play the most important roles in photocatalytic processes such as degradation of organic pollutants or destruction of bacteria and microorganisms. The overall set of radicals is generally indicated by the name Reactive Oxygen Species (ROS), with the processes involved defined as Advanced Oxidation Processes (AOPs). ROS are very important in environmental applications, because of complete degradation of the pollutants until their mineralisation into CO_2 and H_2O , without residual by-products. Another important application is represented by the production of H_2 via water splitting. In this case, the holes react with water forming O_2 and H^+ , whereas the electrons produced OH^- and H_2 .^[71] A schematic representation of the water splitting process is reported in Figure 1.4.

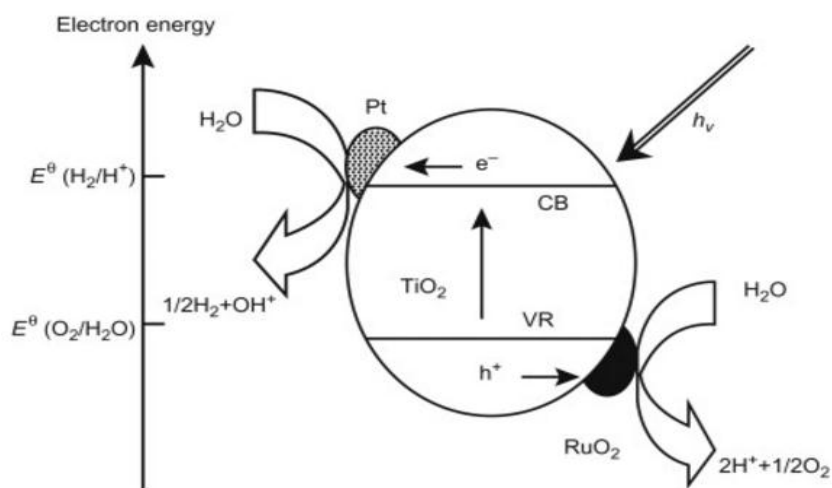


Figure 1.4: TiO₂ photocatalysis in the water splitting [70]

Photocatalytic materials include several categories of semiconductor material such as oxides (from binary to quaternary systems), binary sulphides, selenides and graphene oxide. Binary transition metal oxides are the most common photocatalytic materials, with TiO₂, ZnO and WO₃ as representative compounds. TiO₂ was the first to be investigated, with the discovery of its photocatalytic properties for water splitting by Fujishima and Honda in 1972.^[72] Since then, research on TiO₂ has driven towards the improvement of its properties, acting on morphology, production of nanosized structures (nanotubes, nanoparticles), surface area, application as thin films and doping. [73–75]

1.6 Objectives and scope of this work

The principle aim of this research project was to study the synthesis of and to characterise, zinc nitride fluoride (Zn₂NF) and to investigate its potential for photocatalysis under visible light. Efficient synthesis of this material can only be achieved by first preparing zinc nitride (Zn₃N₂). The production of Zn₃N₂ is governed by strict experimental conditions (including a narrow range of

reaction temperature) and is extremely sensitive to ZnO impurities, which even appear in commercial products with high purity standards.

Consequently, the first objective of this research was to optimise the synthesis of Zn_3N_2 , modifying the conventional ammonolysis synthesis reaction and studying the reasons behind the formation of the nitrides and the presence of oxide impurities. Synthesis parameters such as temperature, treatment time, setup design, heating and cooling rate, reduction of the source of impurities can all potentially improve the quality of the final products. Although the Zn_3N_2 structure has been widely reported, other important characteristics such as morphology have seldom been described.

The second part of the research project is based on the recent findings of Lingampalli *et al.* about the properties of Zn_2NF and the intermediate structures formed between this material and undoped ZnO. The progressive substitution of oxygen ions by the two non-oxide anions led to a gradual change of properties, from light doping to heavier structural lattice distortions, up to non-stoichiometric mixed compounds and finally to pure nitride fluoride. According to the authors, each of these intermediate materials presented different properties, in particular a reduction of the optical band gap and an improvement in the efficiency of water splitting for hydrogen generation.^[46] Likewise, improvement of antibacterial properties in F-doped ZnO materials compared to bare ZnO have been reported, paving the way for new potential applications for this class of materials.^[76]

Therefore, the full characterisation of Zn_2NF is a priority in understand as the effect of the simultaneous insertion of the two anions in the structure and of the various degree of substitution. Potentially a whole class of new intermediate compounds ($ZnO_xN_yF_z$) could be accessed, for which the synthesis mechanism, reaction conditions and definition of the final properties remain as

uncharted territory. Moreover, the properties of the different polymorphs of Zn_2NF and associated compounds have been described by a handful of research work. It is hence necessary to perform a more detailed investigation of the synthesis conditions of these materials and their related properties, such as the phase transition temperatures from one form to another.

All materials were fully characterised from the point of view of their structural properties (X-ray diffraction and Raman analysis), morphological features (SEM), elemental composition (EDX) and electronic and optical properties (UV-Vis spectroscopy, band gap calculation). Rietveld refinement was also used to obtain more structural information about Zn_3N_2 . The mechanistic study of the formation of both Zn_3N_2 and Zn_2NF was performed by Simultaneous Thermal Analysis (STA) investigation, following the mass change and thermal events occurring during a specific heating program.

Finally, the products of the optimised synthesis were tested to assess their photocatalytic properties under both UV and visible light, compared with ZnO and other photocatalysts (e.g. TiO_2). Controlled degradation of an organic dye was used for this purpose.

Chapter 2: Experimental Methods

2.1 Ammonolysis reactions

Ammonolysis reactions were essential for the development of this research project. All ammonolysis reactions were performed in a Carbolite™ tube furnace, with a mullite tube as structural support for the sample insertion inside the furnace. The ammonia gas (BOC, 99.98%) flow rate was controlled by a specific flowmeter (MPB, Series 1200), calibrated for this gas. Flow rates of 0.3-0.5 L/min were usually used as a standard setting. A constant flux of NH₃ was kept throughout all the reaction steps, from the initial heating to reaction temperature until the end of the thermal treatment. Before the ammonolysis reaction, the furnace tube was purged from the presence of atmospheric gases by flowing ammonia for at least one hour. The reactants were placed in an alumina boat, placed in the middle of the reaction tube, where the heating efficiency is at its maximum. The final products were removed directly from the tube furnace after reaction. No protected atmosphere was needed, since the products were stable in air. Ammonia gas exhausts were neutralised by sulphuric acid (Fisher, >95%) solutions. The pH of the solution was constantly checked in order to control the efficiency of neutralisation. Alizarin Yellow R sodium salt (Acros Organic, 96%) was used as indicator for the acid solution. Alizarin Yellow changes its colour at very high pH (12), turning from pale yellow to deep red. The red colour indicates the saturation of the solution by NH₃. At this point, the acid solution should be replaced with a fresh one.

At the end by each reaction, the sample was cooled to room temperature under a constant flow of gas, to prevent oxidation of the products during the cooling phase. However, different gas atmospheres were used during the

cooling process depending on the type of reaction. For the Zn_3N_2 synthesis reaction, cooling was performed under an argon atmosphere (argon, BOC, 99.9995%). On the other hand, ammonia was used during the cooling phase of doped materials.

2.2 Crystallography

A crystal is defined as an ordinate structure built from a regularly repeating atom arrangement in the three spatial dimensions. In this arrangement, the unit cell defines the smallest repeating unit. The entire crystal is formed by those fundamental units by pure translational displacements. The unit cell also shows the symmetry of the crystal structure. Three directions of unit cell are defined as a , b , c , and the angles between the edges are defined as α , β , γ (Figure 2.1).

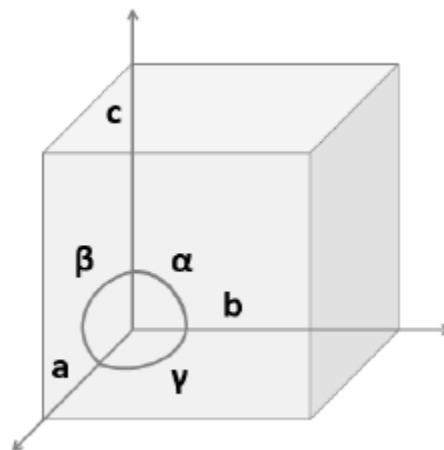


Figure 2.1 Unit cell vectors and angles

The set of symmetry operations that apply to the contents of a unit cell is by a point group, in which one point is fixed while the other geometric elements (crystal planes, lattice vectors) can be moved according to the symmetry

operators (for example rotation or inversion). Considering these non-translational symmetries, only 32 point groups define the unit cell symmetries. The point groups can be classified in seven sub-categories according to the type of symmetry operators applied. The seven categories are defined as the lattice systems. The classification is congruent with the lattice system, except for some cases. The seven crystal systems and their characteristic unit cell parameters are listed in Table 2.1.

Table 2.1 Unit cell vectors and angles

System	Unit cell
Triclinic	$\alpha \neq \beta \neq \gamma \neq 90^\circ$ $a \neq b \neq c$
Monoclinic	$\alpha = \gamma = 90^\circ$ $\beta \neq 90^\circ$ $a \neq b \neq c$
Orthorhombic	$\alpha = \beta = \gamma = 90^\circ$ $a \neq b \neq c$
Trigonal/rhombohedral	$\alpha = \beta = \gamma \neq 90^\circ$ $a = b = c$
Hexagonal	$\alpha = \beta = 90^\circ$ $\gamma = 120^\circ$ $a = b \neq c$
Tetragonal	$\alpha = \beta = \gamma = 90^\circ$ $a = b \neq c$
Cubic	$\alpha = \beta = \gamma = 90^\circ$ $a = b = c$

Atoms or ions are placed in the lattice points with different symmetry depending on the crystal system. According to the relative position of the atoms in the unit cells, those can be classified in four groups, identified by capital letters. *P* refers to a primitive cell, where lattice points only exist on the cell corners; *I* refers to body-centred structure in which lattice points at the cell corners are also located at the centre of the cell; *A, B* and *C* refer to base-centred cells, which lattice points are on the cell corners are also is located at the centre of one pair of opposite faces (e.g. *A*-centred cell lattice points in the *bc* faces and so on); finally, *F* refers to a face-centred unit cell with lattice points on the cell corners and at the centre of each face of the unit cell. These

four different lattice types combine with the seven crystal systems into fourteen lattice representations known as Bravais lattices, listed in Table 2.2.

Table 2.2: Bravais lattices and their corresponding symmetry

Crystal system	Lattice symbol	Minimum symmetry
Triclinic	<i>aP</i>	<i>None</i>
Monoclinic primitive	<i>mP</i>	<i>One two-fold axis or one symmetry plane</i>
Monoclinic centred	<i>mC</i>	
Orthorhombic C-face-centred	<i>oP</i>	<i>Any combination of three mutually perpendicular two-fold axes or planes of symmetry</i>
Orthorhombic primitive	<i>oC</i>	
Orthorhombic body-centred	<i>oI</i>	
Orthorhombic face-centred	<i>oF</i>	
Tetragonal primitive	<i>tP</i>	<i>One four-fold axis or one four-fold improper axis</i>
Tetragonal body-centred	<i>tI</i>	
Trigonal (Rhombohedral)	<i>hR</i>	<i>One three-fold axis</i>
Hexagonal primitive	<i>hP</i>	<i>One six-fold axis or one six-fold improper axis</i>
Cubic primitive	<i>cP</i>	<i>Four three-fold axes along the body diagonals</i>
Cubic body-centred	<i>cI</i>	
Cubic face-centred	<i>cF</i>	

The combination of the 32 point groups with the 14 Bravais lattices results in 230 three-dimensional space groups that define the symmetry of all crystalline structures.

Lattice points are considered as an array of equivalent points which lie on a plane known as a lattice plane. The unit cell dimensions and symmetry define families of parallel lattice planes and their separation within a crystal. The different sets of planes in the crystal system are described by Miller indices, identifying the direction of the planes. The Miller indices are integer numbers

with positive, negative or zero values, generally indicated as h , k and l along the three spatial dimensions in the reciprocal lattice (the Fourier transform of the corresponding Bravais lattice). The distance between parallel planes (d_{hkl}) can be determined using the Miller indices and the cell parameters. The expressions relating all these parameters depends on the geometry of the crystal system and are listed in Table 2.3.

Table 2.3: Relation between lattice spacing (d_{hkl}) and cell parameters

Crystal system	d_{hkl} <i>(as a function of the Miller indices and lattice parameters)</i>
Cubic	$\frac{1}{d_{hkl}^2} = \frac{h^2 + k^2 + l^2}{a^2}$
Tetragonal	$\frac{1}{d_{hkl}^2} = \frac{h^2 + k^2 + l^2}{a^2} + \frac{l^2}{c^2}$
Orthorhombic	$\frac{1}{d_{hkl}^2} = \frac{h^2}{a^2} + \frac{k^2}{b^2} + \frac{l^2}{c^2}$
Hexagonal	$\frac{1}{d_{hkl}^2} = \frac{4}{3} \left(\frac{h^2 + hk + k^2}{a^2} \right) + \frac{l^2}{c^2}$
Monoclinic	$\frac{1}{d_{hkl}^2} = \frac{1}{\sin^2\beta} \left(\frac{h^2}{a^2} + \frac{k^2 + \sin^2\beta}{b^2} + \frac{l^2}{c^2} - \frac{2hlc\cos\beta}{ac} \right)$
Triclinic	$\frac{1}{d_{hkl}^2} = \frac{1}{V^2} [h^2b^2c^2\sin^2\alpha + k^2a^2c^2\sin^2\beta + l^2a^2b^2\sin^2\gamma + 2hkabc^2(\cos\alpha\cos\beta - \cos\gamma) + 2kla^2bc(\cos\beta\cos\gamma - \cos\alpha) + 2hlab^2c(\cos\alpha\cos\gamma - \cos\beta)]$

The Miller indices can describe a specific set of parallel planes using the notation (hkl) , a family of planes equivalent by symmetry $\{hkl\}$ or a direction orthogonal to a specific plane, indicated as $[hkl]$. Bravais lattices and Miller indices are used for crystallography classification.

2.2.1 PXRD

Powder X-ray Diffraction (PXRD or simply PXD) is used to analyse polycrystalline powdered samples comprising known or unknown crystalline phases. PXD is a useful technique for the identification of crystal structure, and provides other information such as the purity of a sample and its phase composition. PXD analysis produces a specific pattern. The analysis of this pattern is a powerful and efficient method for the structure characterisation of a material. The PXD pattern can be fitted using mathematical algorithms to obtain basic structural information such as cell parameters, bond length and angles and the relative composition of the sample in case of multiple phases.

X-ray radiation is emitted at high frequency and energy. X-rays are generated by the interaction of a high-energy electron beam, emitted from a tungsten filament, and a metal target. Copper or molybdenum are generally used as a target. A given X-ray emission is monochromatic, with wavelength (λ) depending on the electronic structure of the atom of the target. The electron beam causes the expulsion of an atomic electron from its orbital in the core shell (1s). Electrons from outer-shell orbitals (2p or 3p) decay to the inner orbital level replacing the expelled electron. The transition is followed by the emission of a photon with energy equal to the difference of the outer and the inner levels involved. The energies involved correspond to X-ray frequency, corresponding to wavelength of the order of the Å unit, the same as typical interatomic distances in the crystal structures. For example, copper has a specific K_{α} emission at 1.5418 Å which is less energetic than molybdenum (K_{α} 0.7107 Å).

XRD analysis is based on the principle of electromagnetic radiation diffraction, the phenomenon in which a light beam “bends” around an obstacle with size in the same order of magnitude of the beam wavelength. For instance, when a light beam pass through a narrow slit, diffraction occurs with the beam spreading around the slit and generating constructive and destructive interference. This principle is applied for the isolation of a single wavelength from a polychromatic light beam using an optical grating. When polychromatic light passes through the grating slits, diffraction occurs, with interference phenomena depending on the mutual orientation of the light beam and the grating. The production of a monochromatic beam of light is possible because the grating orientation allows only selected wavelengths to interfere constructive interference. In a like manner, a crystal lattice acts as a grating towards X-ray beams striking on it. The incident X-ray beam interacts with the lattice points, being deflected in the opposite direction with the same angle. The set of lattice points lying on the parallel planes creates constructive and destructive interferences. For each family of planes, only a certain incident direction can generate constructive interference producing a reflection. The schematic representation of the phenomenon is shown in Figure 2.2, with the geometrical demonstration of the constructive interference in X-ray diffraction. Considering two distinct parallel X-ray beams in phase, A and B, the conditions for constructive interference requires a distance xyz of the beam B equal to an integer number (n) of wavelengths (i.e. for beam B to be in phase with the beam A):

$$xyz = n \lambda \quad (\text{eq. 2.1})$$

This optical path of the beam inside the crystal is related to the incident angle θ , and the distance d_{hkl} between parallel lattice planes of specific (hkl) . The optical path can then be calculated as:

$$xy = yz = d \sin \theta \quad (\text{eq. 2.2})$$

$$xyz = 2d \sin \theta \quad (\text{eq. 2.3})$$

Combining the previous equations, the conditions for reflection from a family of parallel planes is given by Bragg's law:

$$2d \sin \theta = n\lambda \quad (\text{eq. 2.4})$$

The incident angle θ satisfying the reflection conditions is also defined as the Bragg angle.

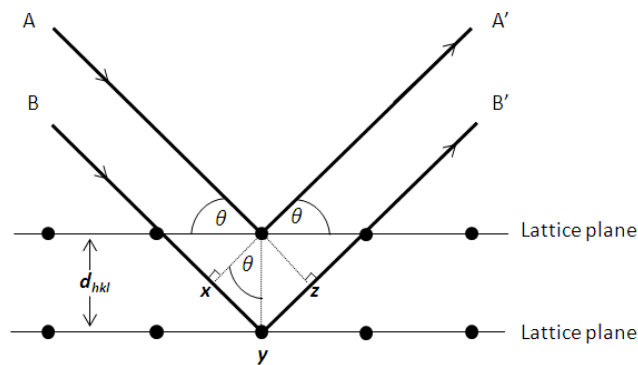


Figure 2.2 Reflections of X-ray beams illuminate on crystal planes

Each family of planes in the crystal will generate a distinctive set of reflections as a function of the incident angle. In a diffractometer, the X-ray beam scans the sample within a specific range of angles, collecting the intensity reflected at the same angle in the opposite direction. The result is a pattern, with each peak corresponding to a specific set of planes (hkl). The pattern is the fingerprint of the crystal structure. The diffraction pattern is specific for the crystal structure (lattice parameter, space group) and for the X-ray wavelength used. The PXD patterns for this project were collected using a single wavelength ($\text{Cu K}\alpha$), isolated by a monochromator.

Different geometries are available for the collection of the reflections from crystalline materials. For powders, the most common is the Bragg-Brentano (or

flat plate) geometry (Figure 2.2). The powdered sample is generally polycrystalline, with the individual single crystallites randomly oriented. The detector, placed at a 2θ angle with respect to the incident beam, collects the constructive interference from all the crystallites respecting Bragg's law for certain values of θ (Figure 2.3).

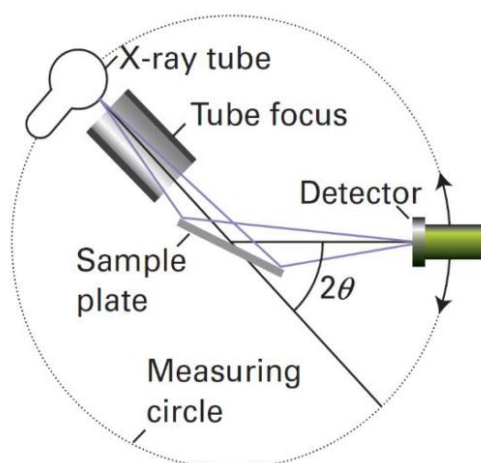


Figure 2.3 Scheme of Bragg-Brentano geometry, used in X'pert diffractometer^[77]

By measuring different Bragg angles, the parameters of the unit cell can be easily obtained as well as the symmetry information. The intensity of the reflections is strictly related to the period is arrangement of atoms in the unit cell.

The diffractometer used for the analysis of the powder was a PANalytical X'Pert Pro MPD, with a Cu X-ray source and a monochromator selecting only Cu K_{α} emission ($\lambda=1.54056 \text{ \AA}$), avoiding the presence of double peaks by excluding K_{β} radiation. For the analysis, the powdered sample was placed on a bracket comprising, a sample holder made of a glass slide with a circular cavity in its middle. The powder was carefully pressed into the cavity, ensuring that the sample as the same level with the surface of the glass slide. Uniformity of the sample surface helps to reduce the background intensity, unwanted shift in 2θ or a change of relative intensity. Another cause of problems could be

preferred orientation effects of the powder during the sample preparation, leading to the enhancement of the intensity of peaks corresponding to crystalline alignment in a certain direction. In almost all the measurements, the analysis was set with a 2θ scan range of 15-85°, using a 0.0334° step size. All measurements were performed at room temperature. For phase identification, a standard scanning time was selected of *ca.* 25 to 30 minutes, corresponding to an exposure of around 100 s per point. For more accurate analysis, such as structure refinement (see below), the scan was extended for several hours (typically up to 12), in order to increase both the number of collected points and their intensity (depending on the exposure time).

A first analysis of the patterns involving phase identification and peak indexing was performed using the software X'pert High Score and Fullprof. The patterns were compared using both the ICDD (International Center for Diffraction Data) and the ICSD (Inorganic Crystal Structure Database) databases. For certain specific samples, further structural information was obtained via the Rietveld refinement process, using GSAS (General Structural Analysis System) software.^[78]

2.2.2 Rietveld Refinement

Rietveld refinement is a popular method for the analysis of crystal structure starting from their X-ray or neutron diffraction pattern and a crystal structure model. The method was first developed by Hugo M. Rietveld in 1966. Rietveld refinement is a mathematical fitting method applying models of geometrical profile shape to the peaks of the PXRD pattern. The observed or experimental pattern is compared with calculated data; a theoretical pattern of the material based on reported structural data (space group, cell parameters, etc.). Experimental and calculated patterns are compared according to a least

squares fitting algorithm, which minimises the differences between the experimental data and the model. The refinement is performed through cycles of calculation. The refinement can be considered successful if at the end of the calculations, the calculated and observed patterns are almost identical, (within the limits imposed by the physical parameters (e.g. thermal factor cannot be negative)). Important structural information can be obtained, such as atomic position, site occupancies, Debye-Waller factors, textures and residual stress.

In the least squares approach used for the refinement, the algorithm minimises a function S_y defined as the weighted difference between the intensities of the observed or experimental pattern $[y(\text{obs})]$ and calculated or theoretical pattern $[y(\text{calc})]$ as showed in equation X:

$$S_y = \sum_i w_i [y_i(\text{obs}) - y_i(\text{calc})]^2 \quad (\text{eq. 2.5})$$

The intensities of the calculated pattern are determined by structures factors (F_K), obtained from the crystallographic model plus a background contribution:

$$y_{\text{calc}} = s \sum_K L_K |F_K|^2 \varphi(2\theta_i - 2\theta_K) P_K A + y_{\text{bi}} \quad (\text{eq. 2.6})$$

where s , the scale factor depends on the quantity of irradiated sample present. The subscript K represents a specific reflection from (hkl) planes; L_K refers to the Lorentz-Polarization factor; φ is the instrumental profile function, describing the characteristic of the signal (peak asymmetry, shape, etc..) which is dependent upon the instrument used; θ_i and θ_K are the Bragg angles for experimental and calculated patterns, respectively; P_K refers to a preferred orientation function; A is an absorption factor; y_{bi} represents the background intensity at point i . The structure factor F_k is defined as:

$$F_K = \sum_{j=1}^N N_j f_j e^{2\pi i(hx_j + ky_j + lz_j)} e^{-\frac{8\pi^2 \langle u_j^2 \rangle \sin^2 \theta}{\lambda^2}} \quad (\text{eq. 2.7})$$

where h, k, l are Bragg reflections indices, N_j refers to the multiplicity of an atom occupation; f_j is the scattering length; (x_j, y_j, z_j) are the coordinates of the atom 'j' and finally the exponential term $-\frac{8\pi^2 \langle u_s^2 \rangle \sin^2 \theta}{\lambda^2}$ defines the temperature factor, with $\langle u_s^2 \rangle$ the root mean square displacement of the atom parallel to the diffraction vector. Background intensity (y_{bi}) often depends on 2θ and can be fitted by a variety of functions, for example according to the expression:

$$y_{bi} = \sum_{n=0}^{N_b} a_n (2\theta_i)^n \quad (\text{eq. 2.8})$$

where N_b refers to the polynomial degree and a_n the polynomial coefficients. The profile functions for curve shape fitting can be Gaussian (G), Lorentzian (L) or pseudo-Voigt (pV) function:

$$G = \frac{(4 \ln 2)^{\frac{1}{2}}}{H_K \sqrt{\pi}} e^{\left(\frac{-4 \ln 2 (2\theta_i - 2\theta_K)^2}{H_K^2} \right)} \quad (\text{eq. 2.9})$$

$$L = \frac{2}{\pi H_K} / \left[1 + 4 \frac{(2\theta_i - 2\theta_K)^2}{H_K^2} \right] \quad (\text{eq. 2.10})$$

$$pV = \eta L + (1 - \eta)G \quad (\text{eq. 2.11})$$

The Gaussian function represents the main contribution to the experimental profile. The Lorentzian function indicates the diffraction peaks broadening, usually due to reduced crystal size or structural microstrain. The pseudo-Voigt function is then an optimal compromise to fit the peak shape, since it consists of the combination of both Gaussian and Lorentzian profiles. In equation 2.11, η is a mixing parameter, indicating the relative weight of the two functions in the profile fitting. H_K refers to the full-width-at-half-maximum (FWHM) of the Kth Bragg reflection. H_K is defined by the Caglioti function which describes the modification of the FWHM depending on the scattering angle $2\theta_K$, as reported

in equation 2.12:

$$H_K^2 = U \tan^2 \theta + V \tan \theta + W \quad (\text{eq. 2.12})$$

where U, V and W are refinable parameters and both depend on the instrument and the sample.

The quality of the refinement is rated by specific figure of merit called agreement indices, also known as R values. The R values are aimed to verify and control all the aspect of the refinement. There are several R values that are calculated including the weighted-profile R-factor (R_{wp}):

$$R_{wp} = \left\{ \frac{\sum_i w_i [y_i - y_{calc}]^2}{\sum_i w_i (y_i)^2} \right\}^{1/2} \quad (\text{eq. 2.13})$$

the expected-R factor (R_e):

$$R_e = \sqrt{\frac{(N-P+C)}{\sum w_i (y_i)^2}} \quad (\text{eq. 2.14})$$

the unweighted-profile R-factor (R_p):

$$R_p = \frac{\sum |y_i - y_{calc}|}{\sum y_i} \quad (\text{eq. 2.15})$$

the intensity R-factor (R_i):

$$R_i = \frac{\sum |I_{Ki}^2 - I_{Kcalc}^2|}{\sum I_{Ki}^2} \quad (\text{eq. 2.16})$$

and the Bragg R-factor (R_B):

$$R_B = \frac{\sum |I_{Ki} - I_{Kcalc}|}{\sum I_{Ki}} \quad (\text{eq. 2.17})$$

where I_{Ki} and I_{Kcalc} are observed and calculated Bragg number of intensities of the reflection (h k l); N is the number of observations, P is the refined

parameters and C is the number of constraints; y_i and y_{calc} are the observed and calculated intensities at point i .

The R values generally considered important for the quality of the refinement are R_{wp} and R_e . A good refinement should present very close values for these two agreement factors. For this reason, the quality of the refinement can be ultimately defined by the square ratio of these two R -factors, defined as χ^2 :

$$\chi^2 = \left(\frac{R_{\text{wp}}}{R_e} \right)^2 \quad (\text{eq. 2.18})$$

For a perfect fit χ^2 is equal to 1. However, in many cases χ^2 values less than 5 can be considered as acceptable. Rietveld refinement thus performed by comparing an experimental XRD pattern with a theoretical structure, using software such as GSAS with EXPGUI interface for the calculation process.^[79]

2.3 Scanning Electron Microscopy (SEM) and Energy Dispersive X-ray Spectroscopy (EDX)

2.3.1 Scanning Electron Microscopy

Scanning electron microscopy (SEM) is an imaging technique using an electron beam to observe sample morphology at nanometric scale. Compared with optical microscopy, electron microscopy can achieve significantly higher magnification. The resolution of optical microscopes is limited by the diffraction of the light beam, preventing the observation of features with size comparable to the wavelengths used (400-700 nm in case of visible light). Furthermore, non-monochromatic sources of light prevent optimal resolution at higher magnification (within diffraction limits) because of chromic

aberration, due to the different refraction of the different wavelengths of the light beam through the lenses, since the refractive index depends on the wavelength. The corresponding wavelength of electrons is much smaller, of a size comparable to the atomic scale, leading to higher resolutions and magnification factors up to hundreds of thousand times.^[80]

A typical SEM instrument consists of three main parts: the electron beam generator, the sample stage and the detector. Electrons are typically generated by thermionic emission from a tungsten or LaB₆ filament, occurring when electrical current passes through it. The emitted electrons, also called primary electrons, are accelerated towards the sample by a high potential difference (10-30 kV) and focused on the target sample by magnetic lenses. The whole chamber of an SEM is kept under vacuum to prevent electron scattering with the atmospheric components. The focused beam scans the sample, providing useful information about the morphological feature of the analysed surface. When the electron beam hits the sample, two types of interactions occur between the electrons and the superficial layer of the sample. For SEM imaging, the detector collects mainly backscattered electrons and secondary electrons, converting them into digital signals allowing the reconstruction of the sample image.

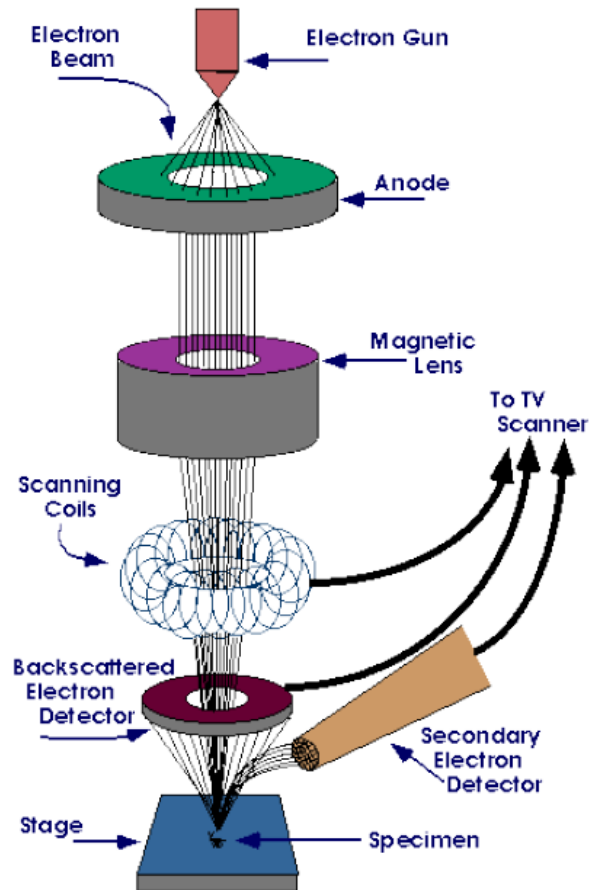


Figure 2.4 Structure of a typical SEM instrument

Because of the specific imaging process, one of the requirements is for the surface of the sample to be conductive. In the case of dielectric materials, the electrons accumulate, generating surface charge which results in overexposure in the image contrast. It is then necessary to coat the surface of a dielectric sample with a conductive layer, usually a thin film of gold or platinum, to prevent the changing at the sample surface.

For the analysis of powdered samples, a small amount of powder is fixed to an aluminium stub by a graphite adhesive sticker. The sample is coated by a sputtering process, using an Ar plasma. The heavy Ar^+ ions generated in the plasma etch a target in gold or platinum above the sample, creating a thin film on the sample surface. The coating process usually lasts 60 to 120 seconds.

A Philips XL 30 ESEM was used for SEM analysis.

2.3.2 Energy Dispersive X-ray Spectroscopy (EDX)

Energy dispersive X-ray (EDX) Spectroscopy was used to determine elemental composition. EDX spectroscopy is generally associated with SEM, using the same setup but exploiting a different physical phenomenon. In EDX spectroscopy, the elements present on the sample surface are identified by the X-rays emitted from them. When the electron beam of the SEM hits the sample surface, high-energy electrons are emitted from the inner electronic shells of the atoms in the sample, with subsequent decay of another electron from an outer level to compensate the vacancy. This phenomenon causes the generation of a photon of energy equal to the difference between the transition levels, corresponding to X-ray frequencies. The energies of the emitted X-rays are characteristic for each atomic element, allowing identification and quantification. For quantification purposes, the instrument is calibrated using a reference material, usually copper. Quantification is not possible in the case of lighter elements, because of the limited number of shells in the atomic structure. For these elements, the X-rays generated are less energetic, difficult to be detected and, in some cases, re-absorbed by the sample.

2.4 UV-Vis Spectroscopy

UV-Vis spectroscopy was used in this project to evaluate the optical properties of powdered materials. The optical band gap can be measured for solid state samples by Diffuse Reflectance Spectroscopy (DRS). This analysis was performed using an integrating sphere applied to a conventional double-beam UV-Vis spectrometer. The sphere is an optical device that collects the reflectance diffused by the sample when the incident beam hits its surface at a

certain angle, determined by the geometry of the optical setup. For the setup used in this project, the range of the measurement spans from the UV region (190 nm) to the near IR wavelengths (1300 nm).

UV-Vis spectroscopy was also used for the measurement of photocatalytic degradation of organic dyes. The absorbance intensity of the organic dye solution is directly proportional to its concentration. The degradation rate or efficiency under UV or visible light can be measured following the decrease of the absorbance intensity during the experiment.

2.4.1 Band gap measurement and calculation

Band gap measurements were performed by UV-vis diffuse reflectance spectroscopy (DRS), a very common technique for the analysis of semiconductor materials in bulk, powder or thin film form. Polycrystalline materials cannot reflect the incident light uniformly, which is scattered in all directions, diffusing those photons not absorbed or transmitted. Exploiting this principle, the collection of the entire diffuse reflectance gives important information about the optical properties of the material. As already mentioned, the integrating sphere device allows the collection of the whole diffuse radiation. A scheme of the optical device is presented in Figure 2.5.

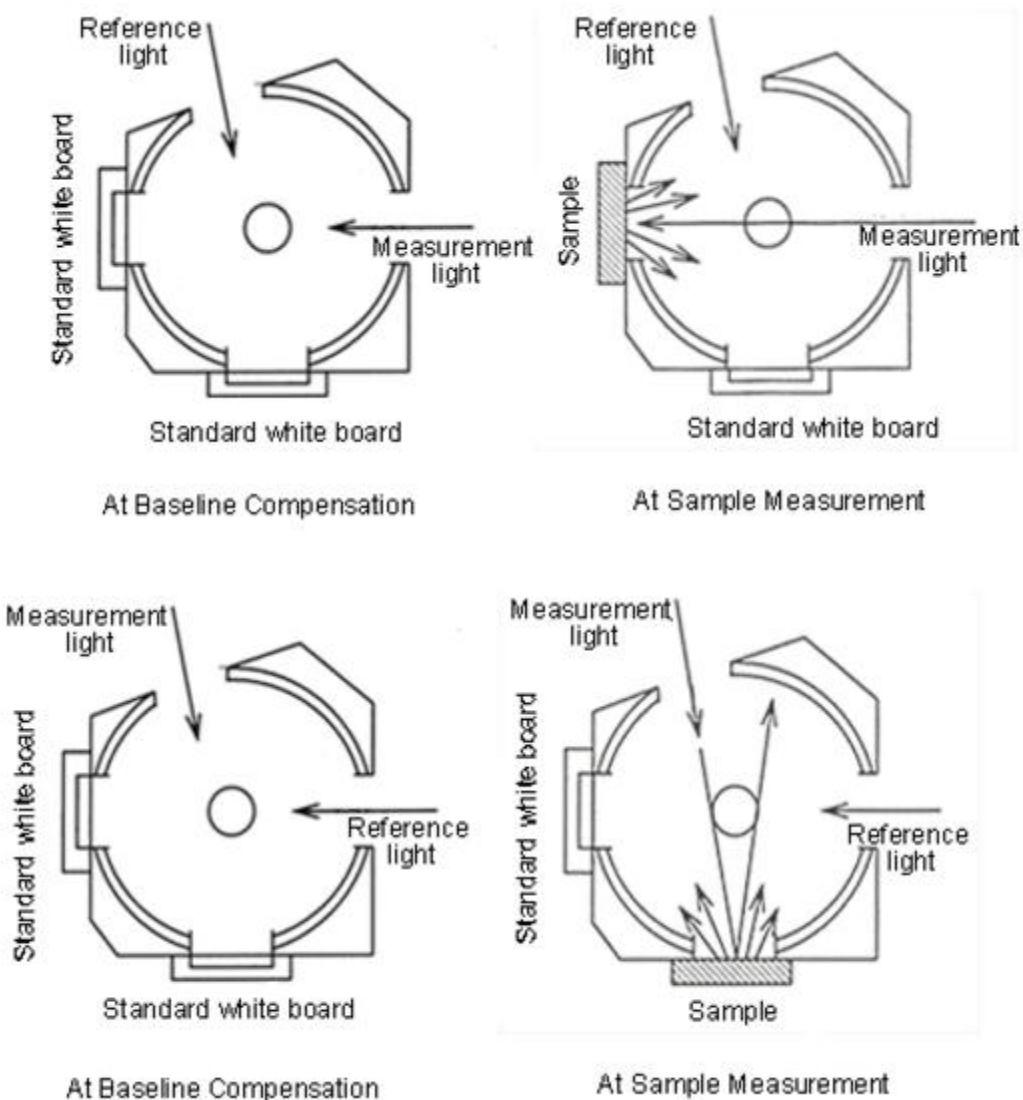


Figure 2.5 Scheme of the integrating sphere device, showing the optical geometry of the incident and reflected light beams

The integrating sphere inner surface is coated with a highly reflective coating (BaSO_4) towards the whole spectrum of irradiating frequencies. The inner walls of the sphere concentrate the diffuse reflectance arising from the sample. The resulting reflectance value is compared with the reflectance of the reference standard, a uniform and compact layer of pressed BaSO_4 powder. The initial baseline measurement is performed using this standard, allowing the evaluation of instrumental error (such as optics misalignment or optical source malfunctioning), since the reflectance should theoretically account for 100% or

be deleted output. The optical geometry of the sphere allows the specular reflection, occurring at an angle of 0° between the surface and the incident beam of light, to escape from the integrating sphere without being detected. Only diffuse reflected light is detected and collected.

In semiconductor materials, an abrupt change in reflectance or absorbance can be related to electronic transitions from the valence to the conduction band. Absorbance and reflectance in this kind of measurement are specular, with total reflectance for wavelengths at which the sample absorbance is null, and vice-versa. The optical band gap can be approximately estimated from the typical absorption edge appearing in the absorbance spectrum of semiconductor materials. More refined calculations have been developed using mathematical function incorporating the absorption coefficient of the material. The common expression for band gap determination is Tauc's function:^[81]

$$(h\nu\alpha)^{1/n} = A(h\nu - E_g) \quad (\text{eq. 2.19})$$

where h refers to Planck's constant ($6.626 \times 10^{-34} \text{ J}\cdot\text{s}$), ν refers to frequency selected by the instrument monochromator, α is absorption coefficient, E_g is the band gap and A is a proportionally constant. n is a coefficient depending on the type of electronic transition. If the band gap transition is indirect or direct, the correspondent value of n will be to 2 or $1/2$, respectively. E_g can be estimated plotting the left hand side of equation 2.19 against the energy $h\nu$ (in eV), which is related to the wavelength in nm by the simple expression $h\nu = 1239.7/\lambda$. The intercept of the linear part of the resulting curve with the X-axis gives the value of E_g .

In a diffuse reflectance measurement, the absorption coefficient can be substituted by a function of the reflectance defined as the Kubelka-Munk function:^[82]

$$F(R) = \frac{(1-R)^2}{2R} \quad (\text{eq. 2.20})$$

In this function, R is the absolute reflectance (not the percentage value). F(R) hence replaces the α in Tauc function.

Conventionally, the intercept is drawn using the tangent to the straight part of the curve, calculated using the point of inflection as the tangent origin. The inflection point can be easily identified using the derivative of the Tauc function.⁸³

If the minimum energy state in the conduction band and the maximum one in the valence band have the same momentum, the semiconductor band gap is defined as direct, with corresponding electronic transitions therefore not involving a change of momentum. By absorbing the energy of a specific photon, the electrons could directly jump into the conduction band from the valence band. Conversely, a semiconductor has indirect band gap if the transition involves a change of momentum, such as the absorption of a phonon, to pass from the maximum of the valence band to the minimum of the conduction band.

Powdered samples were spread uniformly on white filter paper for diffusion reflectance measurements. For a proper measurement of the diffuse reflectance, the optical beam should hit only the part coated and the filter should not have strong absorption in the analysed spectral region. The filter has a weak absorption band at *ca.* 1200 nm, which is usually noticeable only

when measuring white materials. In all the other cases, the absorption of the sample totally covers the signal of the filter paper. All measurements were performed using a Shimadzu UV-2600 spectrometer, provided with an ISR-2200 Integrating Sphere Attachment. The spectra were analysed using MS Excel and Origin 9.0 for the implementation of the Kubelka-Munk functions and the calculation of the band gap.

2.4.2 UV-Vis absorbance of organic dye solutions

Controlled degradation of an organic dye is one of the methods used for testing the photocatalytic properties of a material. According to the material's capacity to absorb photon at certain wavelengths, the test can be performed under different irradiation frequencies, including UVC, UVA and visible light. Low-power blacklight bulbs, high-power low-pressure mercury vapour lamps and Xenon lamps, with spectral emission which is the closest to solar irradiation on Earth, are the most used sources of light employed on dye degradation test.^[84] Organic dyes are well-known to present strong absorption at specific wavelengths due to the electronic structure of the molecule, where conjugated π systems, promote stable transitions of delocalised electrons. The most common absorption process involves electron transfer from a π bonding orbital to a π^* antibonding orbital. Common organic dyes used in such tests are Rhodamine B, methylene red and methylene blue (Figure 2.6).

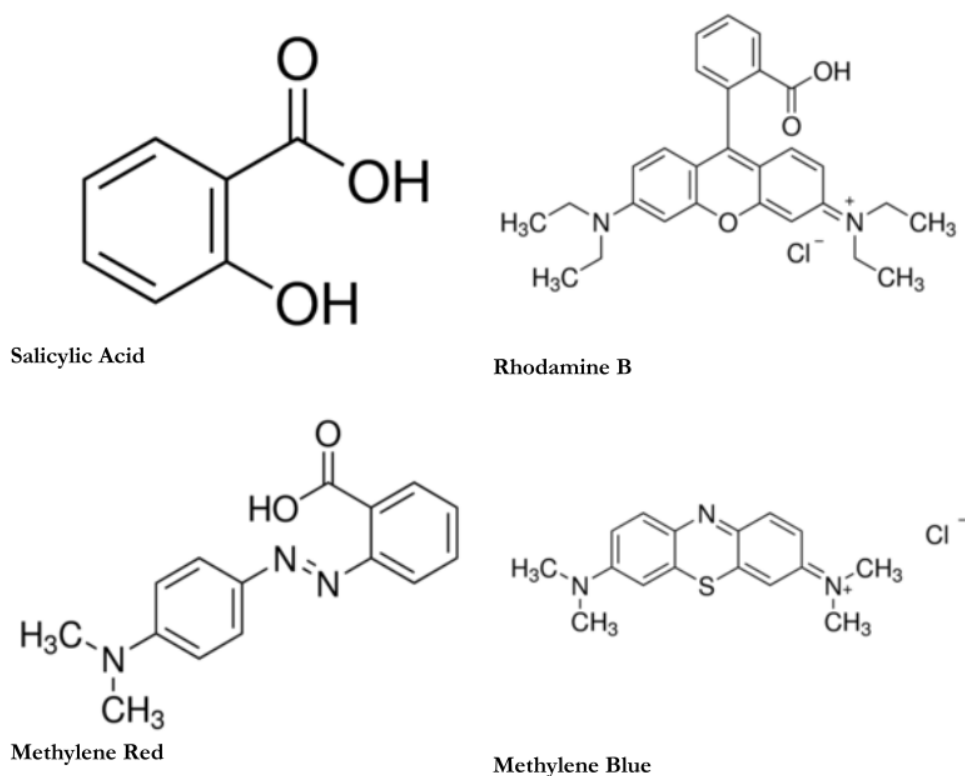


Figure 2.6: Examples of the organic dyes used for degradation testing

For example, Rhodamine B has an absorption peak at *ca.* 554 nm (Figure 2. 7). The decrease of the intensity of the peak indicates an efficient degradation process. Most of the dyes show their absorption peaks in the visible light region.

Because of this, the macroscopic effect of the degradation of these molecules is a progressive decoloration of the system in which they are dispersed. Salicylic acid was also used for particular tests, in which the source of light can be absorbed by the dye rather than the photocatalyst. Aqueous salicylic acid solutions are transparent, with strong absorption in the near-UV. The degradation of this acid can only be followed by spectroscopic methods (UV-Vis) or detection of the mineralised components (for example Total Organic Carbon –TOC- analysis).

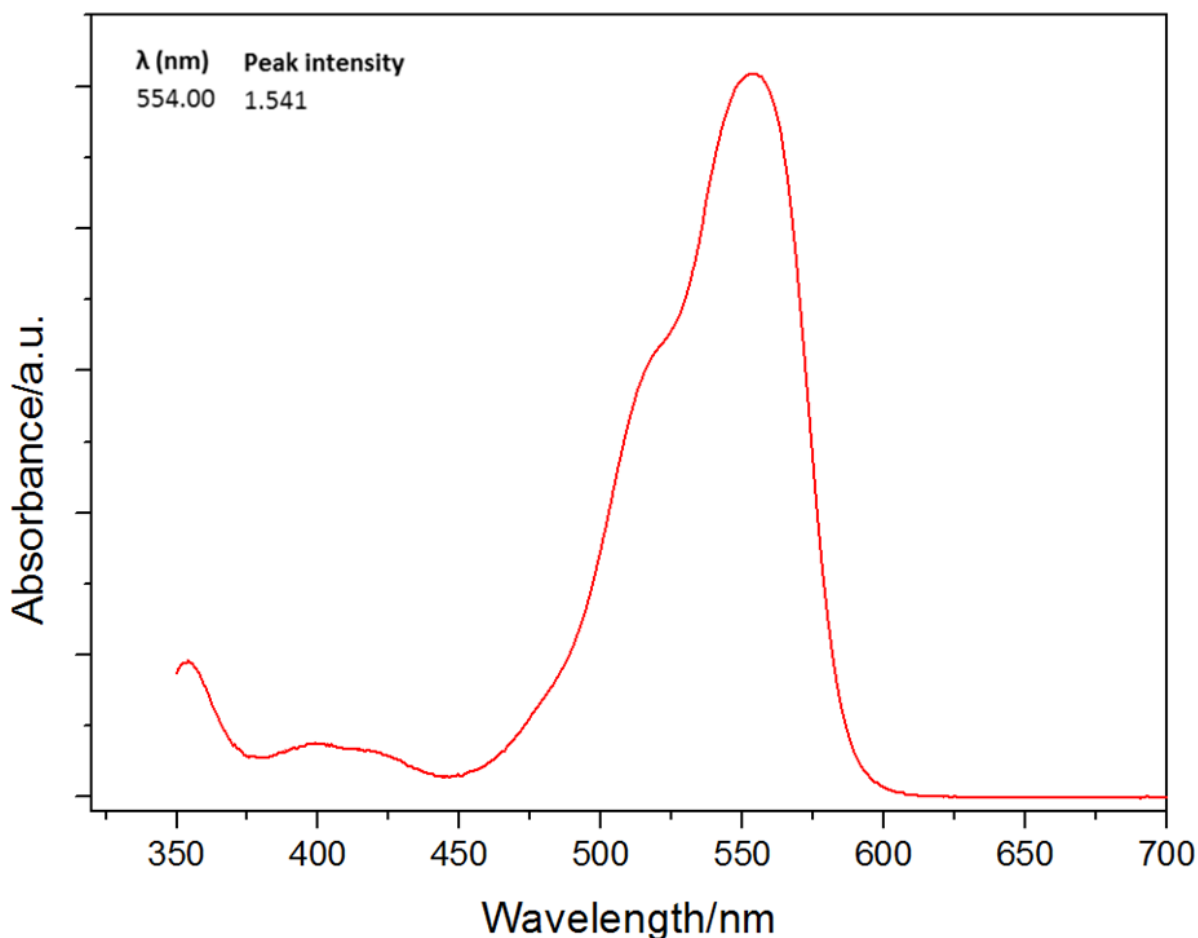


Figure 2. 7 Rhodamine B absorbance spectrum

The absorbance of the sample is related to the amount of material. In aqueous solution, the latter quantity is indicated by the concentration of the solution.

The general absorption behaviour is described by the Beer-Lambert law:

$$A = \log_{10} \left(\frac{I_0}{I} \right) = \epsilon c L \quad (\text{eq. 2.21})$$

where A is the absorbance, I_0 refers to intensity of the incident light and I is the intensity of the light transmitted by the liquid sample. ϵ is the wavelength-dependent molar absorptivity coefficient while c refers to solution concentration and L refers to path length.

The absorbance of a liquid sample is measured using a UV-vis spectrometer in a double beam configuration in which two beams of light of equal intensity are

sent to a reference (generally the pure solvent in which the sample is dissolved/dispersed) and to the sample, collecting both the transmitted beams and calculating the absorbance by intensity difference. If the degradation process is successful, the absorbance of Rhodamine B will decrease which corresponds to a lower concentration in solution.

Rhodamine B solutions were prepared using very low concentrations, enough to colour the solution and give a strong absorption signal while avoiding saturation or a non-linear response of the spectrometer detector (which would nullify the direct correlation between intensity and solution concentration). The standard concentration for Rhodamine B solutions was around $1.5 \cdot 10^{-5}$ mol·L⁻¹. A direct relationship between solution concentration and absorbance peak intensity can be established. This relationship facilitates the comprehension of the degradation kinetics, correlating the physical phenomenon with the actual reduction of molecules in solution. A calibration curve for Rhodamine B was previously calculated, correlating between intensity and concentrations as:

$$C = \frac{I_t - 0.0382}{0.0958} \quad (\text{eq. 2.22})$$

Where I_t refers to the intensity of the absorbance peak. The linear response of the instrument allows the observation of degradation phenomena within the concentration range of $4 \cdot 10^{-5}$ - $5 \cdot 10^{-7}$ M.

Using the concentration values, the degradation rate $D_t\%$ can be calculated using the following expression:

$$D_t\% = \frac{(C_0 - C)}{C_0} \times 100\% \quad (\text{eq. 2.23})$$

where C_0 refers to initial solution concentration and C the concentration at a certain exposure time. The photocatalytic properties of the material can be hence expressed in terms of degradation rate or residual concentration ($100\% - D_t\%$).

In this project, the photocatalytic material was dispersed in the Rhodamine aqueous solution ($1.5 \cdot 10^{-5}$ M) at a concentration of 1 g/L. The solution was sonicated for 10 minutes and stirred under darkness for at least 1 hour. The solution was then poured into two 250 ml beakers and placed under a UVA black light bulb (Lightech G20 T10, 20W power) or exposed to a fluorescent tube lamp (for visible light). The solutions were stirred during the whole degradation period. After set times, aliquots of the solution were collected, and centrifuged to separate the solid fraction. The absorbance of the resulting solution was measured by UV-vis spectroscopy. The plotting of the maximum absorbance peak intensities as a function of the exposure time provided the characteristic degradation curve of the material.

2.5 Thermal Analysis (TGA, DTG)

Thermal analysis generally embraces a category of techniques used for the investigation of the chemical and physical properties of a sample as a function of time and temperature. A program might include heating, cooling and/or constant temperature operations. The temperature change can be performed under controlled atmosphere, with the aid of an inert or reactive carrier gas removing the products generated by the effect of the program on the sample (e.g. decomposition, dissociation, release of smaller fractions, etc.)

Specifically, in this project two thermal analysis methods were used, Thermogravimetric Analysis (TGA) and Differential Thermal Analysis (DTA). Both these two techniques can be employed together, in Simultaneous Thermal Analysis (STA). STA allows the correlation between the data obtained from DTA and TGA, which in principles enables easy the identification and classification of specific thermal events.

Thermogravimetric (TG) analysis measures the variation of the mass of a sample as a function of temperature. The mass of the sample is compared with the mass of a standard, usually corresponding to an empty portable sample holder very similar to the one used to contain the sample. The mass variation can also be measured as a function of the time related to the thermal program. The system that measures the mass is called thermobalance and its setup is shown in Figure 2.8.

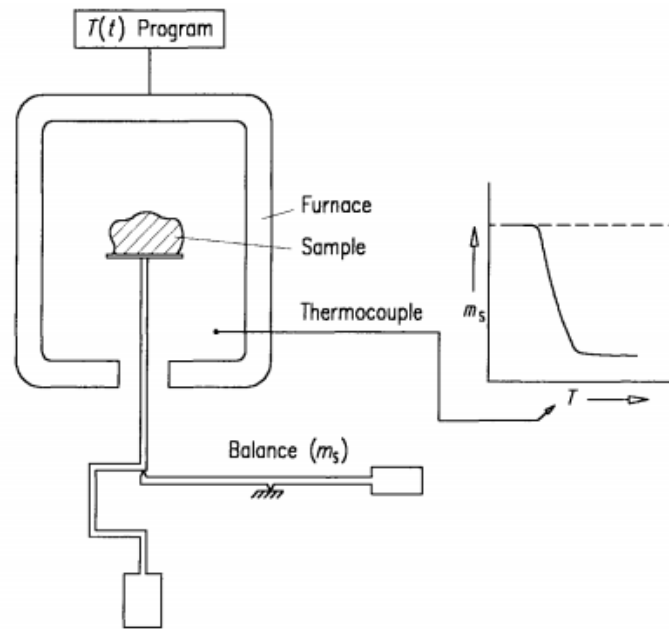


Figure 2.8: Thermo-balance setup [85]

Differential thermal analysis (DTA) investigates the temperature difference between the sample and the reference under identical heating conditions (Figure 2. 9).

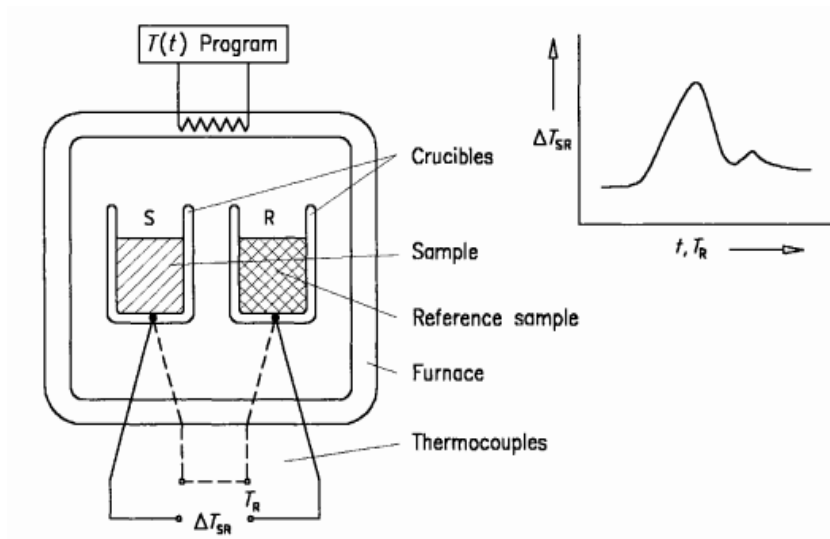


Figure 2. 9 DTA measuring system structure. Furnace under protected atmosphere (left) and DTA signal (right)

The DTA system provides useful information regarding the stability of materials as a function of temperature, for example. The DTA output signal consist of the

difference between the sample and the reference temperature $\Delta T_{SR} = T_S - T_R$. The final results of DTA are reported in the form of a curve of values of power per mass as a function of temperature or time.

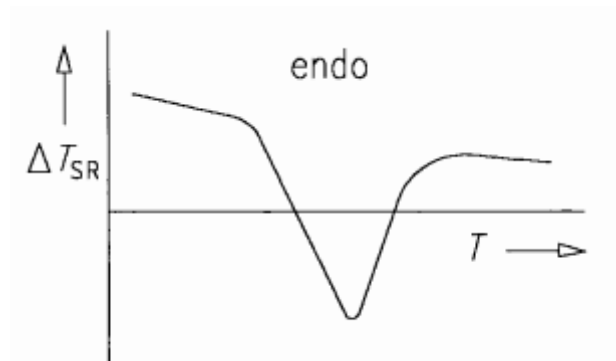


Figure 2.10: DTA curve with peak representing an endothermic effect

A Netzsch STA 409 PC Luxx instrument was used for the STA measurements. The operations were performed working under an argon atmosphere (BOC, 99.998%) inside a glovebox ($H_2O < 0.5\text{ppm}$, $O_2 < 0.5\text{ppm}$, UNILab, MBraun). A constant flux of argon was used as carrier gas. Before the measurements, the temperature programme was set to create a correction file which contains the experiment parameters such as starting temperature, heating and cooling rate and dwell time at constant temperature. The correction file is used to record the behaviour of the instrument under the temperature program, run using a second reference instead of the sample, in order to eliminate potential systematic errors (e.g. mass instability of the balance, buoyancy, etc...). Typically a measurement requires not more than 15-25 mg of sample. The sample is placed in the sample holder (a specifically designed alumina crucible), mounted inside the heating chamber, which is connected to the thermobalance.

In this project, the conditions for the formation of Zn_2NF were tested using the STA program to simulate the synthesis conditions while following the mass

change and the various the thermal events that occur during the reaction. A stoichiometric mixture of Zn_3N_2 and ZnF_2 finely ground powders was used as starting material. The correction file was set up using a starting temperature of 30 °C, with a heating rate of 5 °C/min, setting different final temperatures. The analysis of the TGA and DTA data were processed using the Proteus Analysis software, associated with the instrument.

Mass spectrometry

Mass spectrometry (MS) is an analytical technique based on the ionisation of chemical species and their classification according to their mass to charge ratio. In the setup used in this work, the mass spectrometer is coupled with the STA apparatus and used for the analysis of the evolved gas during the thermal program. Samples undergo ionisation when bombarded by an electron beam, leading to the generation of positive charges by electron loss. The further application of an electric field (\vec{E}) and a magnetic field (\vec{B}) accelerate the ions and separate them according to their different mass-to-charge ratio (m/z). The selection of the ions is described by the combination of Newton's second law of motion (eq. 2.24) and Lorentz's law (eq. 2.25):

$$\vec{F} = m \cdot \vec{a} \quad (\text{eq. 2.24})$$

$$\vec{F} = z \cdot (\vec{E} + \vec{v} \times \vec{B}) \quad (\text{eq. 2.25})$$

where \vec{F} is the force from the fields and \vec{v} and \vec{a} are the velocity and the acceleration of the ions, respectively.

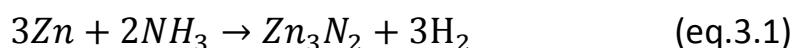
In this project, a Hiden Analytical HPR 20 mass spectrometer was used. The instrument was based upon a quadrupole mass spectrometer designed for fast transient gas detection and used for gases analysis evolved during STA

programs. The quadrupole consists of a pairs of rods connected oppositely to each other and to which a radiofrequency (RF) and a direct current (DC) potential are applied. The ions travel through the channel formed by the rods, while the DC potential selects the ions with the desired m/z . These ions are able to pass through the channel without colliding with the rods to reach the detector. The analysis was controlled by the MAsoftware Pro software package associated with the instrument. Detection of argon as carrier gas was always monitored.

Chapter 3: Zinc nitride

3.1 Zinc nitride synthesis

Zinc nitride is a small band gap semiconductor which has attracted attention due to its outstanding electronic properties. Since the first synthesis reported in 1940 by Juza *et al.*,^[49] Zn₃N₂ has been produced using different methods. The most common is the ammonolysis of metallic zinc at high temperatures, which proceeds as follows:



However, many such reactions fail to yield pure Zn₃N₂, with final products containing ZnO or Zn impurities. Improvements in the synthesis of Zn₃N₂ synthesis have been investigated over the past few decades.^[52–55,86] In this research project, Zn₃N₂ powder was successfully synthesised by the above ammonolysis reaction, limiting the quantity of impurities. The experimental work focused on the increase of nitride purity, limiting the formation of ZnO and understanding the mechanism of the impurity generation.

For the synthesis of Zn₃N₂, 2 g of zinc powder (STREM, 99.9%) were placed in an alumina boat for the ammonolysis reaction. The reaction temperature was set to 600 °C for a duration of 12 hours. The ammonia flow rate was set at 500 ml/min for all of the initial purge of the tube furnace, the heating ramp and the treatment at constant temperature. For the cooling phase, the flowing gas was switched to Ar following the reaction protocol reported by Paniconi *et al.*^[54] After the reaction, the final product appeared as a powder of two different colours, reddish-brown and black. The colour change was gradual in the alumina boat along the direction of the flowing gas. Further reactions show the

regular occurrence of this phenomenon, with black powder forming towards the gas outlet and lighter brown powder remaining in the part closer to the ammonia inlet, as shown in Figure 3.1. The sample was carefully taken out from the boat and the two distinct products separated and ground using a mortar and pestle. During the separation, a further gradient of colour was observed in the samples as a function of depth, with the outermost layer appearing brown and the inner deep layer showing black coloration. According to previous work in literature, the black powder is Zn_3N_2 , while the orange-brown residue contains partially reacted ZnO .^[46]

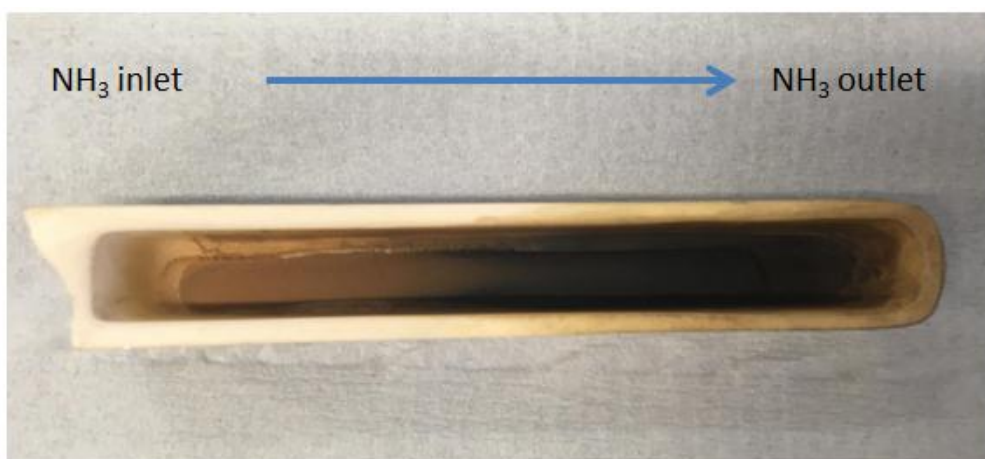


Figure 3. 1 Zn_3N_2 synthesis reaction products in the alumina boat as removed from the furnace after cooling

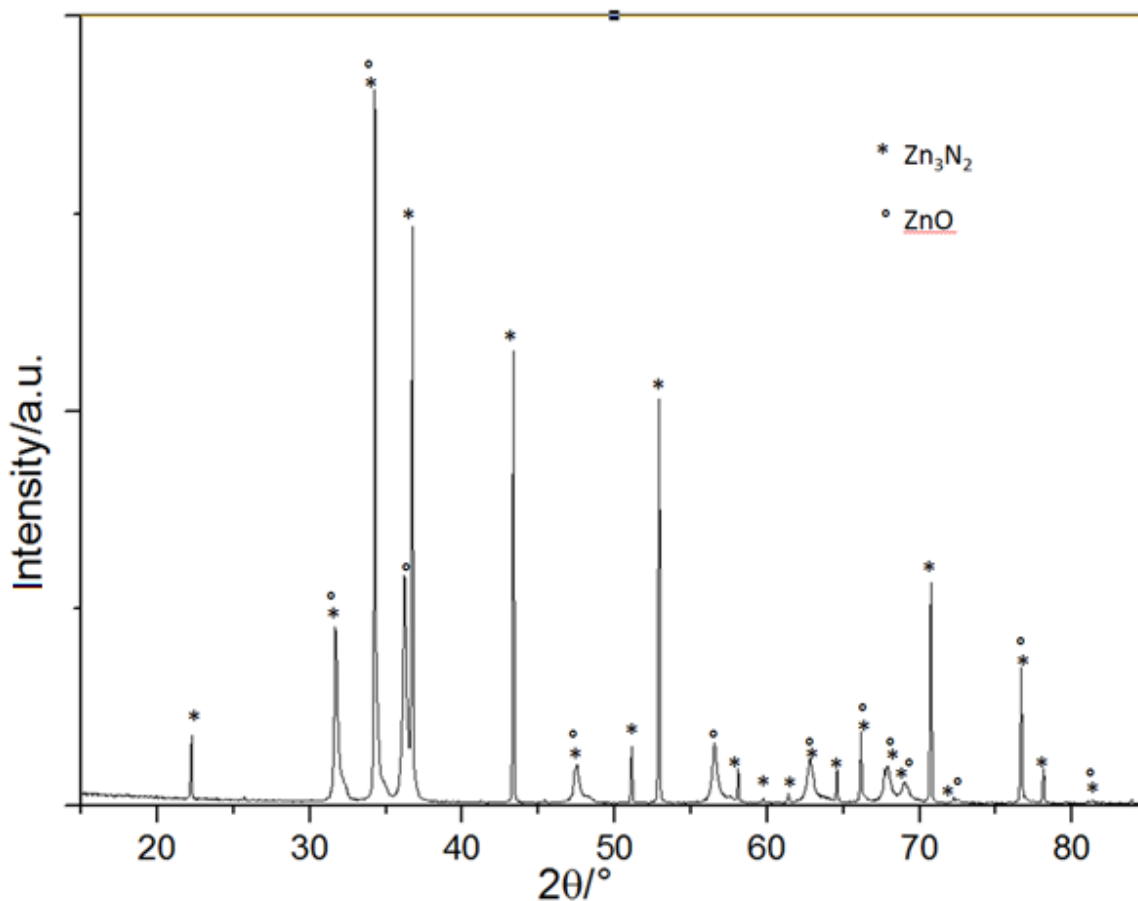


Figure 3.2: XRD pattern of the brown/black mixed powder product

In Figure 3.2, the PXD pattern of the brown and black powder mixed together showed two different phases, with Zn_3N_2 as the principal phase but a consistent presence of ZnO, confirming the biphasic nature of the mixture. As expected, the synthesis performed following the protocol previously reported in the literature resulted in the formation of ZnO impurities.

Some of the peaks from Zn_3N_2 overlap with those of ZnO. Peak overlapping is apparent from the appearance of asymmetry in the peak shape or the presence of a small convoluted peak on the edge of the main signal. Two isolated and relatively strong ZnO peaks were considered, the (101) reflection at *ca.* 36.14° and the (110) reflection at *ca.* 56.52° , to estimate the relative amount of the two phases. Of these the (101) is the most intense XRD

reflection of ZnO and can be used as a reference for the calculation of the ZnO content in the sample.

The formation of a mixture of two different products from the ammonolysis reaction of Zn powder was previously reported by Lingampalli *et al.* [46] The authors suggested separating the black powder, associated with the formation of Zn₃N₂, and ammoniating it. The reaction was cycled three times according to this protocol to obtain an acceptable purity. However, even after this process, the presence of a small amount of ZnO impurity seems to be unavoidable. Despite the difficulty in separation of the ZnO orange-brown powder from the black Zn₃N₂, the products were collected and characterised independently as well as possible.

In an attempt to reduce the amount of impurities, different reaction conditions were considered, focusing on the reaction temperature and duration, heating rate, ammonia flow rate, crucible material, cooling atmosphere and cooling rate. In order to reduce the presence of oxygen from the precursor material, brand new pure Zn powder was used, which was stored under a protected atmosphere (N₂-fed glovebox) and transferred directly to the tube furnace, limiting as far as possible, its exposure to air. Excluding the eventual oxidation of the powder surface (occurring for all metal surfaces), the identification of other possible external sources of oxygen became the critical point for the reaction optimisation.

For the modification of the synthesis conditions, a review of the previous work on Zn₃N₂ showed an optimal reaction temperature between 500 - 600 °C, with a treatment time ranging from only 2h to 168 h. [46,53–55,86,87] All the initially tested conditions for the synthesis optimisation are listed in Table 3.1. The resulting PXD patterns of the products are shown in Figure 3. 3.

Table 3. 1: Experimental conditions for Zn₃N₂ synthesis by ammonolysis

	Temperature/°C	Duration/ h	Crucible material	Cooling gas
1	400	10	Alumina	NH ₃
2	500	10	Alumina	NH ₃
3	600	12	Alumina	Ar
4	600	12	Graphite	Ar
5	600	2	Alumina	Ar
6	600	12	Quartz	Ar

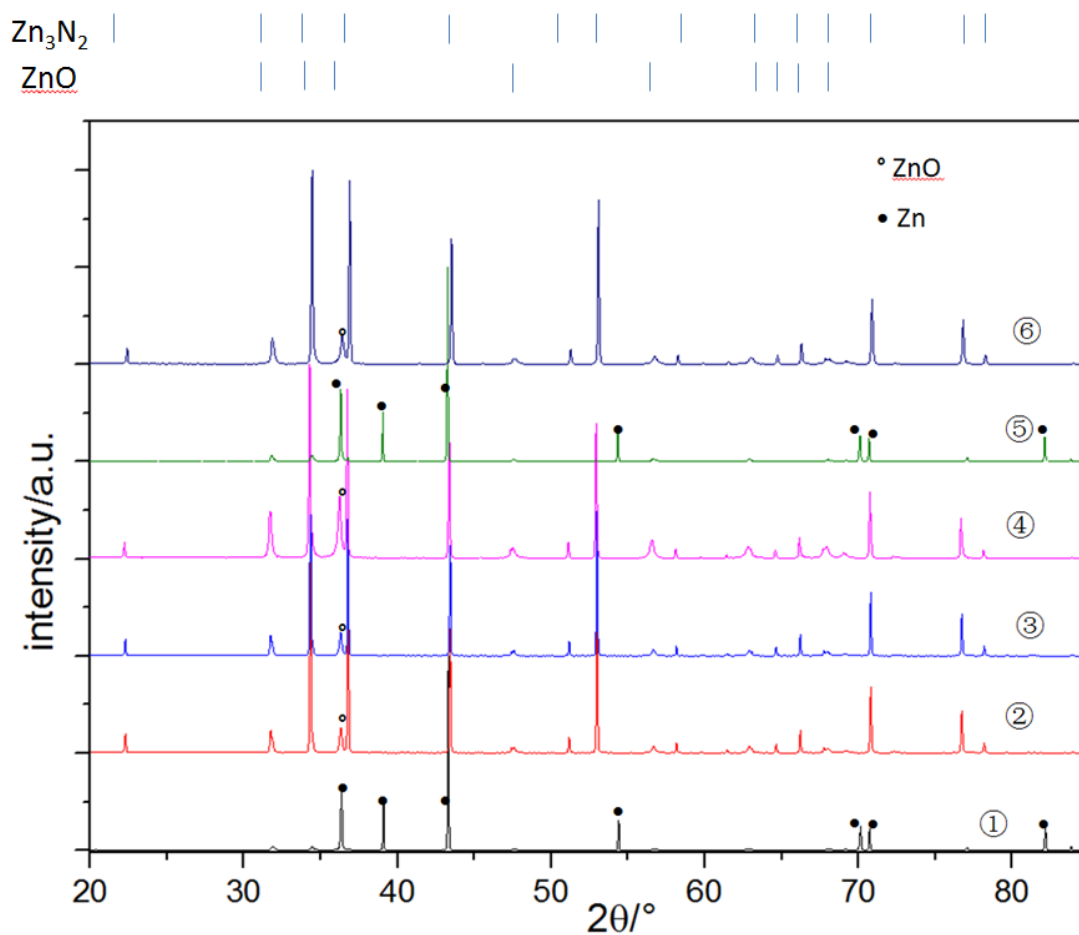


Figure 3. 3 PXD patterns of the products following the synthesis conditions listed in Table 3. 1. “○” marked the most intensity peaks for ZnO and “●” marked Zn

In this set of experiments, only the black portion of the sample was retained for analysis, since this was considered to be the phase of interest (Zn_3N_2 powder). Considering the various reaction conditions, a reaction temperature of 400 °C (reaction 1) or treatment time of 2 hours (reaction 5, following the protocol used by Lingampalli et al.^[46]) are not acceptable conditions for the synthesis of Zn_3N_2 , since Zn appeared as the main phase with a very low amount of Zn_3N_2 being formed. Conversely reaction temperatures between 500-600 °C associated with treatment times of 10-12 hours gave better results, confirming the most appropriate temperature window for the optimal synthesis of Zn_3N_2 .

The crucible material can also affect the outcome of the reaction. This is due to the different dissociation kinetics of NH_3 in presence of different materials. In our experiments, the use of alumina and quartz crucibles resulted in purer products compared to the sample reacted in graphite crucibles (reaction 4). However, the purity is related to the black powder only, since for all the reactions a certain amount of orange-brown ZnO was always present conditions, with difficult to quantify the relative amount of the two different products. Although cooling atmospheres of NH_3 and Ar showed similar product compositions, the amount of ZnO impurities is slightly lower after Ar-cooling compared with cooling under the reaction gas (NH_3).

The modification of the synthesis conditions resulted in slight improvements of Zn_3N_2 synthesis. Despite this, the presence of ZnO impurities and the formation of two distinct products was still an issue for further development of the project. Attention focused on the possible sources of oxygen. For instance, the crucible material contains oxygen in its lattice structure or simply present in the surface. However, the results using a graphite crucible, which should not

contain oxygen, were no better than the reactions performed in alumina or quartz boats. On the other hand, the oxidation reaction with formation of the brown oxide appeared to start from the superficial layers of the material lying on the outer surface at the solid-gas interface rather than from the inner part, which is directly in contact with the crucible material (and is sufficiently in contact with the NH_3 atmosphere, as evidenced by the transformation of Zn in Zn_3N_2).

Further experiments were performed to optimise the synthesis, restricting the range of reaction temperatures between 550-600 °C, with the conditions listed in Table 3.2.

Table 3.2: Zn+ NH_3 samples prepared under refined conditions

	Temperature/°C	Duration/h	Crucible material	Cooling gas
7	550	12	Alumina	Ar
8	575	12	Alumina	Ar
9	600	10	Alumina	Ar
10 (using 9 as starting material)	600	12	Alumina	Ar

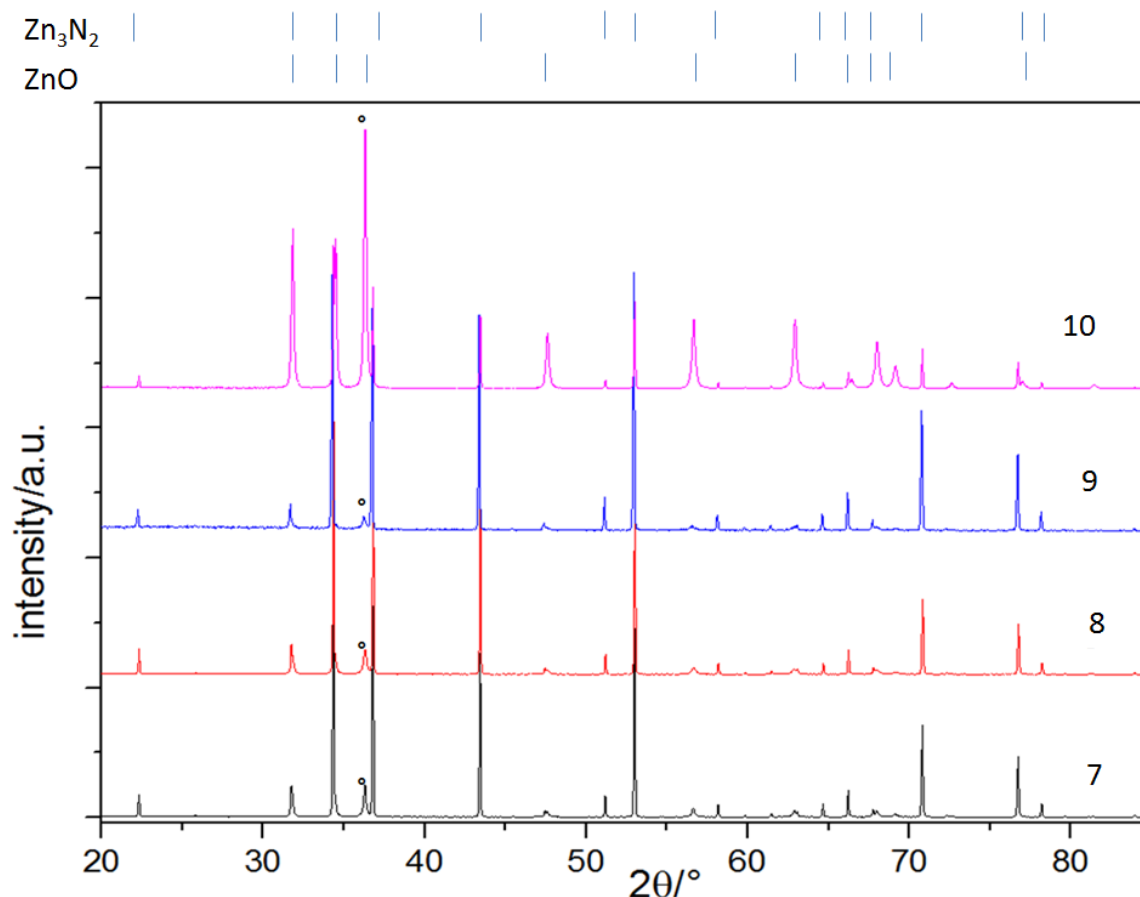


Figure 3. 4 PXD patterns for Zn_3N_2 synthesis within a narrow range of synthesis temperatures

As observed in Figure 3. 4, the restriction of the temperature range from 550-600 °C led to higher purity products. The presence of ZnO is confirmed from its the most intense reflection (101). From this set of experiments, the reaction performed at 600 °C (reaction 9) yielded the purest product. Sample 10 was made by repeating sample 9 under the conditions in Table 3.2 in an attempt to obtain higher purity and remove ZnO completely. However, the pattern for reaction 10 presented in Figure 3.4 shows a dramatic increase of ZnO content.

3.1.1 ZnO re-crystallisation

If one excludes the presence of external oxygen sources, the only viable explanation for the presence of ZnO impurities in the product is the existence of ZnO in the original Zn powder. Even the purest Zn powder contains a certain

amount (< 1%) of oxide due to superficial oxidation occurring on the metal surface. Synthesis of Zn_3N_2 involves a reaction at a temperature higher than the melting point of Zn (420 °C), and the interaction of ammonia and its decomposition products with the molten metal. Re-crystallisation of ZnO around the pre-existing oxide grains, (the melting point, of ZnO, 1975 °C is much higher than that for Zn) might be a possible explanation for the increase of the amount ZnO. The molten surface could capture residual oxygen from external sources (adsorbed water or oxygen, impurities in the gas flow, leaks in the gas line and flange system, etc.), with the ZnO grains growing from ZnO seeds depleting Zn during the constant temperature or cooling phase, when the molten metal progressively solidifies.

A simple melting-solidification cycle reaction was set for Zn powder under inert gas atmosphere to provide evidence for this possibility. The same setup previously adopted for the ammonolysis and argon constant gas flow was used, including a 1-hour purge to remove the adsorbed atmospheric gases. In this case, a certain amount of ZnO (1%) was mixed with the Zn powder and finely ground. The reaction temperature was set to 600 °C for 10 hours, in order to bring the metal above its melting point.

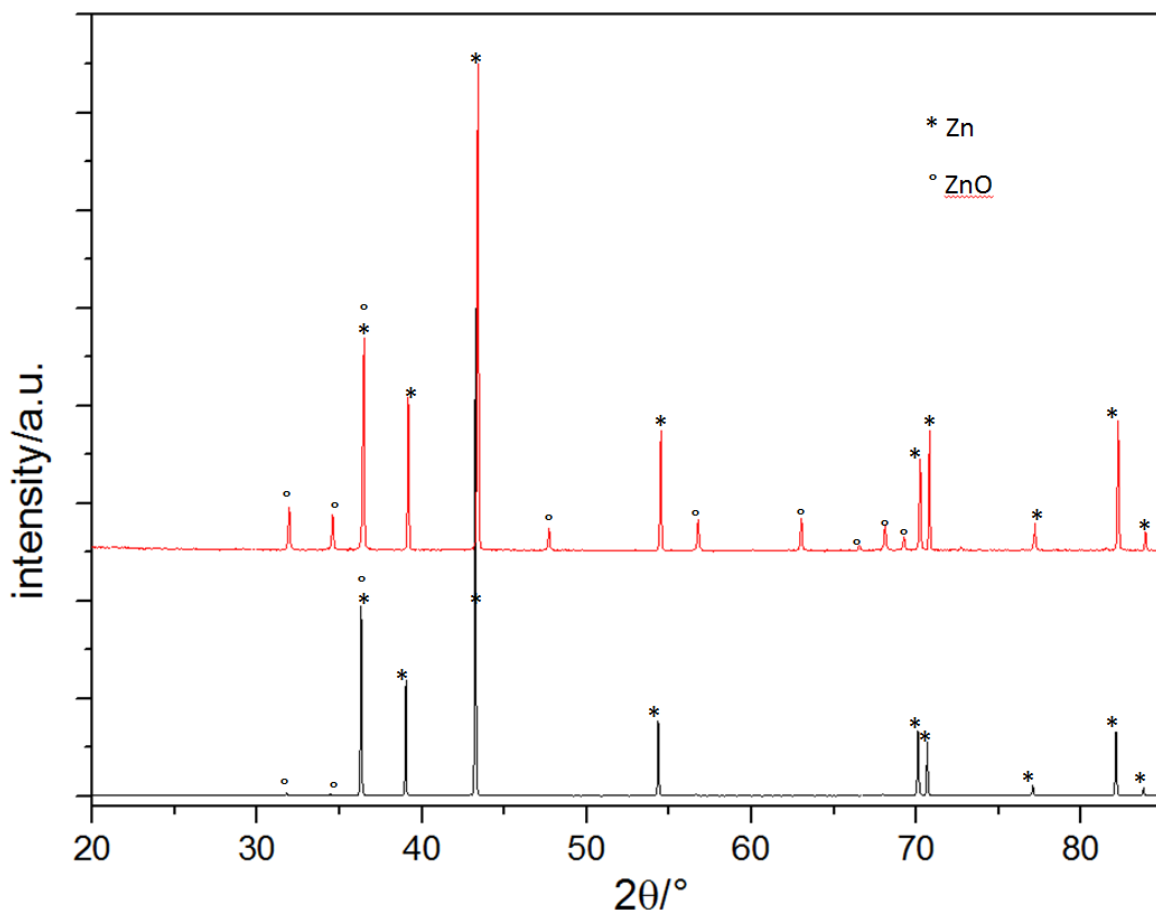


Figure 3.5: Powder pattern of Zn before and after heating under an inert atmosphere in the presence of ZnO

In Figure 3.5, the difference between the original material and the resulting product is evident. A very small amount of ZnO, can be seen the amount of ZnO increases the dramatically after the reaction. The experiment proved that ZnO can grow from molten Zn (even though the exact source of external oxygen was not fully identified). Zn_3N_2 is solid within the whole reaction temperature range, since it is reported to decompose at 681 °C.^[54] Considering the previous results, with the highest purity of Zn_3N_2 product obtained at 600 °C, it is right to suppose that grains of ZnO and Zn_3N_2 co-exist in the molten Zn at least during the first steps of the synthesis. An increase of treatment time has been reported to lead to a higher ZnO level in the final products by Paniconi et al.^[54], which releases Zn in molten state, with the ZnO free to grow without competition.

3.1.2 Quenching/accelerated cooling

Once the optimal temperature and duration conditions for the synthesis of Zn_3N_2 were identified, solidification of Zn should occur in the presence of solid ZnO during the cooling step. As already mentioned, since the solidification process needs some external source of oxygen, the cooling process became a critical factor for the optimisation of the synthesis. Changing the atmosphere to Ar from ammonia during the cooling time implied exposing the inside of the furnace to the atmosphere for a few seconds even though the chamber was supposed to be completely saturated with NH_3 . Moreover, the cooling phase (to room temperature) is relatively long, needing approximately 6-7 h, providing sufficient time for growth of ZnO at the expenses of molten Zn and consequently removing useful precursor for Zn_3N_2 . If one assumes the complete conversion of the available Zn to Zn_3N_2 , a further source of Zn may come from decomposition of Zn_3N_2 due to a change of atmosphere or instability at the reaction temperature.

Excluding a complete new design for the experimental setup, which was beyond the scope of this research project, the only aspect of the synthesis that remained to be optimised was the cooling step. Increasing the cooling rate should prevent the growth of ZnO crystals or the decomposition of Zn_3N_2 .

Thermal conditions that involve a drastic reduction of temperature from the operating value to room temperature in the shortest time possible are defined as 'quenching'. Quenching was performed using a different reaction setup, performing the reaction in a quartz tube (approximately 4 cm in diameter), closed in its upper part with a rubber septum. Zinc powder was placed into an alumina crucible placed in turn at the closed bottom of the glass tube. The

reactions took place in a vertical furnace, following the same protocol of the previously performed ammonolysis, with NH_3 being flowed inside the tube through two syringe needles inserted into the septum. After the ammonolysis reaction, the glass tube was extracted from the furnace and quenched by immersion into an oil bath. Initially, the oil bath was heated to $80\text{ }^\circ\text{C}$ in order to reduce the thermal shock and preventing the fracture of the quartz tube (which was handmade by glassblowing, and likely to contain microstructural defects). The quenching process from $600\text{ }^\circ\text{C}$ to room temperature took approximately five minutes.

As an alternative, gas cooling was also investigated. Using the same setup previously employed for the ammonolysis reactions, bespoke cooling equipment was designed to cool the Ar flow used during the cooling step. The Ar gas line was connected to a stainless steel coil, which was immersed in liquid nitrogen or in a dry ice bath. Since Ar boiling point is $-186\text{ }^\circ\text{C}$, the equilibrium temperature of liquid N_2 (boiling point: $-196\text{ }^\circ\text{C}$) would cause condensation of Ar gas and drastic expansion when the gas exits the coil, increasing the pressure of the system. Another drawback of this method is represented by the eventual thermal stress for the mullite tube of the furnace, exposed to a difference of several hundreds of degrees of temperature. Only a small section of the coil was immersed in liquid N_2 , in order to reduce the residing time of Ar gas in the coil and prevent gas condensation. By comparison, a dry ice bath has a temperature of $-78.5\text{ }^\circ\text{C}$, representing milder cooling conditions and no risk of gas condensation. Both methods led to cooling from $600\text{ }^\circ\text{C}$ to room temperature in *ca.* 30 min. All the quenching reactions performed are listed in Table 3.3.

Table 3.3: Zn₃N₂ reaction incorporating quenching methods

	Temperature/°C	Duration/h	Crucible	Method of cooling
11	600	10	Alumina boat	Liquid N ₂ /Ar
12	600	10	Alumina crucible	Oil bath Quenching
13	600	10	Alumina boat	Dry ice/Ar

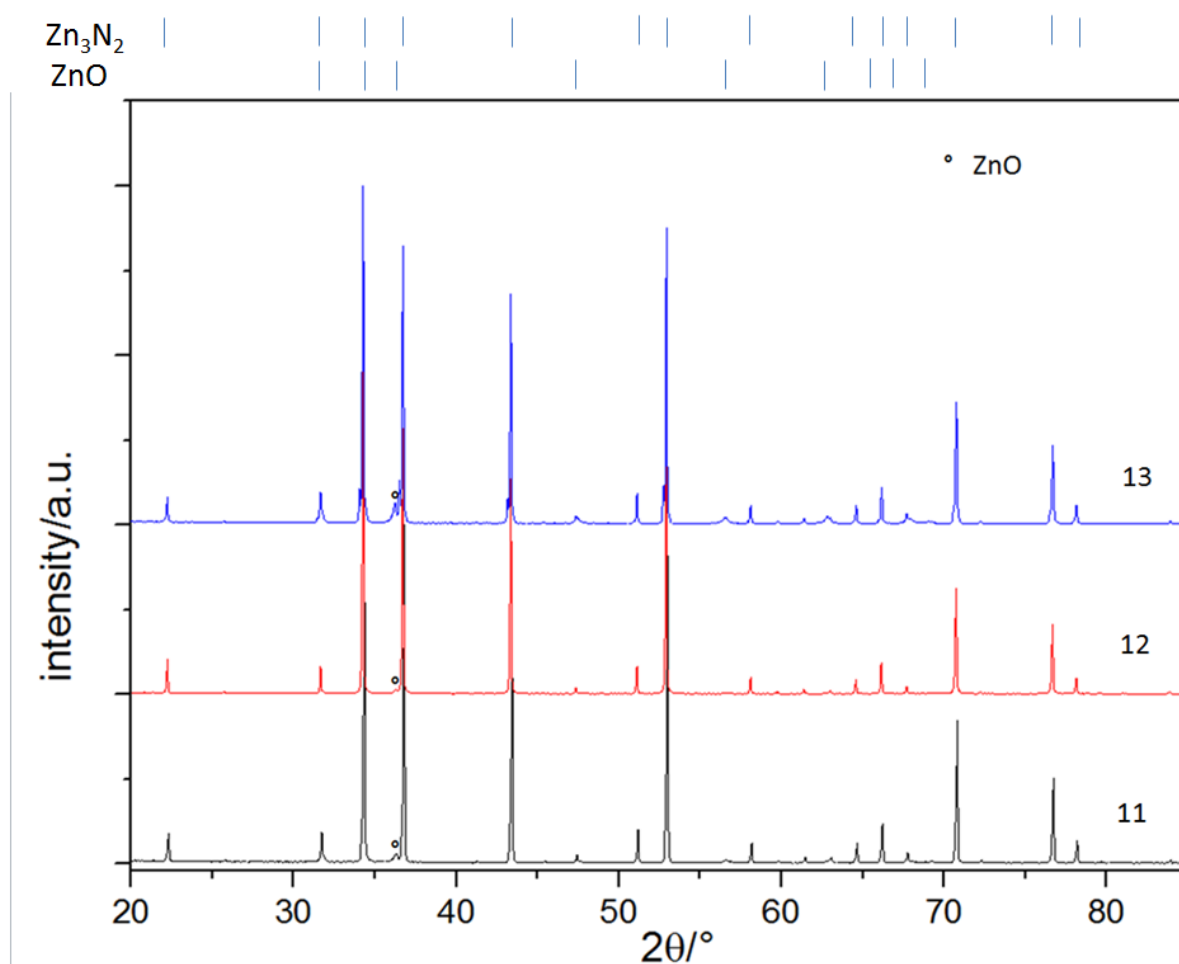


Figure 3. 6 PXD pattern of quenched Zn₃N₂ samples

From the observation of the XRD patterns in Figure 3. 6, all three quenching methods tested yielded higher purity products compared to the previous

results using a conventional cooling step. The amount of ZnO impurity is at a minimal level. Comparing the three methods, direct quenching in an oil bath (reaction 12) provided the highest purity of Zn_3N_2 product. Liquid N_2 -cooled Ar flow provided a better product quality compared to the dry ice-cooled gas flow. Both methods gave lower quantities of ZnO impurity (and consequently more Zn_3N_2) compared to experiments applying conventional Ar cooling at room temperature. The quenching experiments demonstrated the validity of the proposition that the cooling rate is the most critical factor of Zn_3N_2 synthesis. The reduction of the cooling time led to stabilization of Zn_3N_2 at the expense of the formation of ZnO. The purity of Zn_3N_2 is directly related to the rate and efficiency of cooling, for this reason the oil-bath quenching (600 °C to room temperature in a few minutes) showed better results than a liquid N_2 -cooled gas flow, which in turn is more efficient than a dry ice-cooled flow.



Figure 3. 7 : Image of the final product of the oil bath “quenching” reaction (sample 12).

The final reaction products in the vertical tube configuration were visually very different compared to the materials obtained with the earlier horizontal tube furnace setup. Instead of the usual brown-orange ZnO impurities, the vertical

configuration coupled with quenching resulted in the formation of metallic zinc spherical agglomerates. Due to the accelerated cooling rate, unreacted molten Zn solidified rapidly and without oxidation. Solidified Zn did not come back to its original powder form, producing the spherical agglomerates shown in Figure 3.7.

The incomplete reaction of Zn, despite the optimal temperature and duration of the treatment, might be likely due to the distribution of the reacting gas in the setup. In this configuration, the ammonia flow was likely not complete around the zinc powder, given that both the inlet and outlet were located at the top of the tube. Only the upper layer of the material in the crucible underwent efficient nitridation, producing Zn_3N_2 . The lower part of the Zn starting material could not interact with ammonia so easily, solidifying into a metallic form after quenching. This experiment would suggest that ZnO impurities seen in previous experiments could originate from the surface layer of the molten Zn and that the oxygen source probably originates in the flowing gas, since in this last reaction the oxygen-free atmosphere was preserved from the beginning until the end of the process. Metallic Zn spheres and Zn_3N_2 can be easily separated, with the possibility of using the residual zinc in further ammonolysis reactions, providing higher purity Zn_3N_2 compared to the other methods tested or reported in the literature.

Figure 3.8 shows a comparison between our purest Zn_3N_2 product and the best result reported to date in the literature.^[46] The typical ZnO peak, marked with a black circle in the patterns, is significantly reduced in the Zn_3N_2 produced by the quenching method. In conclusion, the cooling rate is an essential parameter to be considered for the optimisation of the Zn_3N_2 synthesis. It is during the

cooling step of the reaction that the ZnO impurities are most likely to appear.

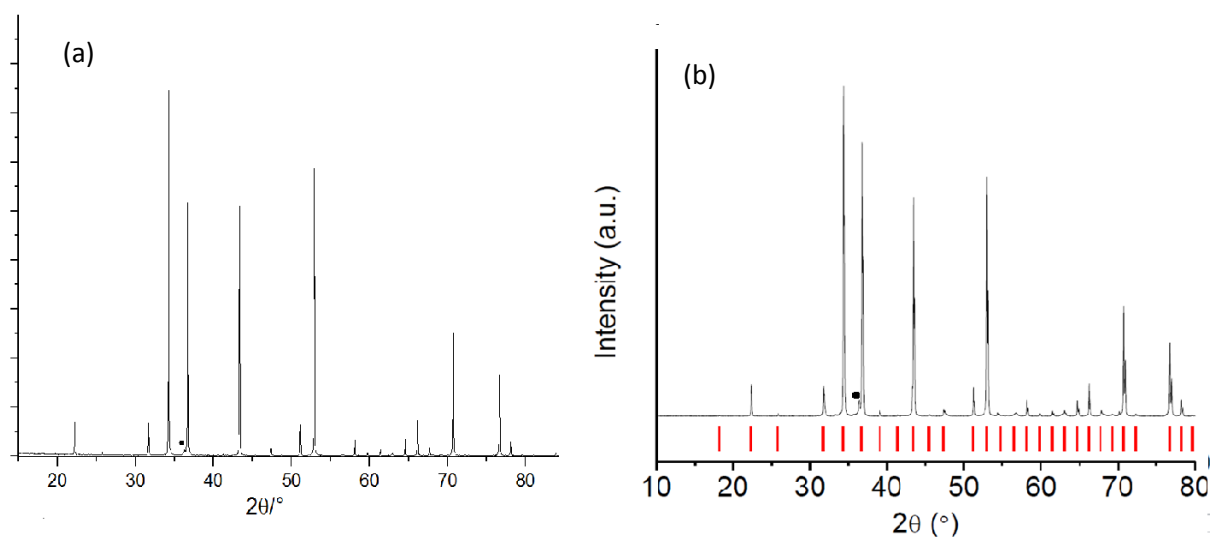


Figure 3.8: Zn₃N₂ XRD pattern comparison. (a) Product synthesised herein by quenching method, (b) Zn₃N₂ powder reported in the literature.^[46]

Among all synthesis methods, oil bath quenching and liquid N₂ cooling methods produced Zn₃N₂ products of outstanding quality. The products of these two synthesis methods were selected as precursors for the subsequent synthesis of Zn₂NF.

3.1.3 Microwave-assisted ammonolysis

As described in the previous sections, thermal ammonolysis is the most common and efficient method for the synthesis of Zn₃N₂. However, reaction times are relatively long, despite some reported reactions of only 2 h^[55] which could not be reproduced in this project. A constant flow of ammonia is required throughout the reaction, which is a cause for environmental concern due to its toxicity and corrosive power. The energy consumed for the furnace heating and the cost of the neutralisation of the ammonia outgas have added further economic and environmental implications, that would affect the scale-

up of the reaction (the general yield for the best reactions is less than 40% compared in terms of the original mass of Zn).

A simple way to make the process more environmentally friendly might involve shortening the reaction time. The application of microwave irradiation in solid-state chemistry is a promising method to achieve the reaction durations of only a few minutes and, because of the accelerated heating rate. It is possible to access metastable phases or materials otherwise difficult to synthesise by conventional thermal methods.⁸⁸

Microwave (MW) synthesis was applied to the ammonolysis of Zn powder. The experimental setup was similar to the vertical configuration used to study the effects of quenching on the Zn_3N_2 synthesis. A quartz tube was dipped in a beaker filled with SiC powder. SiC is a microwave susceptor, a material that couples with microwave irradiation and efficiently converts this into heat. Zn powder is also able to interact with microwave, since metallic elements generate heat by atomic conduction. The tube was filled with NH_3 gas via syringe needles (one for the inlet, the other for the outlet) inserted in the rubber septum isolating the tube from the surrounding atmosphere. The quartz tube, together with the SiC beaker, was placed into a multi-mode MW cavity, designed by modifying a domestic MW oven (DMO) with a maximum output power of 700 W.

Optimising the reaction time is one of the main issues of the application of MW irradiation in solid-state reactions. Due to the fast heating, it is easy to exceed the optimal window of temperature for the production of a product (in this case Zn_3N_2). The upper temperature for the reaction with molten Zn, excluding the decomposition temperature of Zn_3N_2 at 700 °C, is represented by the boiling point of Zn 907 °C, even though the Zn vaporisation can occur at lower temperature (*ca.* 400 °C in particular cases ^[60]), which is perhaps the

main reason of further loss in final product yield after nitridation by ammonolysis. Constant power MW irradiation was continuously applied for tired of 5 and 10 minutes. For longer times, evaporation of Zn and its re-condensation on the quartz tube wall was observed. In other attempts, the MW heating was repeated several times for shorter periods, in order to prevent Zn evaporation, Sample 16 was subjected to four 3 minute heating periods denoted 3+3+3+3 in the table.

Table 3.4: Microwave-assisted synthesis conditions for Zn₃N₂

Sample	Microwave heating duration/min
14	10
15	5
16	3 + 3 + 3 + 3

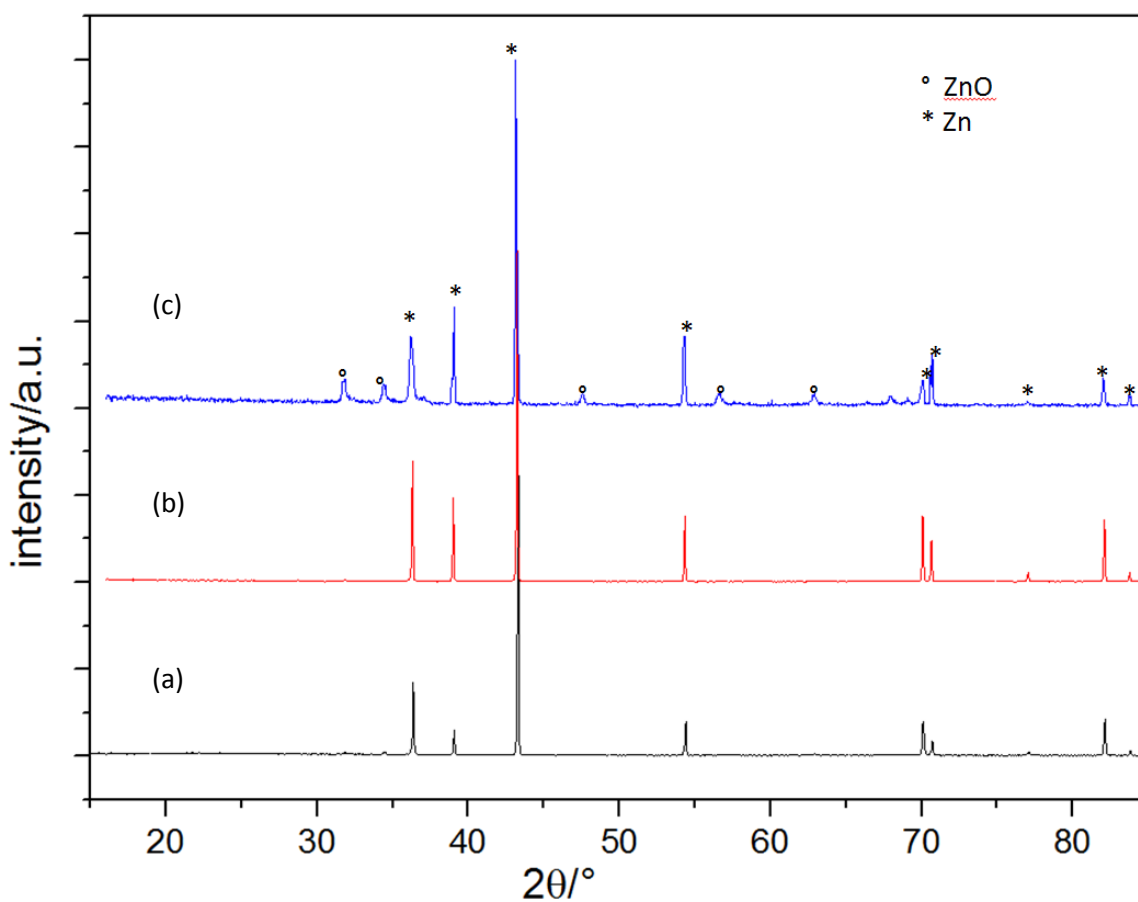


Figure 3.9: XRD patterns for microwave-assisted synthesis of Zn_3N_2 at different experimental conditions (list in Table 3.4) (a) sample 14, (b) sample 15, (c) sample 17.

None of the reactions produce Zn_3N_2 . Constant power irradiation ((a) and (b) in Figure 3.9) produced unreacted Zn, together with a large amount of Zn condensed on the tube inner wall. In a cycled reaction, ZnO appeared, probably due to the heating-cooling mechanism similar to the one observed for the standard cooling conditions. The main issue for the efficient MW synthesis of Zn_3N_2 is the temperature control, with the MW irradiation leading in most cases to vaporisation of the precursor, preventing the reaction with NH_3 . The reaction is also affected the poor distribution of the ammonia flow, as witnessed using this experimental setup previously (see section 3.1.2).

3.2 Morphological and elemental analysis

The high purity Zn_3N_2 produced using the accelerated cooling methods (described in section 3.1.2) were further characterised. SEM analysis and EDX spectroscopy were used to characterise the morphology and the elemental composition of the Zn_3N_2 powders respectively.

Figures 3.10 and 3.11 show SEM images of Zn_3N_2 synthesised by the oil-bath quenching method. The morphological analysis of this material evidenced the presence of highly crystalline particles, that account for most of the sample. The remainder of the material consists of irregular structures with uneven surfaces.

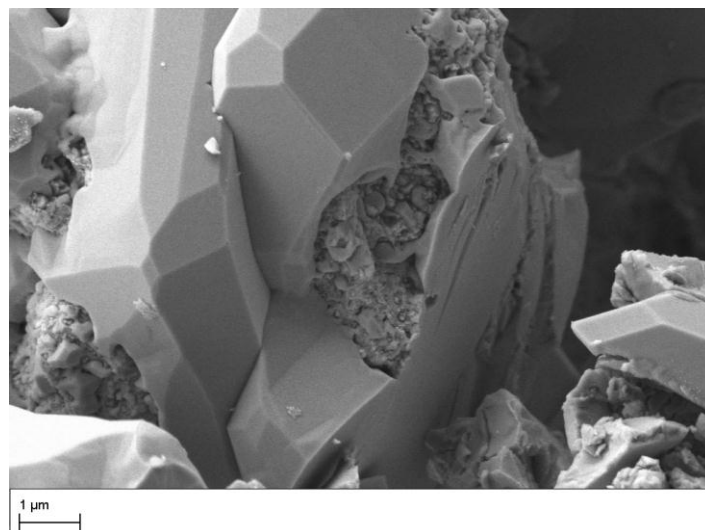


Figure 3.10 SEM image of Zn_3N_2 synthesised by quenching method

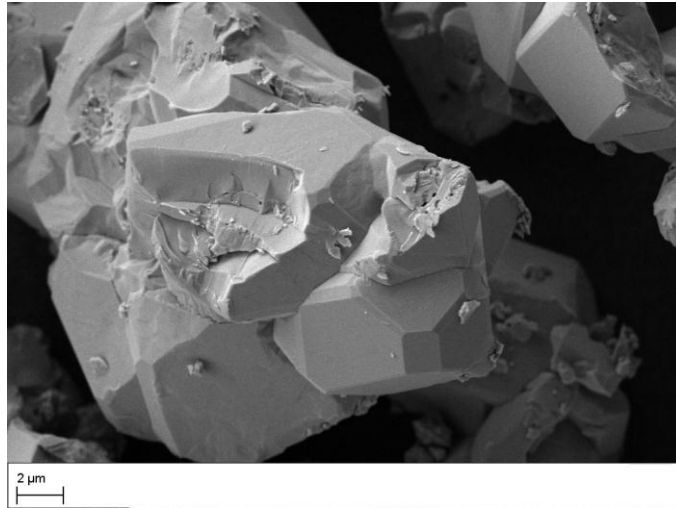


Figure 3.11 SEM image of Zn₃N₂ synthesised by quenching method

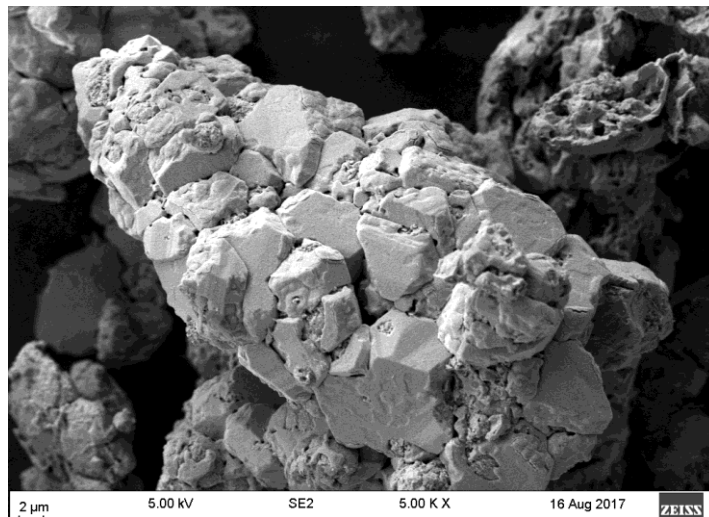


Figure 3. 12 SEM image for Zn₃N₂ synthesized by liquid nitrogen method

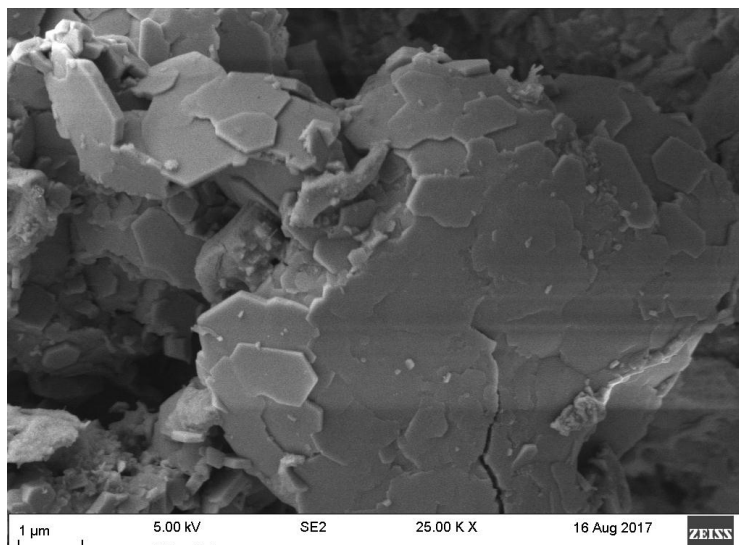


Figure 3. 13 SEM image for Zn₃N₂ synthesized by liquid nitrogen method

Zn₃N₂ samples synthesized by liquid nitrogen cooling had a broadly similar morphology, confirming the formation of crystallised Zn₃N₂ including a matrix of less regular fused particles (Figure 3. 13). The contrast in these structures can be attributed to the different cooling mechanism; more uniform by oil-bath quenching and starting from the surface in liquid N₂ cooling. Considering the crystal structure of the possible materials, the hexagonal structure might be associated with segregating ZnO (as mentioned before, always present even in residual concentrations) or to Zn, with a principle of crystallisation along the [0001] direction, abruptly interrupted by the rapid cooling. The result would be evidence of the small amount of impurities observed by XRD analysis. However, no elemental composition or EDX mapping was possible on these particular sections of the sample, so the exact nature of the different morphological features is still unclear.

Finally, a comparison of the morphology observed for the samples was made with the few controversial reports in literature for Zn₃N₂. In Figure 3. 14, the morphology of Zn₃N₂ powder synthesised at 600 °C for only 120 minutes can be observed. According to the authors, the spherical shape of the nitride (Figure 3. 14 (a)) is attributed to the interaction of a droplet of boiling Zn with NH₃. On the other hand, no explanation is provided for the formation of the hexagonal structures (image on the right), similar to the ones observe herein by liquid N₂ cooling. Previously reported experiments (leading to formation of Zn₃N₂ after at least 10 hours) could not be reproduced in the work herein detailed. However, the formation of hollow spheres has also been reported elsewhere.^[87] The theory of the reaction with vapour or droplets of Zn above its melting point could be considered valid, given also our own experimental evidence. In the previously reported work, Zn₃N₂ films (characterised by PXD analysis) formed on the quartz tube wall using a vertical configuration setup.⁸⁷

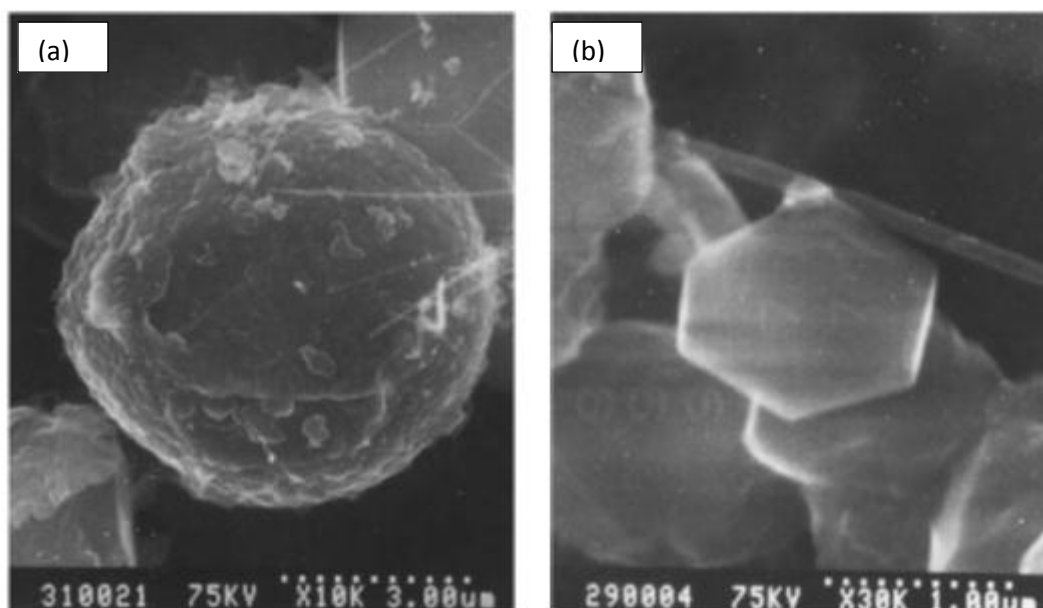


Figure 3. 14: Zn_3N_2 powder synthesised at 600°C for 120 minutes^[89]

EDX performed on Zn_3N_2 powder suggested a correlation between synthesis method, morphology of the final products and the elemental composition and distribution. Several points and areas were selected for the elemental analysis of the sample, choosing different sections in shown the previously collected SEM images. The EDX analysis of the polygonal faceted crystallites (Table 3. 5), evidenced the presence of nitrogen and a very low concentration of oxygen. However, the unshaped and irregular material forming at the margins of the crystallites showed the reverse trend of elemental concentration, with high level of oxygen, as witnessed by the results in Table 3. 6.

Table 3. 5: EDX analysis for the polygonal regular structure observed in Zn_3N_2 morphological analysis

Atoms Position	Average/ at%	σ
Zn	57.42	9.44
N	35.88	9.18
O	6.70	2.41

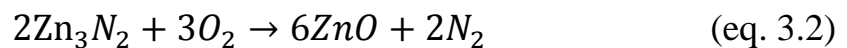
Table 3. 6: EDX analysis for the irregular material observed in Zn₃N₂ morphological analysis

Atoms	Position	Average/ at%	σ
Zn		42.56	9.63
N		24.93	10.07
O		32.50	12.42

The experimental elemental composition can be compared with the theoretical values of the material, which in case of Zn₃N₂ are 40% of N and 60% of Zn. The experimental results reported in Table 3. 5 match reasonably well with the theoretical values, with relative percentage of 57.4% for Zn and 35.9% for N when the presence of oxygen is excluded. Comparing the relative concentration of Zn and N in the irregular material observed at the edges of the crystallites, the amount of the two elements remains in a similar ratio (63% for Zn, 37% for N). However, the irregular material contains a much larger amount of oxygen (32.5% versus the original 6.70%) that cannot be neglected. These values potentially indicate the presence of ZnO in addition to Zn₃N₂, (while excluding any unreported oxynitride materials). Nevertheless, it was difficult to estimate the relative amount of ZnO in the sample, probably due to the presence of background oxygen (for example, from the carbon tab used for the sample preparation) and the low accuracy of the technique in discrimination between light elements such as N and O. For example, considering only the amount of nitrogen, the correspondent amount of Zn for the complete formation of Zn₃N₂ should be approximately 37.5%, which would leave only 5% of Zn available for the formation of ZnO.

The higher amount of oxygen could be also arising from reaction of the sample with atmospheric moisture adsorbed during the sample preparation for SEM

analysis. This could lead to formation of a nanometric oxide layer, not detectable by PXD (equation 3.2).^[90]



The superficial layer of ZnO could then increase the total amount of oxygen detected and would be expected to react at a higher rate with smaller irregular particles than the larger crystallites. Other techniques should be used to clarify the exact composition of the samples and surfaces observed, such as X-ray Photoelectron Spectroscopy (XPS), which would provide a precise measure of the composition of the surface to a depth of 10 nm and is particularly accurate for light element detection.

3.3 Band gap measurement

The optical band gap for samples was calculated using optical diffuse reflectance spectroscopy (DRS) measured via UV-Vis absorption spectroscopy. In one of the few works reporting the synthesis of polycrystalline Zn_3N_2 and a determination of its optical properties, Kuriyama *et al.* observed a direct band gap of 3.2 eV.⁶⁰ However, depending on the nature of the material, very different band gap values have been reported, in particular for Zn_3N_2 thin films much lower band gap values were reported, with a minimum of 0.8 eV.⁵⁴

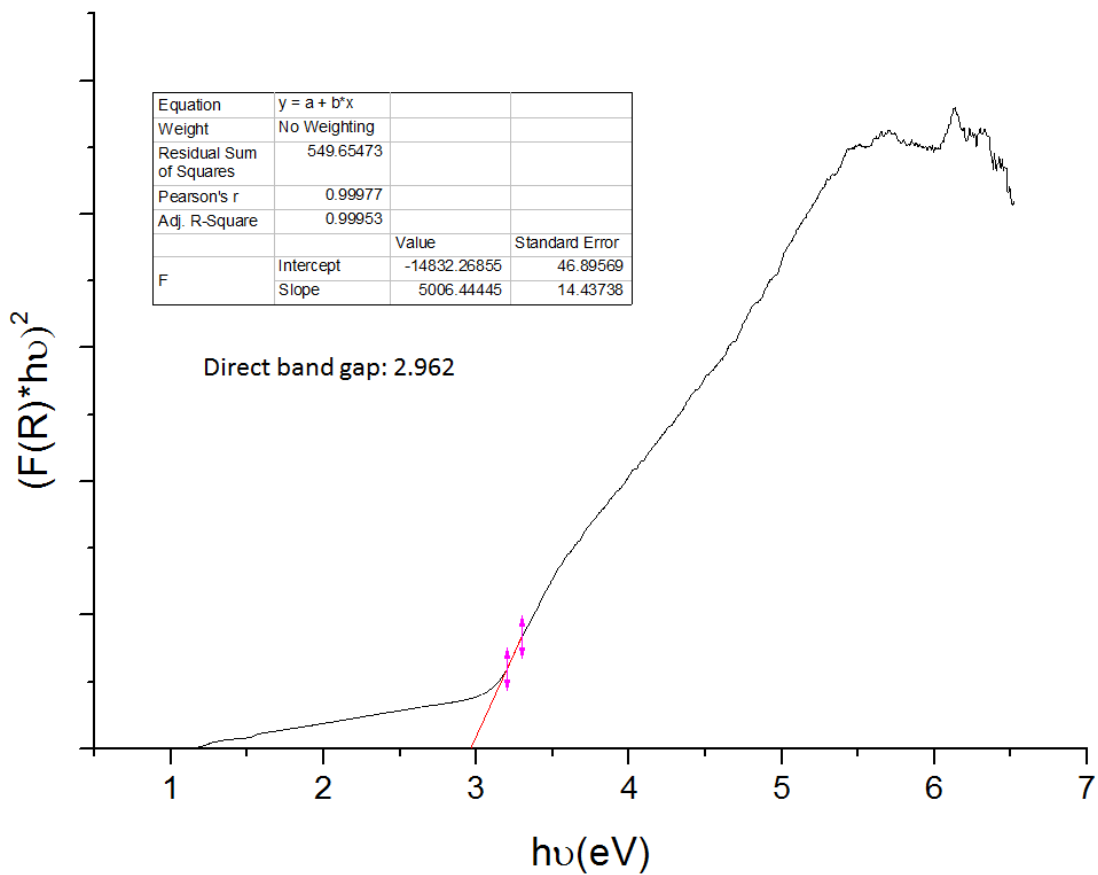


Figure 3. 15: Kubelka-Munk function transformation of UV-vis diffuse reflectance vs energy for Zn_3N_2 sample 12.

Figure 3. 15 shows the transformed UV-vis diffuse reflectance spectrum for Zn_3N_2 powder synthesised using the oil-bath quenching method (sample 12). This was the purest Zn_3N_2 material obtained from the experiments. The direct band gap is calculated using a transformation of the Kubelka-Munk function, which is a mathematical expression function of the diffuse reflectance and represents the ratio between the absorption and the scattering related to a uniform surface. The calculations gave a value of 2.96 eV, which is not far from the value reported by Kuriyama *et al.*

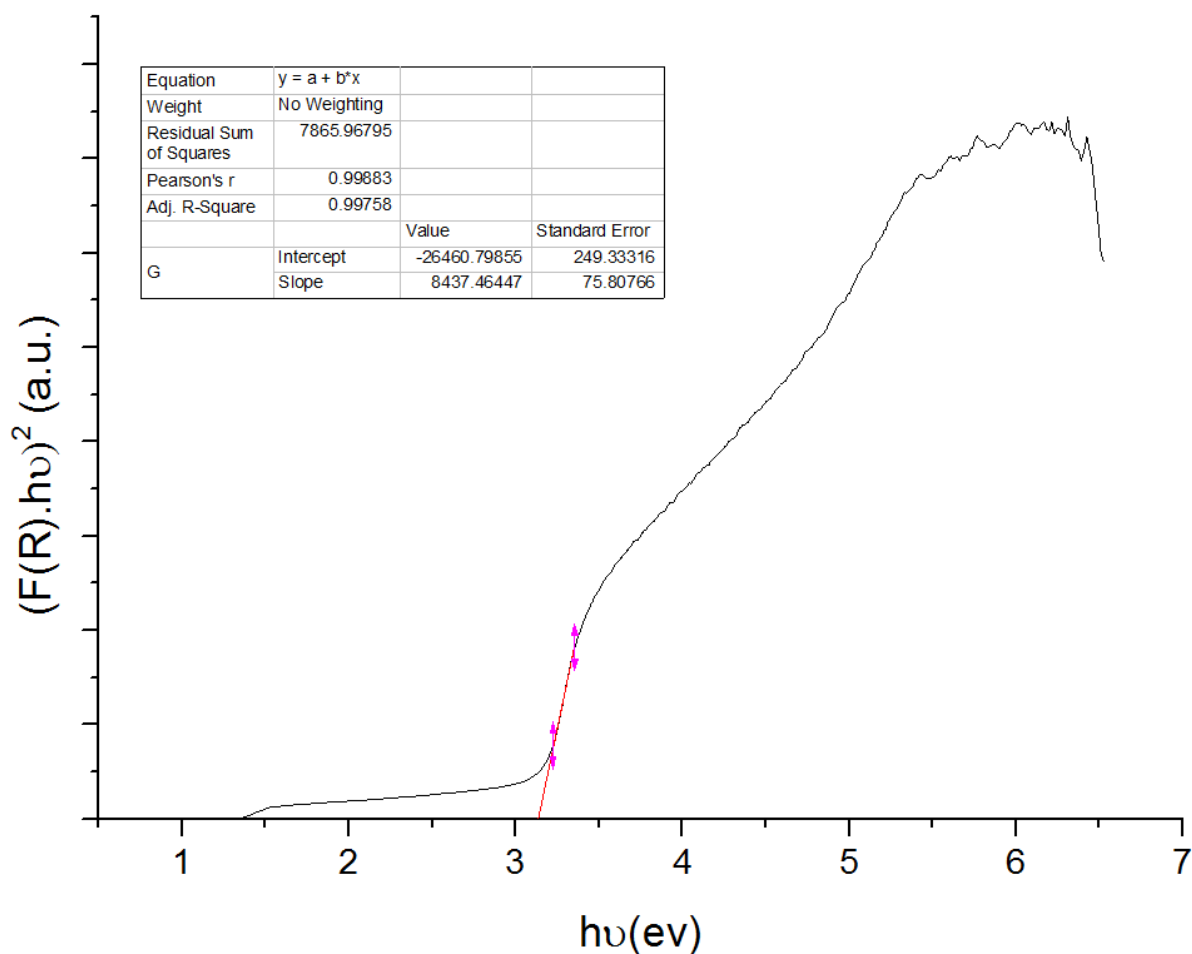


Figure 3. 16: Kubelka-Munk function transformation of UV-vis diffuse reflectance vs energy for Zn_3N_2 sample 11.

However, in Figure 3. 16 the direct band gap of Zn_3N_2 synthesised using an Ar flow (sample 11) at room temperature during the conventional cooling phase, was estimated to be 3.13 eV. This sample appeared to confirm a higher amount of ZnO impurity compared with sample 12 and were any oxygen substituted in the Zn_3N_2 structure, it would directly influence the band gap. It is evident from these results that the presence of ZnO affects, besides the purity of the material, also the overall optical properties. Analysing the shape of the Kubelka-Munk functions, the presence of a double band gap can be ruled out (the curve should have presented a double slope). The conventional by cooled sample 11, the band gap is closer to ZnO (3.37 eV).

3.4 Zinc nitride Rietveld refinement

Rietveld refinement was performed against powder XRD data for the purest Zn₃N₂ sample 12 (sample 12 synthesised by quenching in the oil bath) to compare its crystal structure with the models reported in the literature. The refinement was performed using the structure of Zn₃N₂ reported in the ICSD database (FIZ Karlsruhe), based on the work of Partin *et al.* [51] as a starting model. The calculations were performed using the EXPUGUI-GSAS software. According to the reference data, the crystal structure of Zn₃N₂ is cubic (space group I a-3) with a lattice parameter a=9.7691 Å.

The results of the refinement, reported in Figure 3.17 and Table 3. 7, show that the synthesised Zn₃N₂ presents slightly larger lattice parameters and a higher cell volume compared with the reference structure. However, the difference is minimal, with the result being in substantial agreement with the results of Partin *et al.* .

Table 3. 7: Crystallographic information obtained from Rietveld refinement of Zn₃N₂

Crystal system	I-centered cubic
Space group	I a-3
Lattice parameters	a= b= c = 9.7830(12) Å
Lattice angle	α= β= γ= 90°
Z	16
Volume	936.314 (20) Å ³
Unit cell formula weight	3586.464
Density	6.361 g/cm ³
wRp	0.1606
Rp	0.1242
χ²	3.743

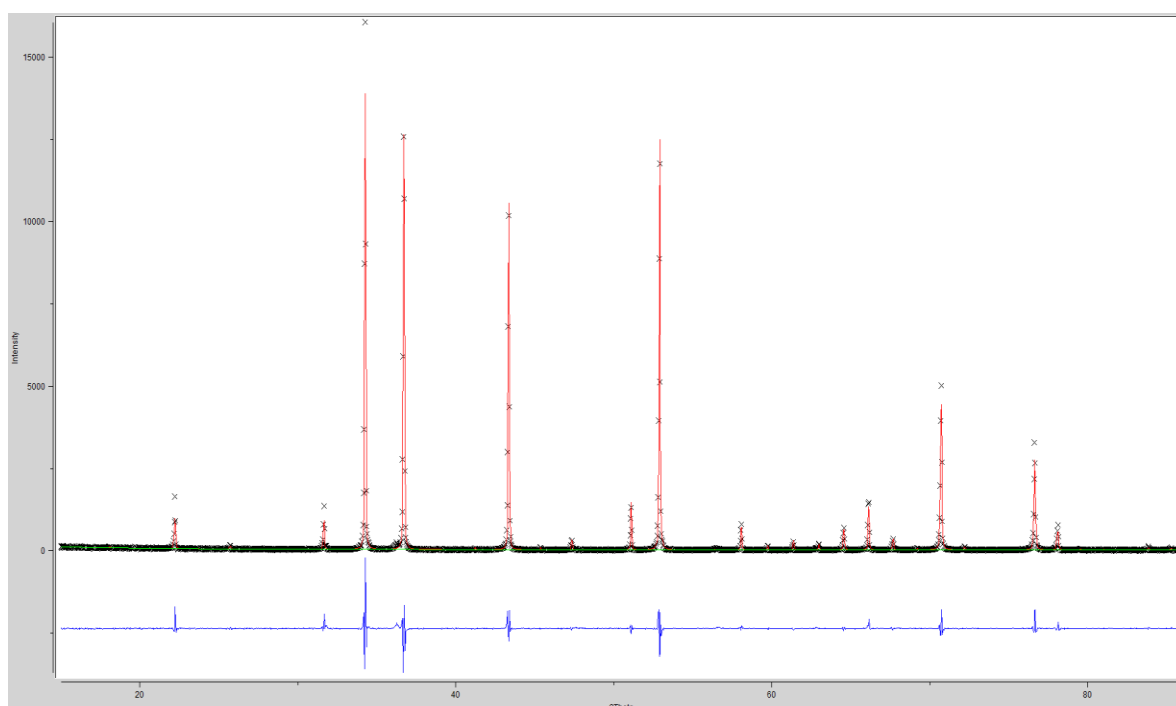


Figure 3.17: Rietveld refinement for sample (Zn_3N_2 synthesised by quenching method). Red line for calculated data, black crosses for experimental observations, green line for background curve, blue line for the difference between calculated and observed patterns.

Atomic parameters are shown in Figure 3.17 and bond lengths in Table 3.9.

Table 3. 8: Refined atomic parameters of the phase in sample 12 Zn_3N_2

Atomic parameters						
Atom type	Wyckoff Site	Fractional Coordinates			Uiso / \AA^3	Occupancy
		x	y	z		
Zn(1)	48e	0.39661(3)	0.15184(3)	0.37559 0(4)	0.02017 (7)	1.0
N(1)	8b	0.25	0.25	0.25	0.00161 (7)	1.0
N(2)	24d	0.97925(1)	0	0.25	0.01143 (4)	1.0

Table 3. 9 Refined interatomic distances sample 12 Zn₃N₂

Zn(1)-N(1)/ Å	2.1197(28)
Zn(1)-N(2)/ Å	2.277(7)
Zn(1)-N(2)/ Å	1.994(10)
Zn(1)-N(2)/ Å	2.086(7)
Zn(1)-Zn(1)	2.752(4)
Zn(1)-Zn(1)	3.1593(10)
Zn(1)-Zn(1)	2.7887(28)
Zn(1)-Zn(1)	2.718(4)

The cell parameter is larger than previously reported.^[91] Bond lengths are similar to previous research with some small differences in the bond lengths. This might due to the different oxygen content in the final products.

Despite the good quality of the pattern, it was not possible improve the quality of the refinement further. A certain number of discrepancies can be observed between the calculated and experimental patterns (Figure 3.17), especially considering the relative intensity of the peaks. These suggest that the structure, might involve subtle modifications such as partial substitution of oxygen in some nitrogen positions. More powerful techniques, such as neutron diffraction, would provide stronger evidence for this given the superior contrast in N and O scattering lengths compared to PXD.

Chapter 4: Zinc nitride fluoride

4.1 Zinc nitride fluoride synthesis

The successful improvements to the synthesis of Zn_3N_2 were detailed in the previous chapter. Synthesis of high-purity nitride is complicated by the formation of ZnO impurities, which are difficult to prevent. The market cost of the relatively pure material is an indicator of the issues related to the synthetic procedure.

For this project, the interest in high-purity Zn_3N_2 was motivated by its use as precursor for the synthesis of Zn_2NF , the principal material of our investigation. According to previous research, Zn_2NF has two crystalline forms, a low-temperature and a high-temperature structure. The low-temperature phase is orthorhombic, while the high-temperature phase is tetragonal. However, the phase transition temperature between the two forms is still controversial and the thermal analysis was performed in a static vacuum in a quartz tube.^[46]

For the synthesis of Zn_2NF , a 1:1 stoichiometric mixture of Zn_3N_2 (produced in house) and ZnF_2 (Alfa Aesar, 99%) were ground together to obtain a homogeneous powder (approximately mass as 0.223g: 0.103g). The powder mixture was placed into an alumina crucible, in turn inserted into a sealed stainless steel reactor. The reactor was placed in a small vertical furnace, connecting the reactor flanges to the vacuum system. The reaction was performed under vacuum in a quartz or stainless steel tube to prevent the formation of impurities due to oxidative side reactions. In all the reactions, the system was brought to temperature using a heating rate of 5 °C/min. The

optimal synthesis conditions were investigated, together with a detailed characterisation of the Zn₂NF product.

In principle, the synthesis of the low-temperature phase was targeted. Several attempts were tried, following the work of Lingampalli et al. and modifying the synthesis conditions, which are reported in Table 4. 1.

Table 4.1: Synthesis conditions for the preparation of the low temperature phase of Zn₂NF

Reaction	Temperature/°C	Duration time/h	Pressure/ mbar
1	350	1	$2 \cdot 10^{-2}$
2	350	3	$2 \cdot 10^{-5}$
3	450	3	$1 \cdot 10^{-5}$

As can be seen in the PXD patterns in Figure 4. 1, the products of the low-temperature phase reactions are mainly unreacted Zn_3N_2 and ZnF_2 plus ZnO impurities. Other weaker reflections in the patterns might be associated with other nitride-fluorides, such as $Zn_9N_4F_6$ and $Zn_7N_4F_2$. The presence of Zn_2NF cannot be confirmed even from an analysis of these low-intensity reflections. Zn_3N_2 and ZnF_2 do not appear to react at these temperatures. The amount of ZnO significantly increased at 450 °C. It is difficult to explain the formation of the ZnO even under mild-vacuum conditions.

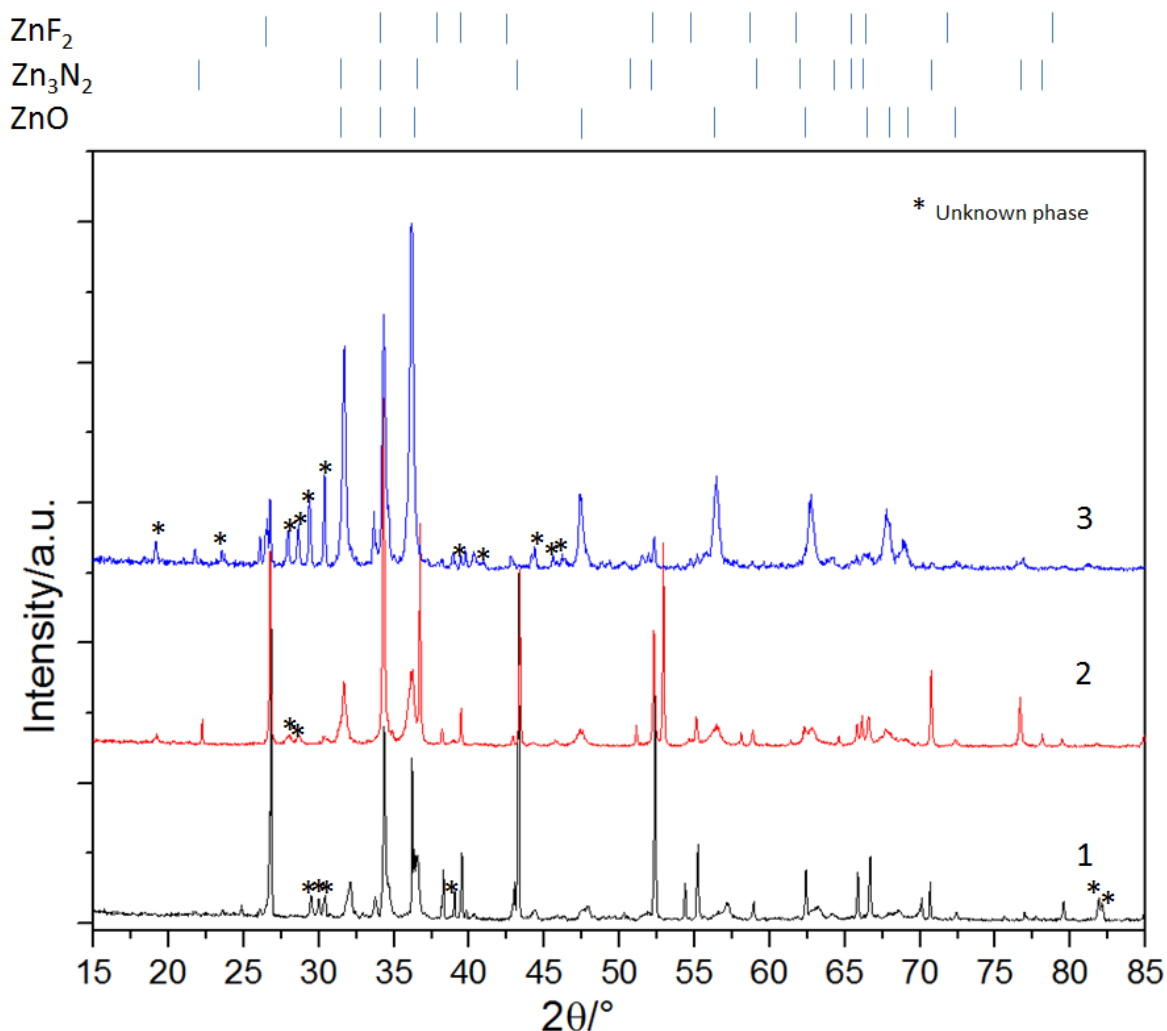


Figure 4. 1 PXD patterns of the products from low-temperature Zn_2NF reactions 1-3

In further attempts, the reactor, together with the precursor mixture, was degassed overnight and then sealed under an N₂ atmosphere in a glovebox, in order to minimise external oxygen and water. Moreover, since the conditions previously used (350 °C - 450 °C) were not sufficient for the reaction of the starting materials, the synthesis of Zn₃N₂ was performed at higher temperatures. The improved synthesis conditions are detailed in Table 4.2.

Table 4. 2: High-temperature Zn₂NF synthesis conditions

Sample	Temperature/°C	Duration time/h	Atmosphere
4	350	1	Ar
	500	2	
5	500	3	Vacuum;1·10 ⁻⁵ mbar
6	500	2	Vacuum;1·10 ⁻⁵ mbar

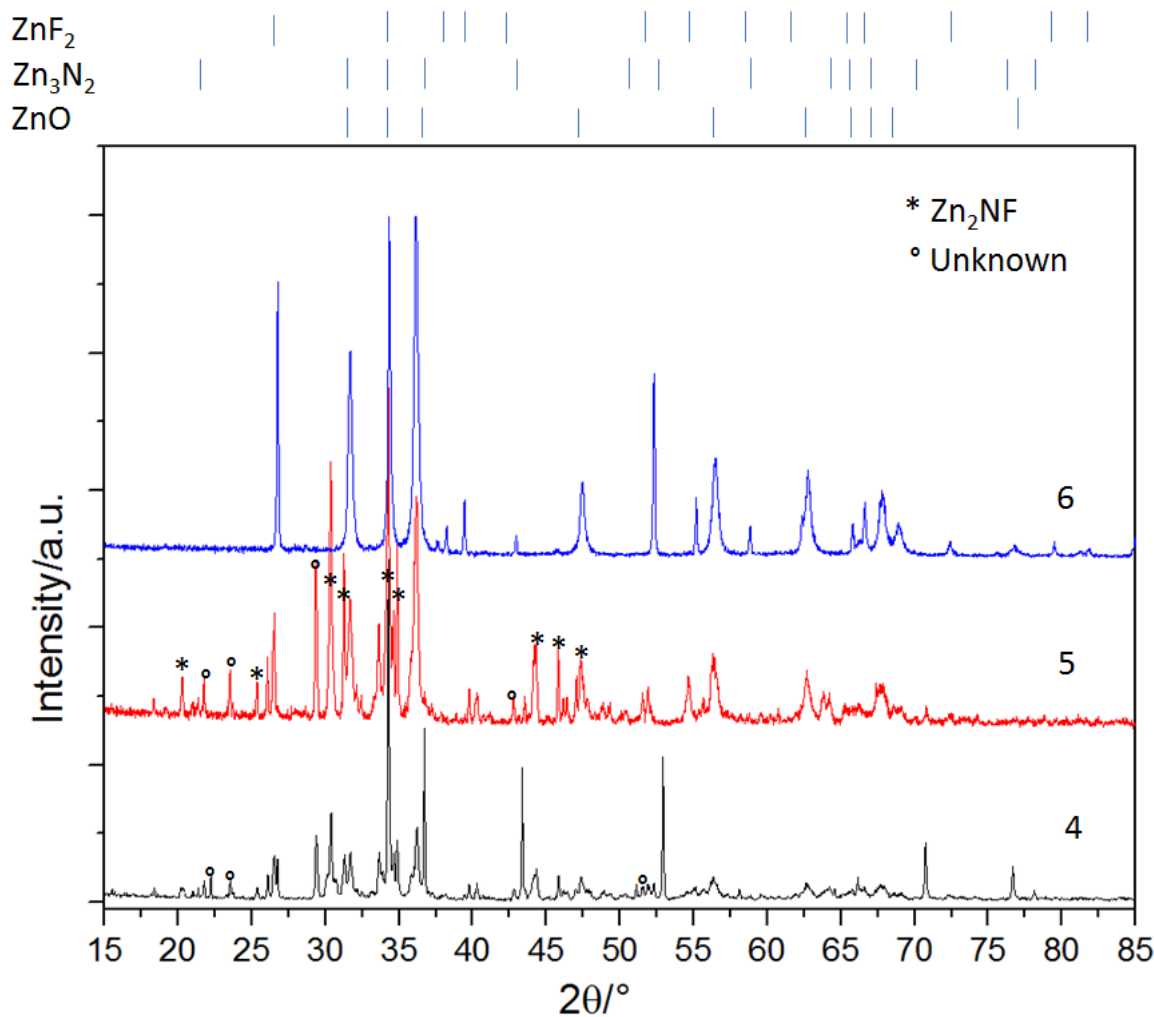


Figure 4. 2 PXD patterns of the product from the high-temperature Zn_2NF reactions 4-6

The effect of the increase of reaction temperature can be seen from PXD patterns (Figure 4. 2). Sample 4 was prepared using two heating steps, as reported for the synthesis of Zn_2NF by Lingampalli et al.⁴⁶ Although this time the precursor mixture reacted, the main phases observed were Zn_3N_2 and ZnO . Additionally, when the reaction was performed in a single step bringing the temperature directly to 500 °C (sample 5), the tetragonal high-temperature structure of Zn_2NF was observed, together with other forms of nitride-fluoride ($\text{Zn}_9\text{N}_4\text{F}_6$) and ZnO impurities.

Despite the formation of tetragonal Zn_2NF , the product is not single phase and not highly crystalline. The treatment time used might have not been sufficient

to achieve complete crystallisation. A further reaction was performed in the an attempt to improve the quality of Zn_2NF and remove the impurities (at least the secondary nitride-fluoride phase). The product of reaction 5 was used for a second reaction under the same temperature conditions for an additional 2 hours. Unfortunately, the resulting product (sample 6) showed an increased amount of ZnO , (as the predominant phase) with the additional presence of ZnF_2 . Despite all the precautions adopted to prevent the contact with oxygen or water, an additional thermal treatment apparently caused the decomposition and favoured the formation of ZnO .

STA analysis was performed to clarify the processes behind this set of reactions, to determine the onset temperature for the formation of Zn_2NF and to evaluate its thermal stability. Furthermore, since the STA instrument is enclosed under a protected atmosphere (Ar-fed glovebox) and Ar is used as carrier gas during the thermal analysis. It would be virtually guaranteed that air would be excluded from the reaction. In this way, it was possible to follow the reaction in real time through observation of the sample mass variation (TG) and the temperature difference with an inert reference (DTA).

A mixture of Zn_3N_2 and ZnF_2 powders was placed into an alumina pan, used as standard sample holder for the STA. The suggested maximum material loading for the STA measurement is 30 mg, so this was the mass of the reactants used for this reaction. A heating rate of 5 °C/min was employed for all reactions. The other synthesis conditions are reported in Table 4.3.

Table 4. 3: Zn₂NF reaction condition for syntheses using the STA apparatus

Sample	Reaction temperature/°C	Dwell time/h
7	350	1
8	450	6
9	350	1
	500	2
10	500	6
11	600	3
12	650	3
13	700	no dwell
14	700	1

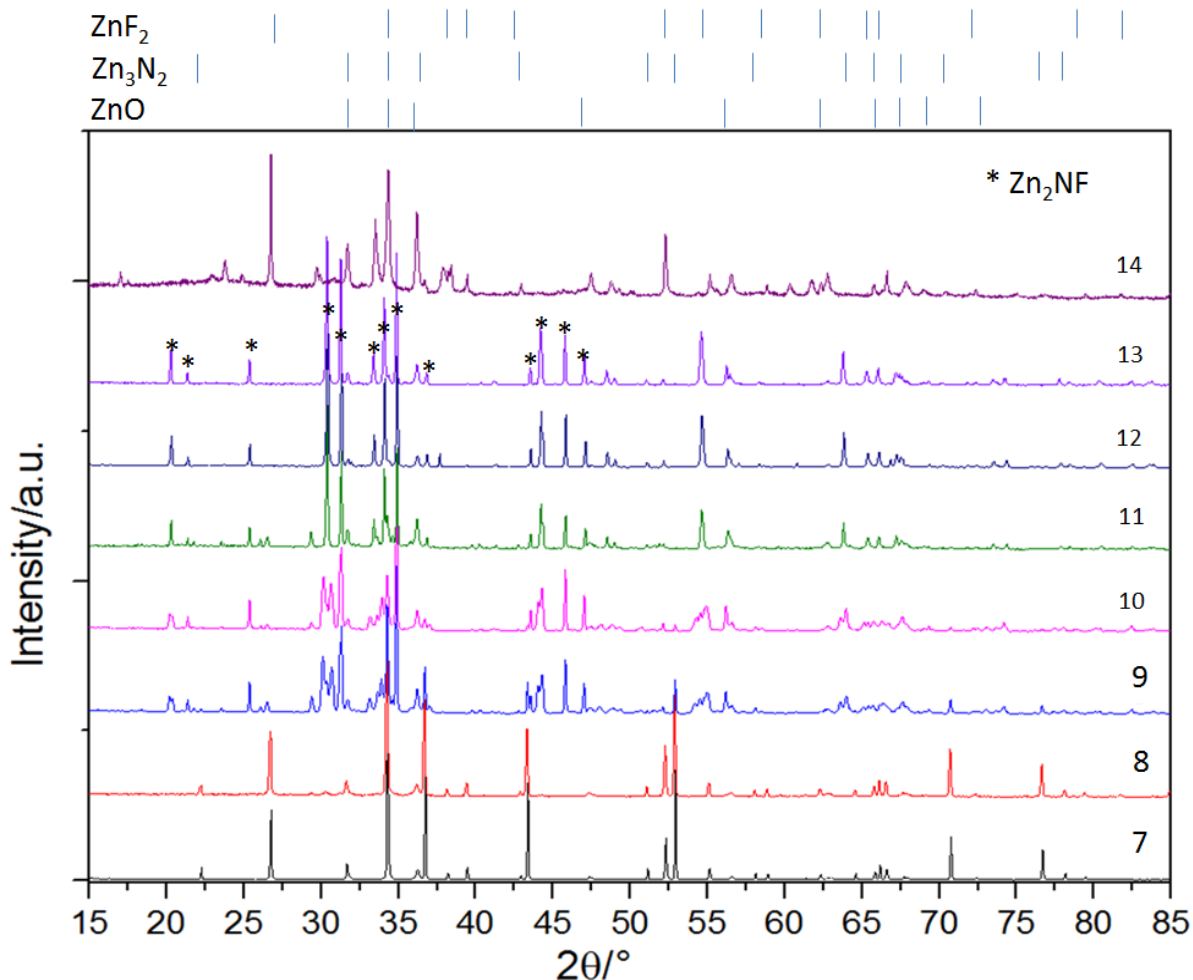


Figure 4. 3 Comparison between XRD patterns of the synthesis reactions of Zn₂NF in STA apparatus

Figure 4. 3 shows the PXD patterns from the STA reaction products under different experimental conditions. The reactions at 350 °C and 450 °C (samples 7 and 8) did not produce Zn₂NF, with unreacted Zn₃N₂ as the main phase. Zn₂NF synthesis occurs at temperatures between 500-700 °C (samples 9 to 13).

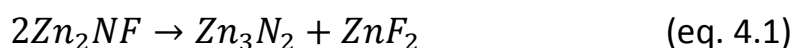
These results confirm our previous findings. Furthermore, the two-step reaction (9) and the single-step one (10) resulted in the same final products, according to their XRD patterns. This result is not in agreement with the results of Lingampalli et al.; where the final product appears to depending only on the final temperature. In fact, there are more impurities resulting from the double-step reaction (9) than the single-step reaction (10). For this reason, single-step reactions were considered to give a higher purity crystalline product. Another

observation is the ZnO impurity was present after reactions (9) and (10) while it decreased as the temperature was increased in reactions (11) to (13). The purity control of the atmosphere in the STA apparatus ensured the dramatic reduction of external contaminants (oxygen, water), which can be considered as the real cause of the formation of ZnO during the synthesis of Zn_3N_2 .

With increasing temperature, the synthesis and crystallisation processes tend to go to completion. At 700 °C, tetragonal Zn_2NF peaks are well-defined and the previously observed additional peaks $Zn_9N_4F_6$, $Zn_7N_4F_2$ and some unknown phases are present.

As an example, the pattern related to the synthesis at 500 °C (sample 10) presented a peak around 30.4°, which cannot be associated with any known reflections of Zn nitride fluoride structures and it is very close to the (1 1 1) peak of tetragonal Zn_2NF . The higher product purity is manifested by the progressive disappearance of the peak belonging to the unknown intermediate phase from 600 °C (sample 11) and its total absence at higher temperature (samples 12 and 13).

Tetragonal Zn_2NF was formed as a product for all the reactions between 500-650 °C, regardless of the duration of thermal treatment. However, when the reaction temperature was held at 700 °C for 1 hour (sample 14), the resulting product was comprised mainly of ZnO with residual ZnF_2 . At this temperature decomposition of Zn_3N_2 appears to occur. When the temperature reaches 650 °C, the final product has the tetragonal crystal structure of the high temperature phase of Zn_2NF . However, any further heating dwell leads to decomposition of the material, and the subsequent nitride, leaving ZnF_2 unmodified, due to its higher thermal stability. The decomposition mechanism might be summarised as follows:



where O in the last equation represents not only the eventual presence of oxygen in the STA apparatus (the purity standard for a protected atmosphere in a glovebox requires less than 1 ppm for both O₂ and H₂O), but also pre-existing impurities (<1% ZnO present in Zn₃N₂).

The synthesis reaction of Zn₂NF appears similar to a sort of equilibrium in which the material is dissociated into the original precursor when the temperature destabilise one of this two. As will be described in the analysis of the morphology of these materials, the sample produced by reaction 7 (ramp to 700 °C without further dwelling) presented a totally different morphology than the sample obtained by reaction 6 (600 °C for 3 hrs), despite processing the same crystalline structure.

These findings are also raise questions about the true nature of Zn₂NF, which can be seen as an equilibrium mixture of the two original materials in intimate contact, producing a totally different structure. Further investigations clarifying the composition of the material (TEM analysis and theoretical calculations such as DFT) are beyond the scope of this dissertation.

The orthorhombic low-temperature phase of Zn₂NF was not observed at any of the intermediate conditions between the non-reaction of the original precursors and the formation of tetragonal Zn₂NF. Orthorhombic Zn₂NF was expected at around 350-450 °C, but none of the temperatures or treatment times (up to 6 hrs) were successful in synthesising this structure. This result is in contrast with the findings of Lingampalli et al.,^[46] which claimed low-

temperature Zn_2NF could synthesized from the reaction between Zn_3N_2 and ZnF_2 at 350 °C for just 1 hour under vacuum.

Tetragonal Zn_2NF appears as a yellow powder (Figure 4. 4). The compound is stable in air, as assessed by the total absence of chromatic modification and unchanged crystalline structure after several weeks of being exposed to the atmosphere. This colour is similar to that reported previously for tetragonal Zn_2NF .⁴⁶

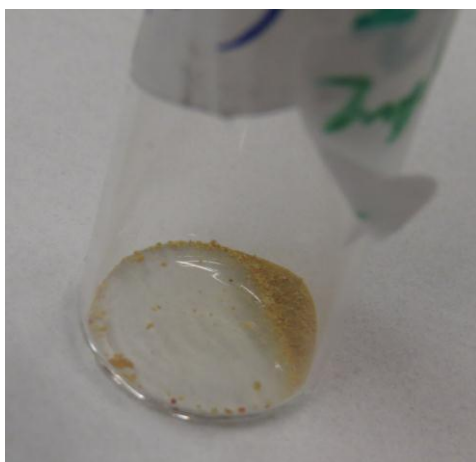


Figure 4. 4 Tetragonal Zn_2NF powder

4.2 Zn_2NF SEM and EDX

Pure Zn_2NF synthesised in the STA was further characterised by SEM and EDX.

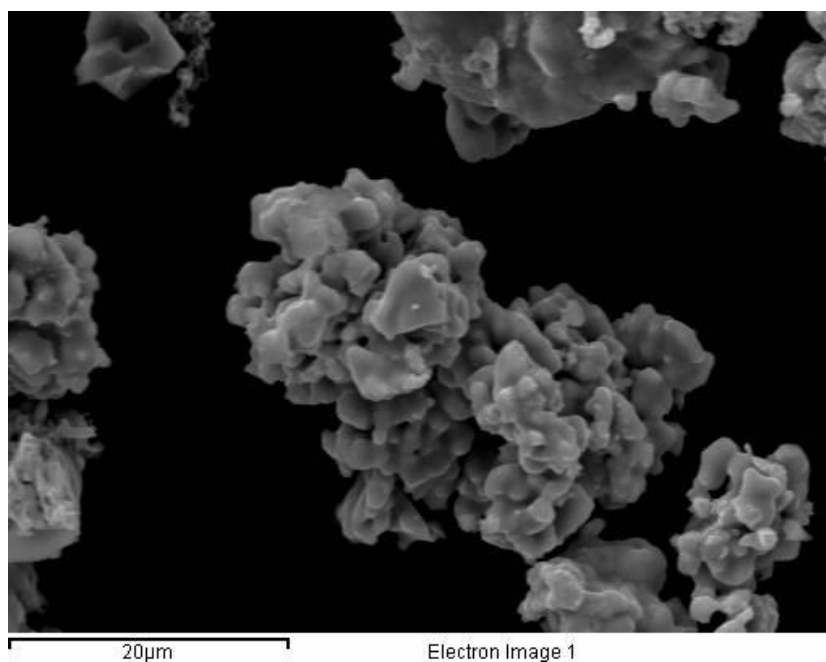


Figure 4. 5 Micrograph of Zn_2NF synthesised at 650 °C for 3 hours (sample 12)

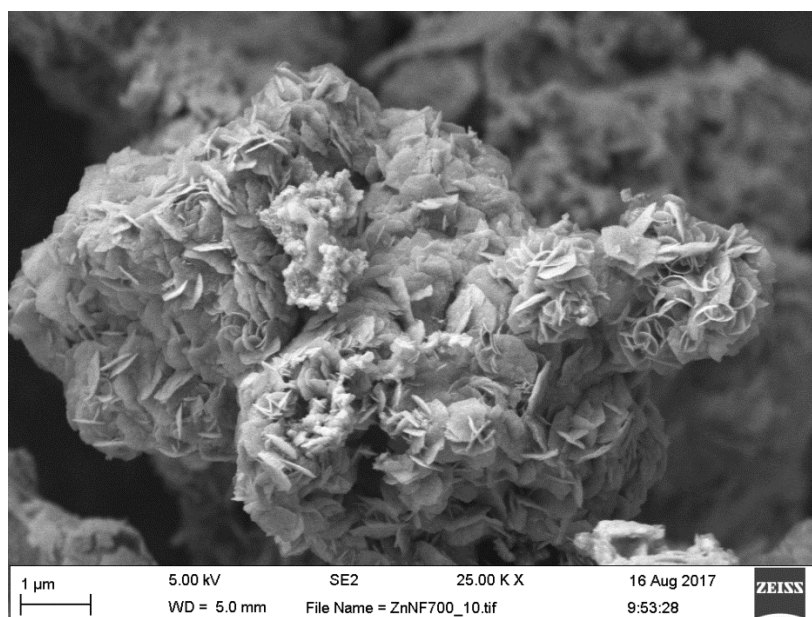


Figure 4. 6 SEM image of Zn_2NF synthesised at 700 °C (sample 13)

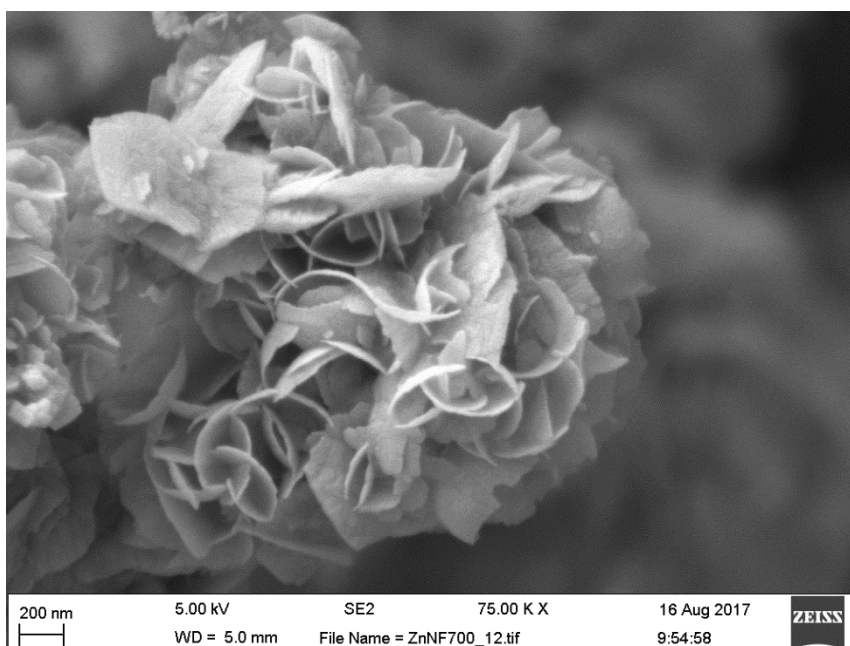


Figure 4. 7 Higher magnification SEM image of Zn₂NF (sample 13), illustrating typical petal structure

Zn₂NF synthesised at 650 °C has an irregular morphology, mainly composed of block-like micrometric agglomerates (2.5 µm average size). Individual component particles vary in size from 5.5 to 1.9 µm and have a faceted appearance. After heating to 700 °C (sample 13) the morphology was quite different, showing the formation of thin petal-like particles which cluster into complex structures. The morphology at 650 °C (sample 12) is reminiscent of the observed in pure Zn₃N₂, albeit with a smoothing of the edges of the crystallites.

The sample produced at 700 °C (sample 13) shows a more hierarchical morphology. The petal-like structure extends across the entire surface of the sample. The flower-like structure results from the disordered arrangement of the petals, intersecting and crossing each other rather than forming an ordered layered structure. The thickness of the petals was measured using the SEM images with the ImageJ software package. The petal thickness ranges between 7 -18 nm, with an average size of 12 nm.

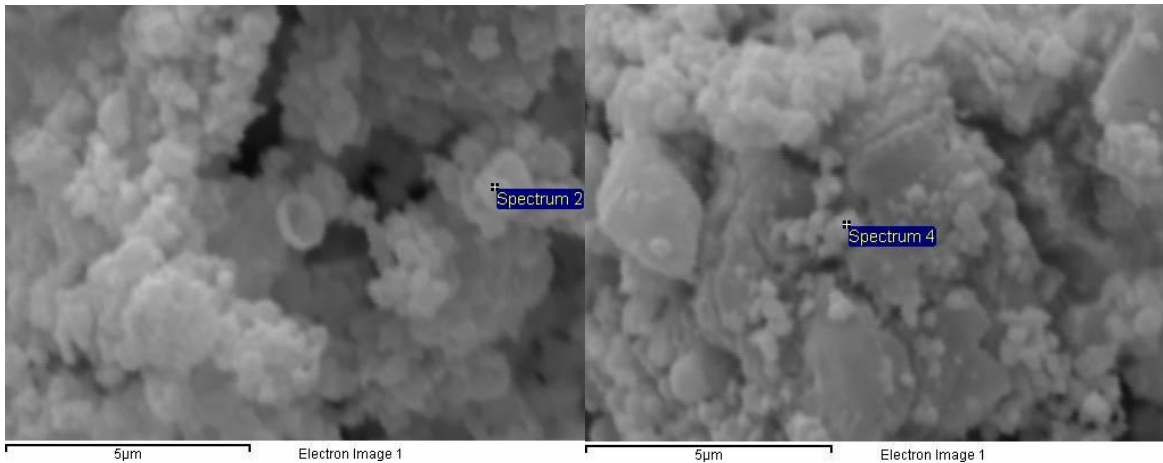


Figure 4. 8 SEM image of sample 11 synthesised at 500 °C

Figure 4. 8 shows the morphology of Zn_2NF powder synthesised at 500 °C. In this case, the morphology is more similar to that observed at 650 °C, with evident presence of predominant large crystallites surrounded by smaller irregular particles. Since at 500 °C the formation of the nitride fluoride is not complete, the two different types of particles represent a mixture of the two reactant phases Zn_3N_2 and ZnF_2 respectively.

The elemental composition of Zn_2NF powders synthesised at different temperatures was determined by EDX analysis.

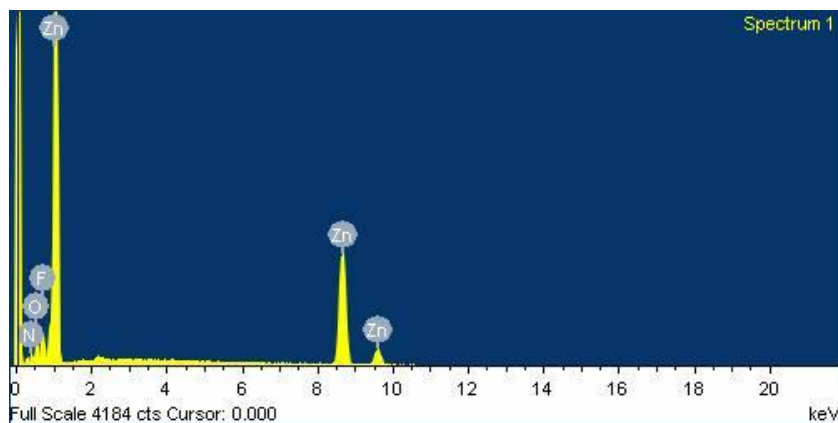


Figure 4. 9 EDX spectrum for the sample synthesised at 500 °C (sample 11)

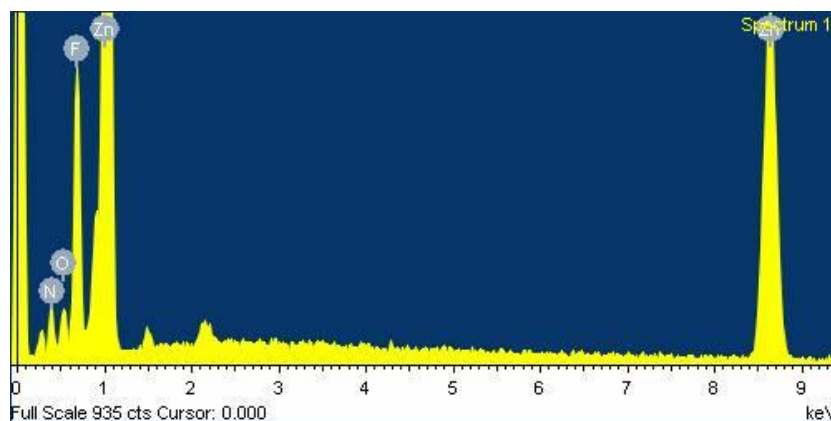


Figure 4. 10 EDX spectrum for sample synthesised at 650 °C (sample 12)

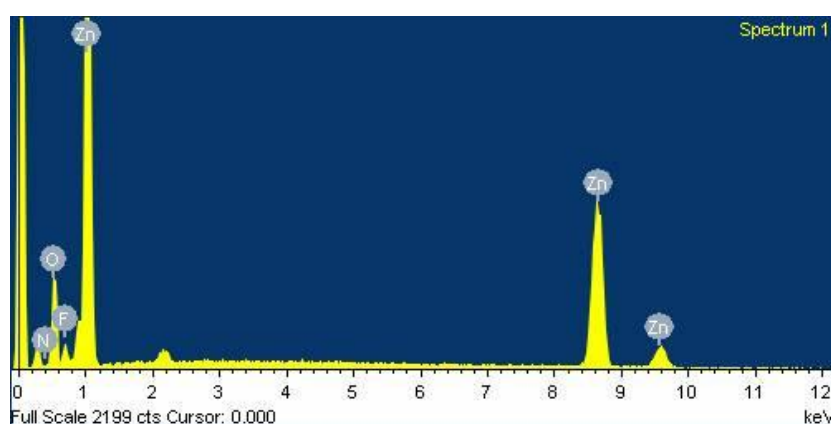


Figure 4. 11 EDX spectrum for the sample synthesised at 700 °C (sample 13)

EDX analysis confirmed the presence of the constituent atoms of Zn_2NF with, in addition, traces of oxygen. The elemental composition is sensitive to the reaction temperature, especially for nitrogen. In Table 4.4, the average concentration of the elements is listed as a function of the reaction temperature.

Table 4.4 : Relative atomic composition of Zn_2NF powder at different synthesis temperature

Atoms/% Temperature/°C	500	650	700
Zn	36.64 ± 6	34.13 ± 2	38.10 ± 7
N	17.69 ± 1	22.84 ± 1	5.01 ± 2

O	21.89 ± 4	6.96 ± 1	40.29 ± 5
F	23.79 ± 3	36.08 ± 2	16.60 ± 7

The zinc concentration is approximately constant for all the temperatures applied, at *ca.* 35%. At 500 °C, Zn₂NF shows higher than expected oxygen content, at a level comparable with nitrogen and fluorine atom concentrations. This is probably due to incomplete reaction, which led also to partial oxidation of Zn₃N₂, generating ZnO impurities. The fluorine content appears to be slightly higher than the nitrogen value, even though the stoichiometry ratio of the two is very close to 1:1. At 650 °C, the nitrogen and fluorine concentrations both increase at the expense of the oxygen content. On the other hand, at 700 °C the situation is the opposite, with a dramatic increase in the oxygen concentration and a decrease of the other two non-metals, especially nitrogen which is lowered drastically to *ca.* 5%. The reason for this loss in nitrogen might be attributed to the thermal decomposition of Zn₃N₂ reported to occur at 681 °C (whereas ZnF₂ melts at 872 °C).^[54] The thermal decomposition of Zn₃N₂ is competitive with the synthesis of Zn₂NF, since the reaction of the nitride with the fluoride occurs through partial decomposition of the former, according to our observations. This would also explain why the optimal synthesis temperature is just below the decomposition temperature, in which the decomposition-reaction with fluoride mechanism is predominant compared with the thermal decomposition of nitride. Since the concentration of oxygen and nitrogen in the EDX analysis are affected by the low sensitivity of the technique for the lighter elements and the presence of possible contamination from the surrounding environment, the atomic concentration of

fluorine has been assumed as a good parameter to evaluate the quality and the efficiency of Zn_2NF synthesis. Higher concentrations of F correspond to purer nitride-fluoride product.

4.3 Zn_2NF thermal analysis

According to the results reported in the previous sections, initial formation of Zn_2NF phase occurs at 500 °C, with an almost single phase material obtained at 650 °C. TG-DTA analysis can help in the identification of the onset temperature of the Zn_2NF formation through the study of the mass change and the appearance of specific thermal events. For this purpose, the reaction performed in the tube furnace was simulated by creating a temperature program analogous to the temperature profile (heating rate and thermal dwell) used for the Zn_3N_2 synthesis.

In addition, the Zn_2NF decomposition test has been set as 5 °C/min and 2 °C/min heating ramp from 25 °C to 1000 °C. Meanwhile, the mass spectrometer has been applied in the test with N_2 (28), N (14), F_2 (38), F (19) and O_2 (18) has been set as target species for measurement.

Figure 4. 12 and Figure 4. 13 show the TG curves for the reactions at 350 °C for 1 hour + 500 °C for 2 hours; 650 °C for 3 hours and 700 °C. It is evident that a reaction temperature of 500 °C does not lead to a significant mass loss; estimated at less than 2%. Conversely, setting higher reaction temperatures leads to much higher mass loss rates. The main weight loss onset occurred at 550°C. Further continuous increase of the temperature caused the mass loss process to accelerate.

As observed in Figure 4. 12 and Figure 4. 13, the mass loss rate is temperature dependent. The mass loss can be attributed to Zn_2NF decomposition since the nitride+ fluoride solid state reaction should occur at constant mass. The rate of decomposition increases with temperature and as Zn_3N_2 forms zinc + nitrogen gas. The EDX analysis of the resulting material would appear to support this.

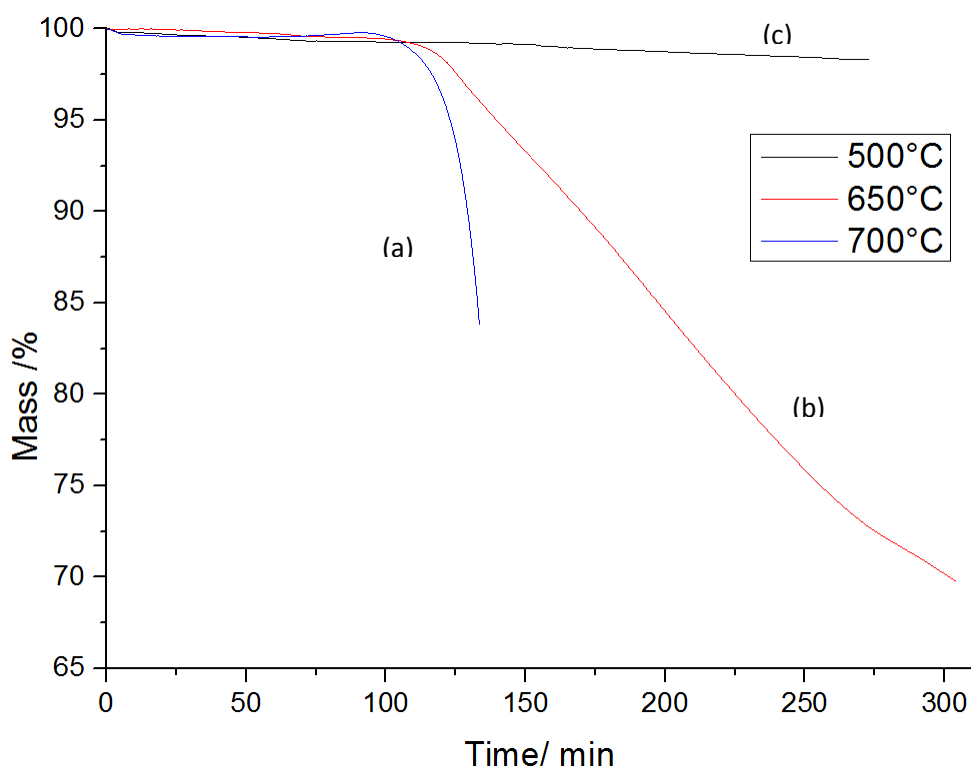


Figure 4. 12 Thermogravimetric analysis of the reactants as a function of time when heated to and held at (a) 700 °C (b) 650 °C (c) 350°C +500 °C respectively.

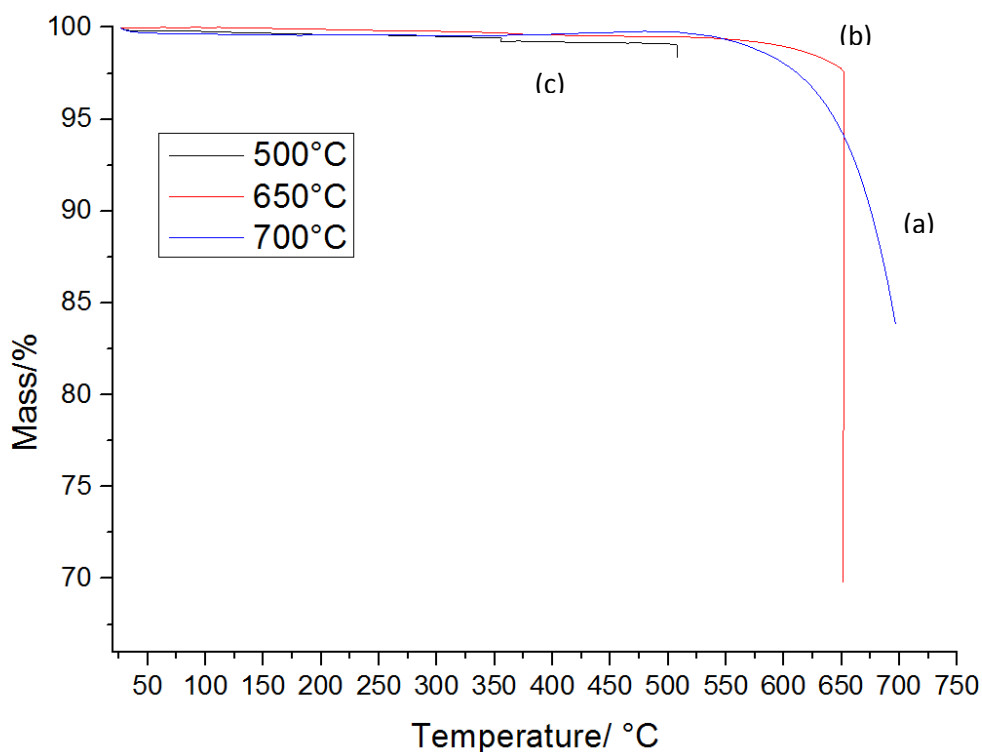


Figure 4. 13 Mass loss as a function of temperature for the experiments shown in Fig. 4.12

The thermal stability of Zn_2NF (sample 12) was tested via STA, using heating rate of $5^\circ C/min$ and $2^\circ C/min$ in the temperature range from $25^\circ C$ to $1000^\circ C$. The mass loss for the Zn_2NF powder shown in Figure 4. 14 indicates a significantly mass decrease in the range. $600- 800^\circ C$. The $5^\circ C/min$ scan gave higher decomposition rates than the $2^\circ C/min$ one. In Figure 4. 15, the DTA curves show three thermal events in both the analysis, which were marked with ①, ② and ③ respectively. The event onset temperatures were not corresponding in the two scan due to the different heating rate. The event 1 and 2 might be associated with the start and the end of the decomposition process, respectively. Event 3 is likely to be caused by the melting of ZnF_2 , which normally occurs at $872^\circ C$.

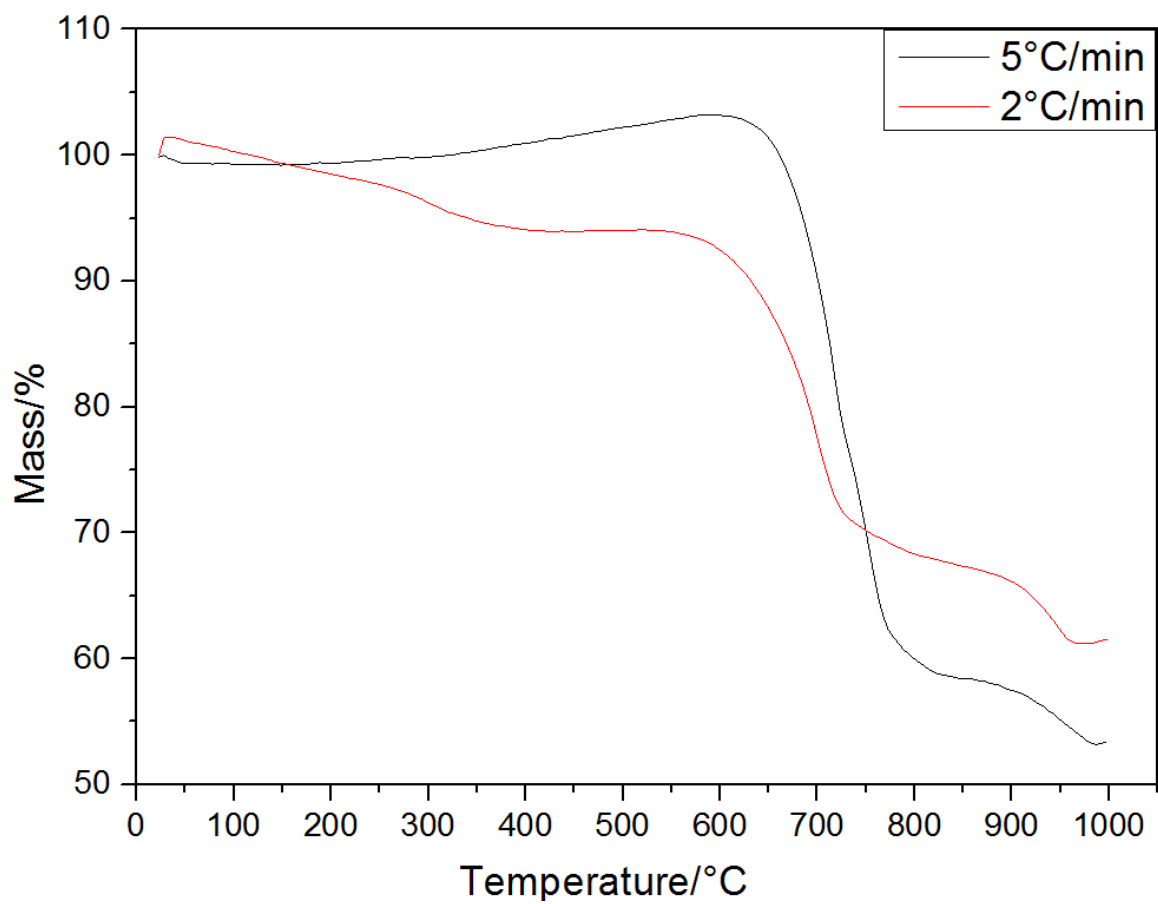


Figure 4. 14 Thermogravimetric of the sample 12 Zn₂NF decomposition test

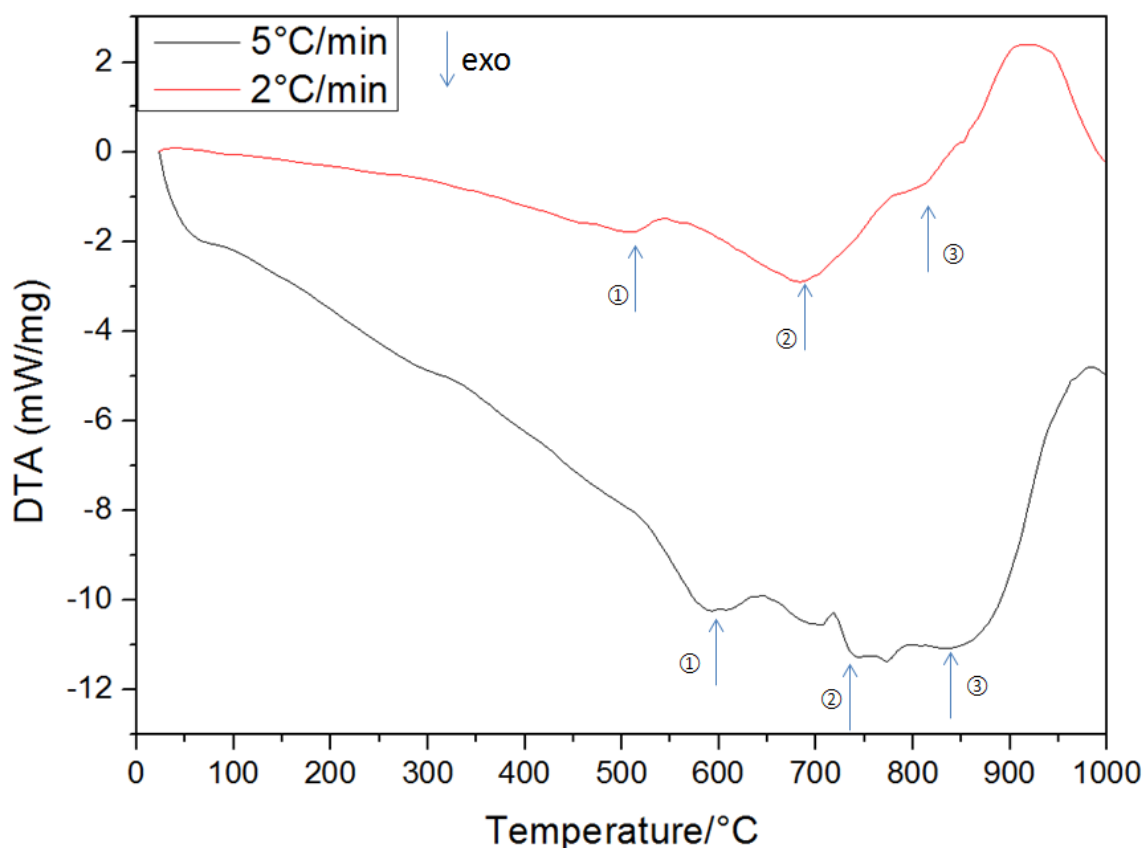
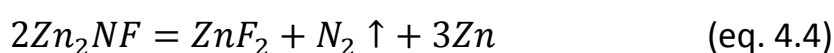


Figure 4. 15 DTA curve vs temperature for sample 12 (Zn_2NF) under the conditions used in Figure 4.14.

The MS analysis (Figure 4. 16) revealed that the mass loss observed in the TG curve corresponds to a nitrogen loss. In the $2\text{ }^\circ\text{C}/\text{min}$ scan the N_2 release occurs at a slower rate compared to the $5\text{ }^\circ\text{C}/\text{min}$ scan, resulting in less mass loss for the former. No other types of MS signals were detected, excluding the release of other elements. However, vaporisation of Zn was not possible to observe probably because the metal vapours condensate on the connection line between the STA furnace and the MS instrument. Combining these results with the previous hypothesis about the mechanism of Zn_2NF decomposition, this reaction can be observed starting from $600\text{ }^\circ\text{C}$ and described as:



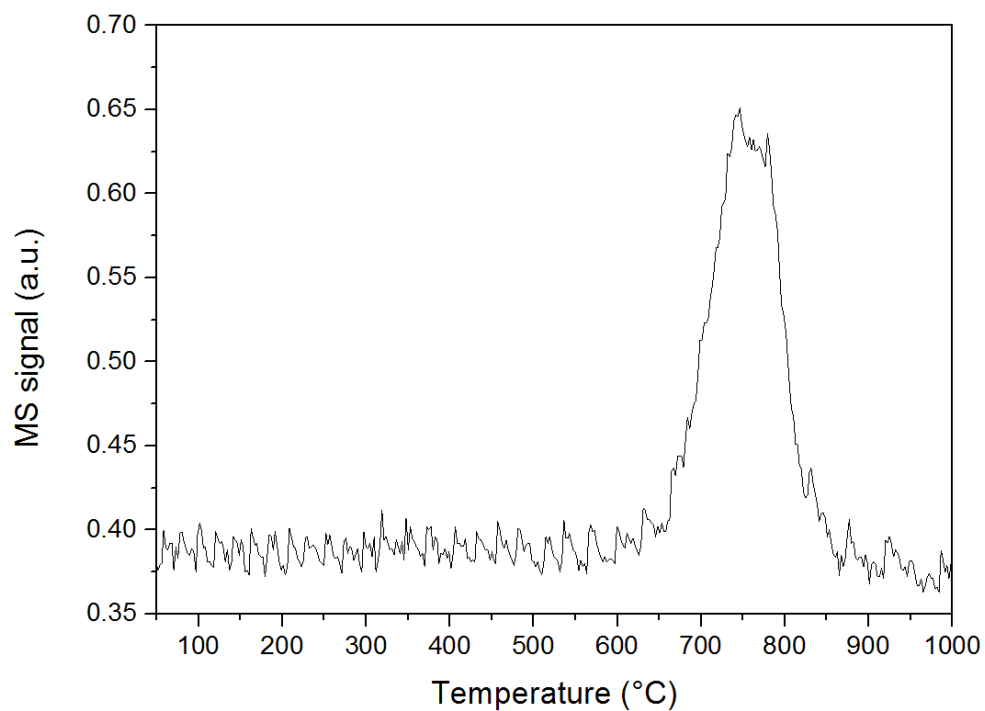


Figure 4. 16 N₂ evolution profile of the decomposition of sample 12 Zn₂NF powder with 5°C/min heating ramp

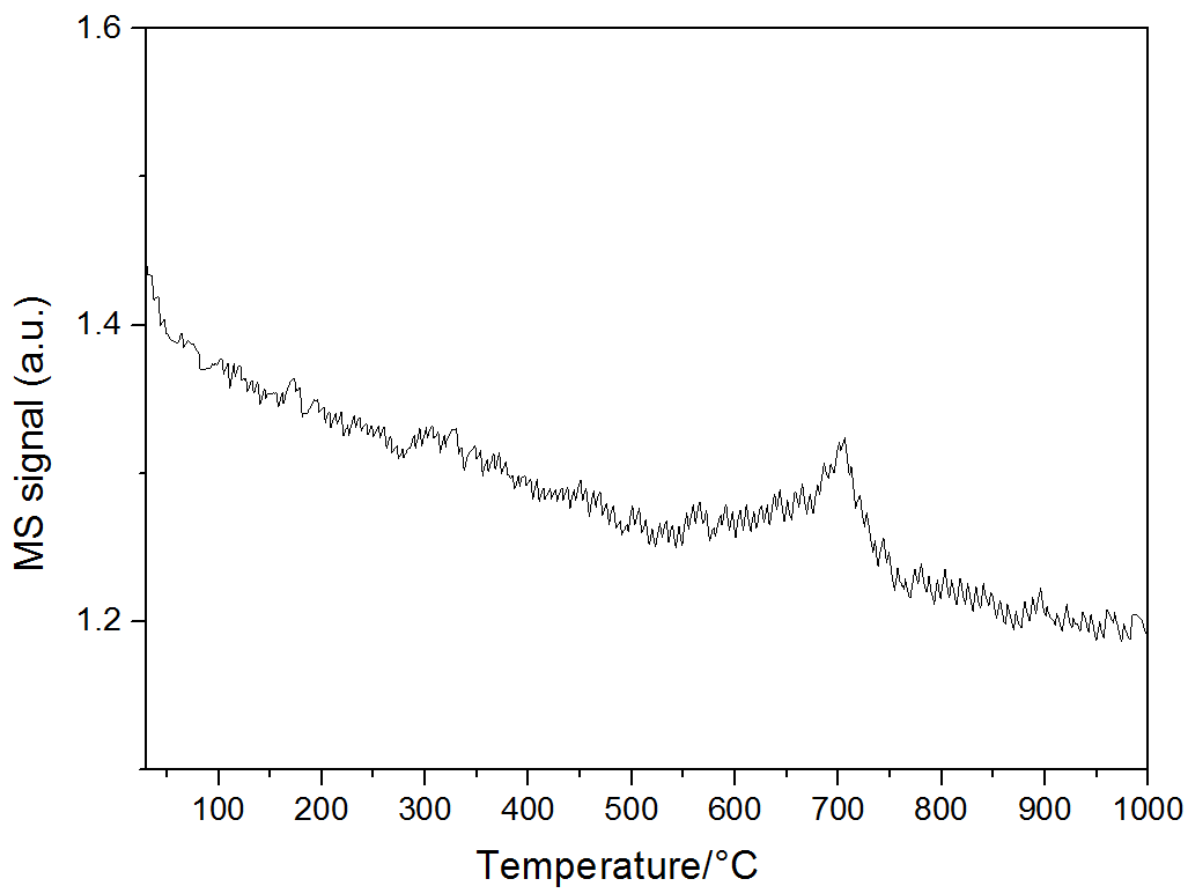
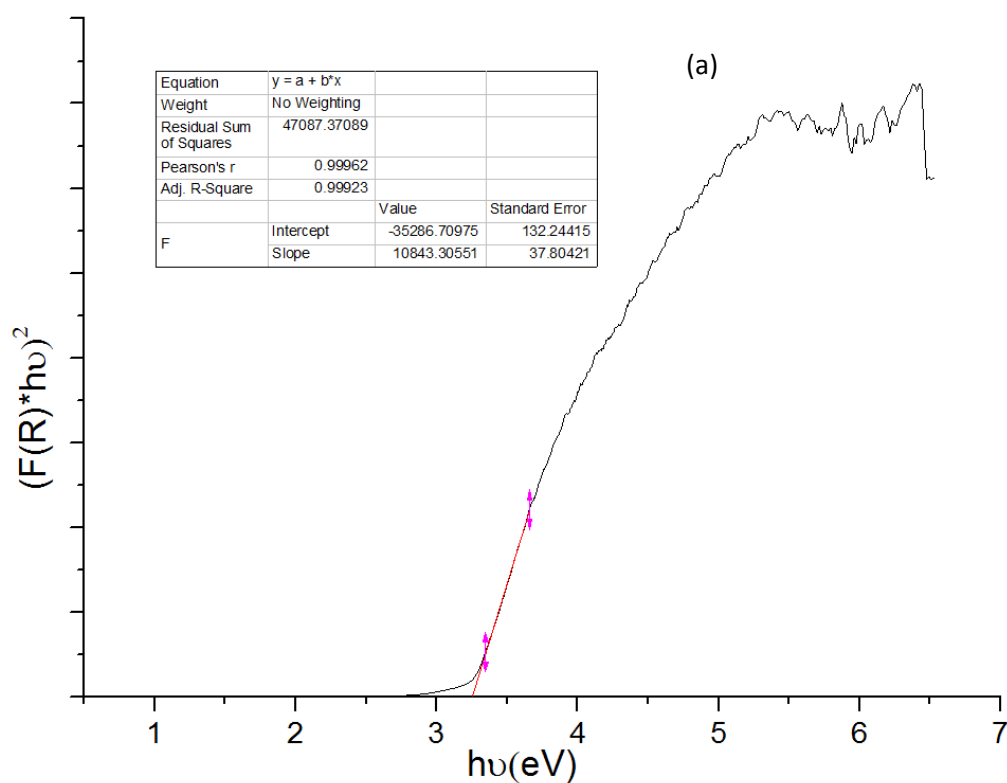


Figure 4. 17 N₂ evolution profile of the decomposition of sample 12 Zn₂NF powder with 2°C/min heating ramp

4.4 Optical properties

The band gap of Zn₂NF synthesised at different temperatures was calculated by measurement of the diffuse reflectance by UV-vis spectroscopy. The samples prepared at 500 °C, 650 °C and 700 °C (sample 11, 12 and 13) were compared in order to study the variation of the optical properties as a function of synthesis the temperature. Figure 4. 18 shows the transformation of the Kubelka-Munk function for the three samples. The material was previously reported to have a direct band gap^[46] and this reason a value of n=2 was used for the calculation of the band gap.



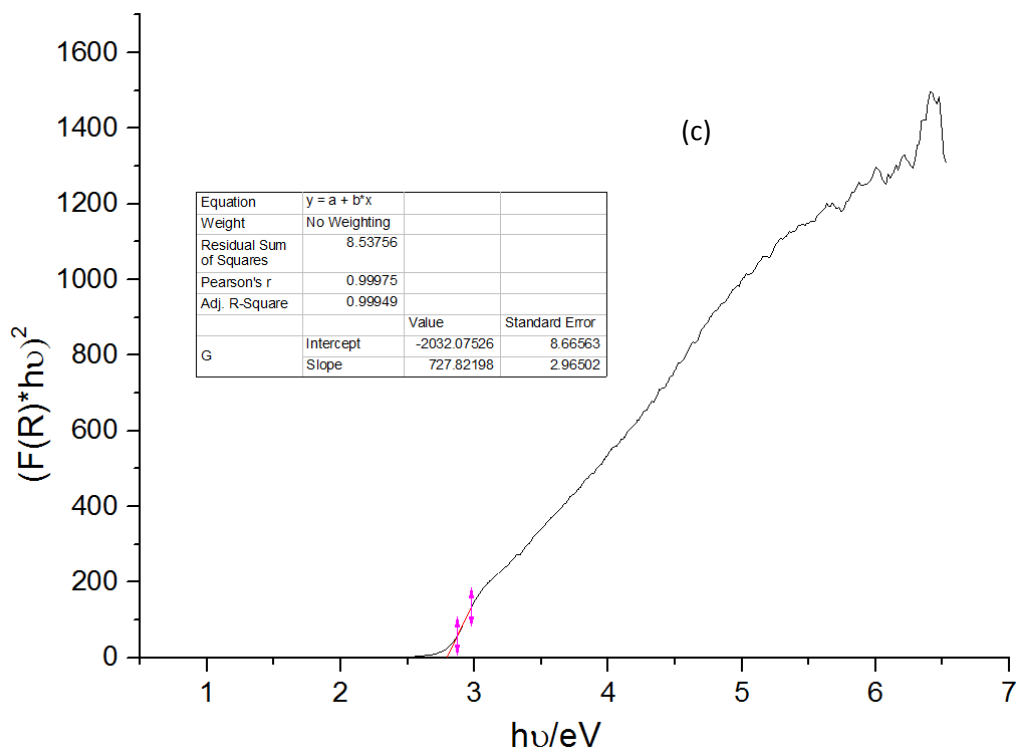
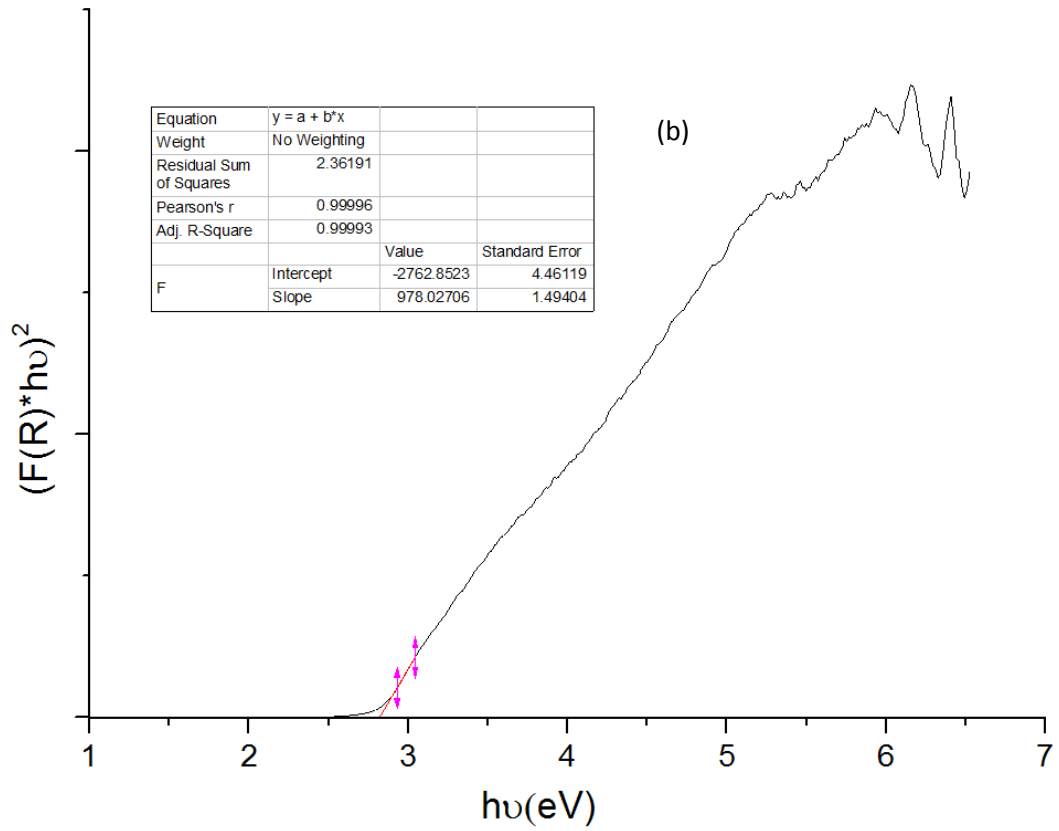


Figure 4. 18 Plot of the Kubelka-Munk function where $n=2$; vs $h\nu$ for samples synthesised at (a) 500 °C; (b) 650 °C and (c) 700 °C

The 500 °C-Zn₂NF (sample 11) has a direct band gap of 3.25 eV, whereas the Zn₂NF powder synthesized at 650 °C (sample 12) and 700 °C (sample 13) has a band gap of 2.82 eV and 2.79 eV respectively. All these three samples band gaps are lower than the direct band gap of ZnO (3.37eV) which lies in the visible light region. Considering the isoelectronic nature of 2[O²⁻]=[N³⁻F], the combination of nitrogen and fluorine narrows the band gap energy with respect to the presence of oxygen species only such as in ZnO.

It is notable that the direct band gap is very similar for the samples synthesized at 650 °C and 700 °C. From PXD patterns, the Zn₂NF high-temperature phase is the predominant phase in both samples and the band gap in both samples is very close to the value of 2.8 eV reported in literature⁴⁶. The differences between the band gap values of Zn₂NF produced at 650 °C and 700 °C can be attributed to systematic errors committed during the measurement or the linear fit of the optical functions rather than a relevant effect of the different temperatures. Since it was not possible to obtain the corresponding low-temperature phase in this work, no evidence is available to confirm the existence of an even lower band gap energy for the orthorhombic structure Zn₂NF, as reported elsewhere.^[46] However, the sample obtained at lower temperature (500°C-Zn₂NF), which has a band gap closer to ZnO than Zn₂NF.

4.5 Zn₂NF photodegradation test

Controlled degradation of Rhodamine B was used as a test to assess the photocatalytic properties of the samples. Since the Zn₂NF band gap is lower than ZnO according to our observations, Zn₂NF can be considered as a potential photocatalytic material in the visible light region. The degradation test results were compared to the performance of a commercial titanium oxide-based photocatalyst (Aeroxide[®] P25, ACROS, 99.5%), used as a reference

material due to its outstanding and undisputed photocatalytic properties. Zn₂NF powder was dispersed in a Rhodamine B solution ($1.5 \cdot 10^{-5}$ M), with a catalyst concentration of 0.5 g/L. A second suspension using TiO₂ P25 was prepared in the same way at the same concentration. Sonication and stirring were used to ensure the powder dispersion in the solution. The concentrations of the solutions after stirring were considered as the concentration at time 0. The solutions were tested under UV and visible light irradiation. The selected time data point set for the two different sources of light were different, since usually degradation under UV light is faster, requiring less time compared to the same process under visible light. The time at which small quantities of solutions (*ca.* 1.5 mL) were collected were at 0, 5, 10, 15, 20, 30, 40, 50, 60 minutes for UV and at 0, 10, 20, 30, 45, 60, 90, 120, 180 minutes for visible light.

At each point indicated, the collected volume was centrifuged for 20 minutes at 4000 rpm. After that, the powder precipitates at the bottom, allowing the collection of the supernatant and the measurement of the absorbance spectrum to determine the effect of the degradation. The degradation curves, calculated correlating the measured absorbance intensity at 554 nm for each exposure time selected, are shown in Figure 4. 19.

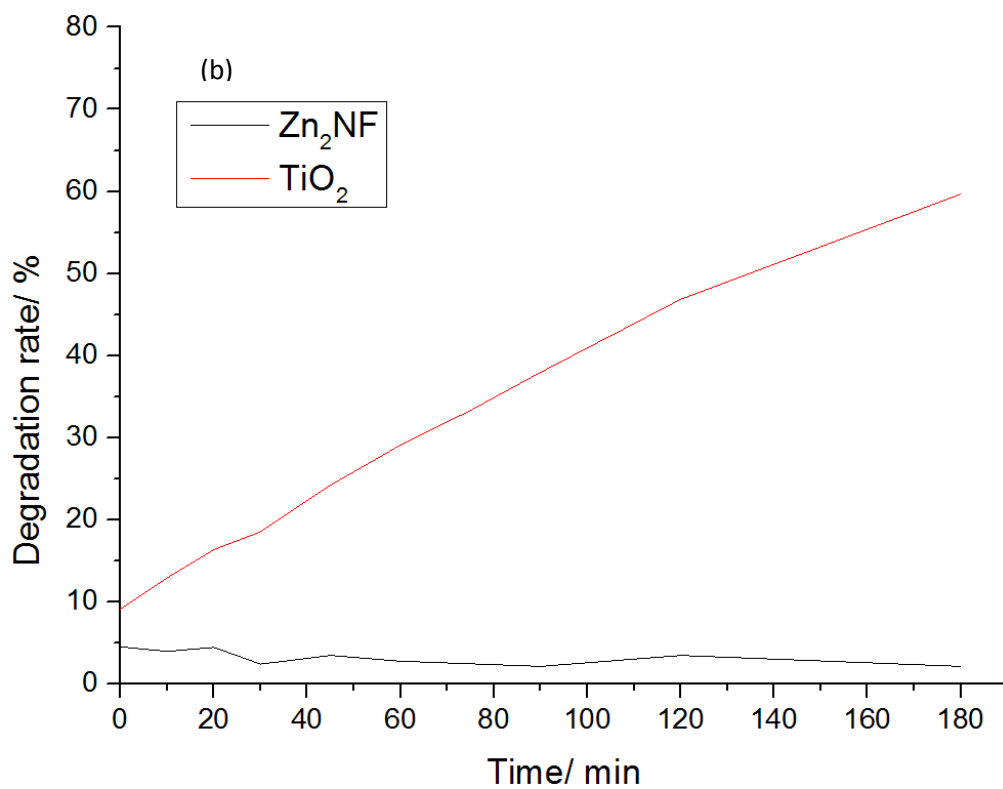
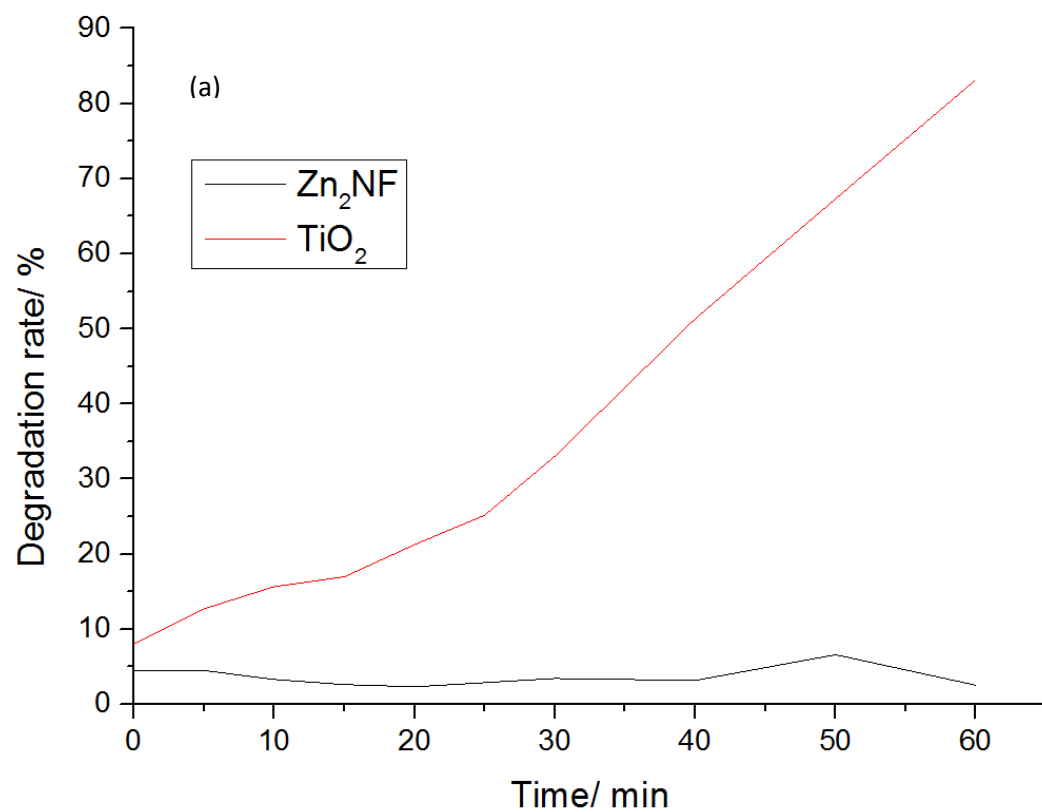


Figure 4. 19 Photodegradation curves of Zn₂NF (sample 13) and TiO₂ under (a) UV light and (b) visible light respectively

As can be observed from the degradation profiles, the Zn₂NF sample do not show any appreciable photocatalytic property under either UV or visible light. The small fluctuations of concentration during the degradation experiment are mainly due to systematic errors in the measurement or the eventual evaporation of Rhodamine B solution, since even a small evaporated volume can affect the very low concentration of Rhodamine, showing a mild re-concentration effect. After the degradation tests, the used Zn₂NF was recollected from the solutions. The powders were twice centrifuged and washed with water to remove the Rhodamine B adsorbed to the surface. The collected powder was then dried overnight at 50 °C in a drying oven.

The dried powder was characterised by PXD, SEM and EDX, to determine if any changes had occurred to the sample following the dye degradation test.

As shown in the XRD patterns in Figure 4. 20, sample 13 contains considerably more ZnO following the dye degradation process. Zn₂NF clearly remains in the sample, however, the pattern of the material after the degradation test is less defined compared with the one prior to the test (despite data collection under the same instrumental conditions). The presence of a higher background and a lower signal-to-noise ratio potentially indicate the presence of amorphous compounds in the material after testing. The marked changes in the morphology of the material can be seen in the SEM (Figure 4.21).

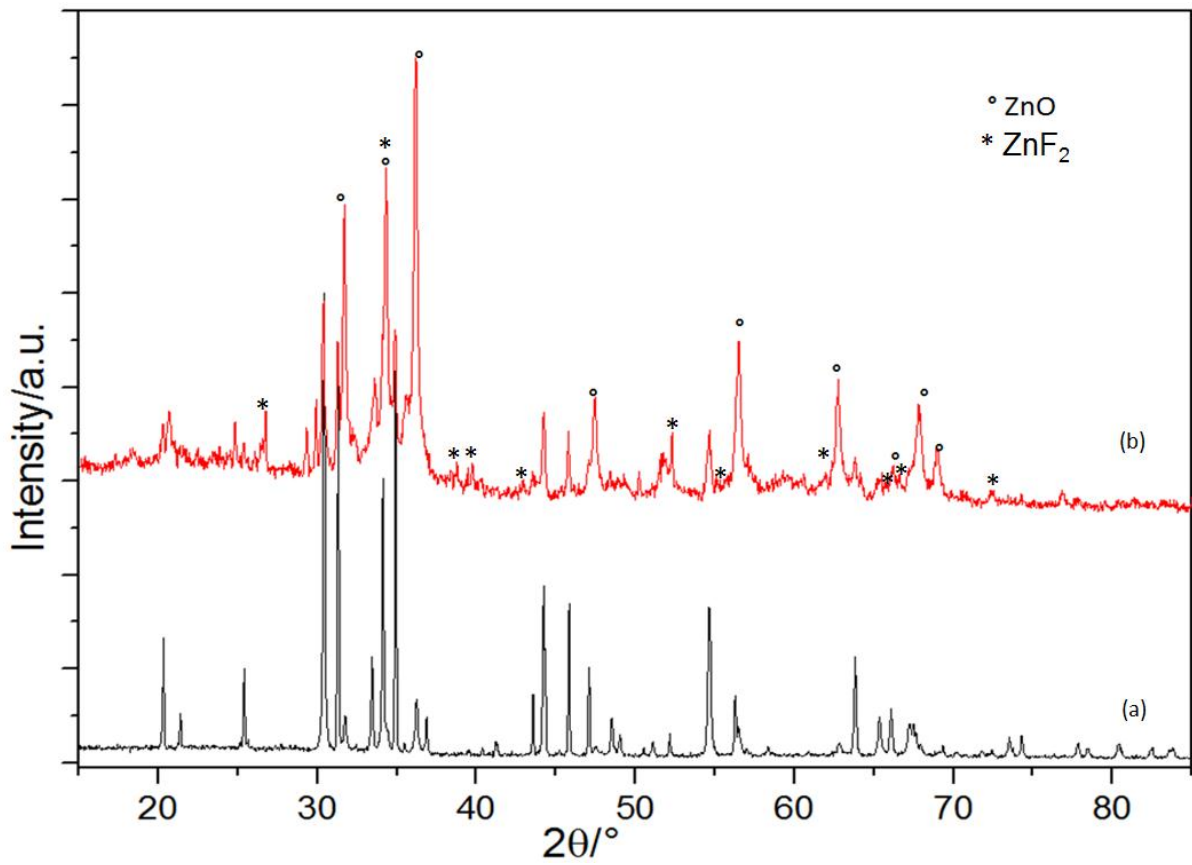


Figure 4. 20 PXD pattern of sample 13 (a) before and (b) after the photodegradation experiment.

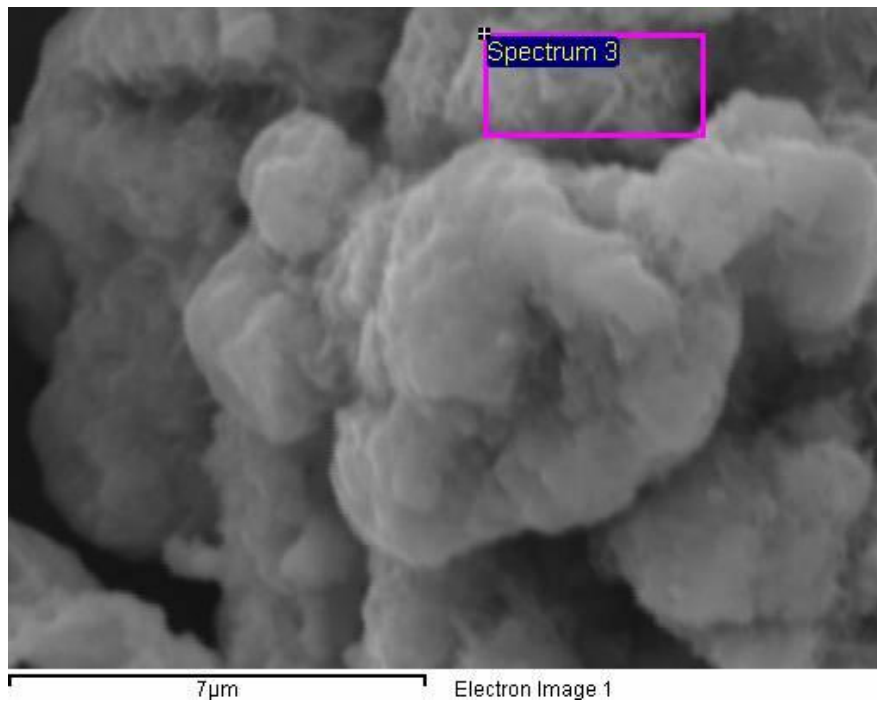


Figure 4.21: SEM image for recollect Zn₂NF powder

Elemental analysis by EDX of sample 13 after testing showed an increase of the signal associated with oxygen with a concomitant loss of nitrogen (Figure 4. 22). The atomic composition of the sample before and after the degradation test is reported in Table 4. 5:

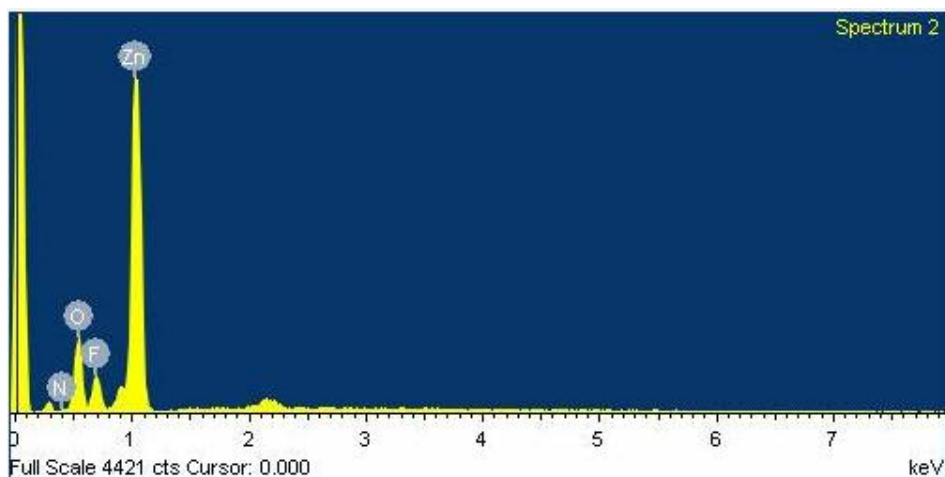


Figure 4. 22 EDX spectrum for sample after the dye degradation test

Table 4. 5 : Average atoms ratio of Zn₂NF before and after degradation test

	Zn	N	O	F
Before	34.13%	22.84%	6.96%	36.08%
After	49.48%	1.48%	34.40%	14.38%

EDX results provided further evidence for the large increase of ZnO in the sample after testing.

The results from PXD and SEM/EDX suggest that Zn₂NF may react with water. This possible reaction could be the main reason for the poor performance of the material as a photocatalyst. Even if Zn₂NF is photoactive, the results suggest that the material is unstable in an aqueous environment, which would render it completely ineffective for the photocatalytic splitting of water, for example. Furthermore, the dispersion of Zn₂NF in water is poor compared with materials such as TiO₂, which TiO₂ has highly hydrolysed surface that makes

the material suitable for homogeneous dispersion in solution. The dispersion of Zn₂NF powder was unstable often with sudden a precipitation of the solid after several minutes at which point it became difficult to redisperse even when stirred. The crystallite size of the powder and the very low surface area arising the multiple thermal treatments might be further reasons for the poor affinity of Zn₂NF with water.

4.6 Zn₂NF refinement

The Rietveld refinement was performed against the PXD data of Zn₂NF powder synthesised at 650 °C (sample 12) to compare the structure with the ones reported in literature. The structure reported by Lingampalli *et al.* [46] was used as a model for the refinement. Furthermore, a cel file was generated from these data as starting model using PowderCell 2.4 software to create the .cel file for the starting model. The calculations were performed using EXPUGUI-GSAS software. Since the material is not presenting only a single phase, two other phases other than tetragonal Zn₂NF were considered, ZnO and Zn-O-N-F, the latter presenting the same structure of ZnO but with substitution of the oxygen position by the other two non-metals, with occupancies of 0.4, 0.3 and 0.3 for O, N and F respectively.

The results of refinement are reported in Figure 4. 23 and Table 4.6, with the refined atom coordinates for Zn₂NF structure listed in Table 4.6.

Table 4. 6 Crystallographic information obtained from refinement of Zn₂NF

Crystal system	Tetragonal
Space group	P4 ₁ 2 ₁ 2
Lattice parameters	a= b=5.873(16)Å, c=6.53206(19)Å
Lattice angle	$\alpha= \beta= \gamma= 90^\circ$
Z	16
Volume	225.305(11)Å ³
Unit cell formula weight	655.060
Density	4.828 g/cm ³
wRp	15.08
Rp	11.24
χ^2	7.987

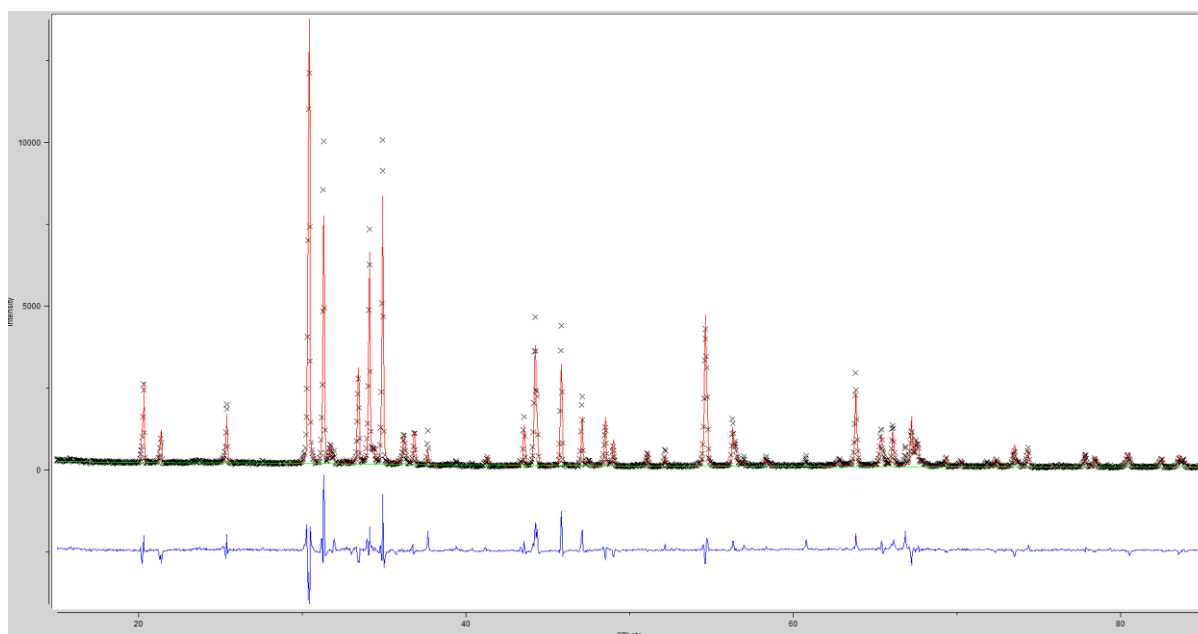


Figure 4. 23 Rietveld refinement for sample 12 Zn₂NF. Red line for calculated data, black crosses for experimental observations, green line for background curve, blue line for the difference between calculated and observed patterns.

Table 4. 7 Refined atomic parameters of the phase in sample 12

Atomic parameters						
Atom type	Wyckoff Site	Fractional Coordinates			Uiso /Å ³	Occupancy
		x	y	z		
Zn(1)	8b	0.2777(34)	0.3497(4)	0.21923(32)	0.025(1)	1.0
N(1)	4a	0.1784(27)	0.1784(27)	0	0.081(9)	1.0
F(1)	4a	0.7916 (13)	0.7916 (13)	0	0.036(1)	1.0

The cell parameters and the bond length are very similar in comparison with previous results reported by Lingampalli *et al.*. In both refinements the presence of ZnO was assumed as second phases.

Chapter 5: Doped-ZnO materials

5.1 Doped-ZnO materials synthesis and characterisation

According to the work of Lingampalli et al.,^[46] Zn₂NF shows the same photocatalytic properties as ZnO, with enhancement of these properties under visible light because of a narrower band gap, induced by the combination of N³⁻ and F⁻ anions replacing O²⁻. The complete replacement of oxygen atoms is the ultimate consequence of the doping process on ZnO with insertion of non-metallic elements. The 2p orbitals of elements such as N and F combine with the same zinc valence orbitals as the oxygen atoms, lowering the width of the forbidden energy region from values corresponding to UV frequencies to visible-light wavelength and extending the photocatalytic response of the material in this spectral range.

Nitrogen doping of ZnO has been widely reported.^[68,92,93] Unlike other materials (such as TiO₂), the production of doped material is achieved most easily by oxidizing the fully nitrated form, starting from Zn₃N₂ as a powder or thin film. Nitriding the oxide would be less favourable due to the lower energy of oxidation of Zn₃N₂ compared to that for nitriding ZnO. Moreover, fluorine doping has been reported to confer anti-bacterial properties on ZnO, with an additional improvement of the photocatalytic properties compared to bare ZnO under visible light.^[76] The usual preparation method for F-doped ZnO involves thermally heating a mixture of ZnO and ZnF₂.^[66,94] Co-doping of N and F has been also reported with promising results for hydrogen generation. Altering the ratio of O, N and F in the co-doped structure can determine the final properties of the material.^[46,69,95] However, co-doping mechanisms are

still unclear and the reactions are hard to control to select a final product with the optimal concentration of the three non-metals.

Various attempts to replicate and improve the preparation of doped ZnO using different methods are reported in this chapter. The control of the material composition was performed first by careful selection of different precursor materials. Full characterisation of the produced materials should help to improve the knowledge of the properties of the resulting materials and the mechanism of N and F doping in ZnO.

The doping procedures were categorised according to the selection of the precursor material. Thermal synthesis in the presence of NH_4F under a reactive atmosphere was considered using ZnO as starting material. Ammonium fluoride was used as source of fluorine, with the reaction promoted by the reductive atmosphere of NH_3 , which could facilitate also the insertion of N atoms into the ZnO structure. ZnO nanoparticles have been synthesised by a sol-gel method as reported by Harun et al.^[96] Commercial zinc acetate dihydrate (Acros, 98%), sodium hydroxide (pellets, Alfa Aesar, 99.99%) and methanol (Fisher, $\geq 99.9\%$) were used as starting materials. As an alternative, ZnF_2 was nitrated via thermal ammonolysis (and decomposition of NH_3 at high temperature). The use of zinc powder as a precursor was also considered due to the low oxidation energy of Zn in metallic form and its higher chemical activity compared to ZnO. This last procedure involves a thermal treatment of Zn powder in the presence of NH_4F under either an NH_3 atmosphere or under vacuum. The initial masses of the reactants for each method are reported in Table 5.1, whereas the precise reaction conditions are reported in Table 5.2.

Table 5.1 : Mass of the reactants for the set of ZnO doping mass of reactants of experiments

Reaction	ZnO/g	Zn/g	ZnF ₂ /g	NH ₄ F/g
1,2	0.15	-	-	1.5
3,4	-	-	2	-
5	-	0.15	-	1.5
6,7	-	0.25	-	0.5

Table 5.2: Summary of ZnO doping experiment conditions

Reaction	Precursors	Temperature/°C	Duration time/h	Atmosphere
1	ZnO+NH ₄ F	600	2	NH ₃ (g)
2	ZnO (NPs)+NH ₄ F	600	2	NH ₃ (g)
3	ZnF ₂ +NH ₃	600	3	NH ₃ (g)
4	ZnF ₂ +NH ₃ (2 nd cycle)	600	3	NH ₃ (g)
5	Zn+NH ₄ F	600	2	NH ₃ (g)
6	Zn+NH ₄ F	500	5	Vacuum/ 2.1·10 ⁻² mbar
7	Zn+NH ₄ F	500	5	Vacuum/ 1·10 ⁻⁵ mbar

Both powdered ZnO and nanoparticles (marked as NPs in Table 5.2) were used for the doping procedure, resulting in different final products.

Ammonolysis of ZnF₂ was performed in several cycles, using the product of the previous reaction 3 for the following one (reaction 4). For the reaction of zinc powder with NH₄F under vacuum, the two starting materials were placed in a sealed stainless steel reactor, lowering the internal pressure to 2.1·10⁻² mbar or to 1·10⁻⁵ mbar, using a rotary pump or a turbo molecular pump, respectively.

All the reactants were mixed and ground, with the mixture placed into alumina crucibles or boats.

The ammonolysis reactions ZnO and NH₄F (reactions 1 and 2) were performed with an excess of the latter, in order to compensate for the thermal decomposition of ammonium fluoride into NH₃ and HF at low temperature (around 100 °C and well below the planned synthesis temperature). For the same reason, the reactions under vacuum (reactions 6 and 7) were performed with an excess of Zn in order to avoid the increase of NH₃ and HF partial pressure inside the reactor and any possible risks related to the high reactivity and corrosive power of these two gaseous compounds.

All the products were characterised by PXD analysis to identify phase composition and crystal structures as shown in Figure 5.1 错误!未找到引用源。 .

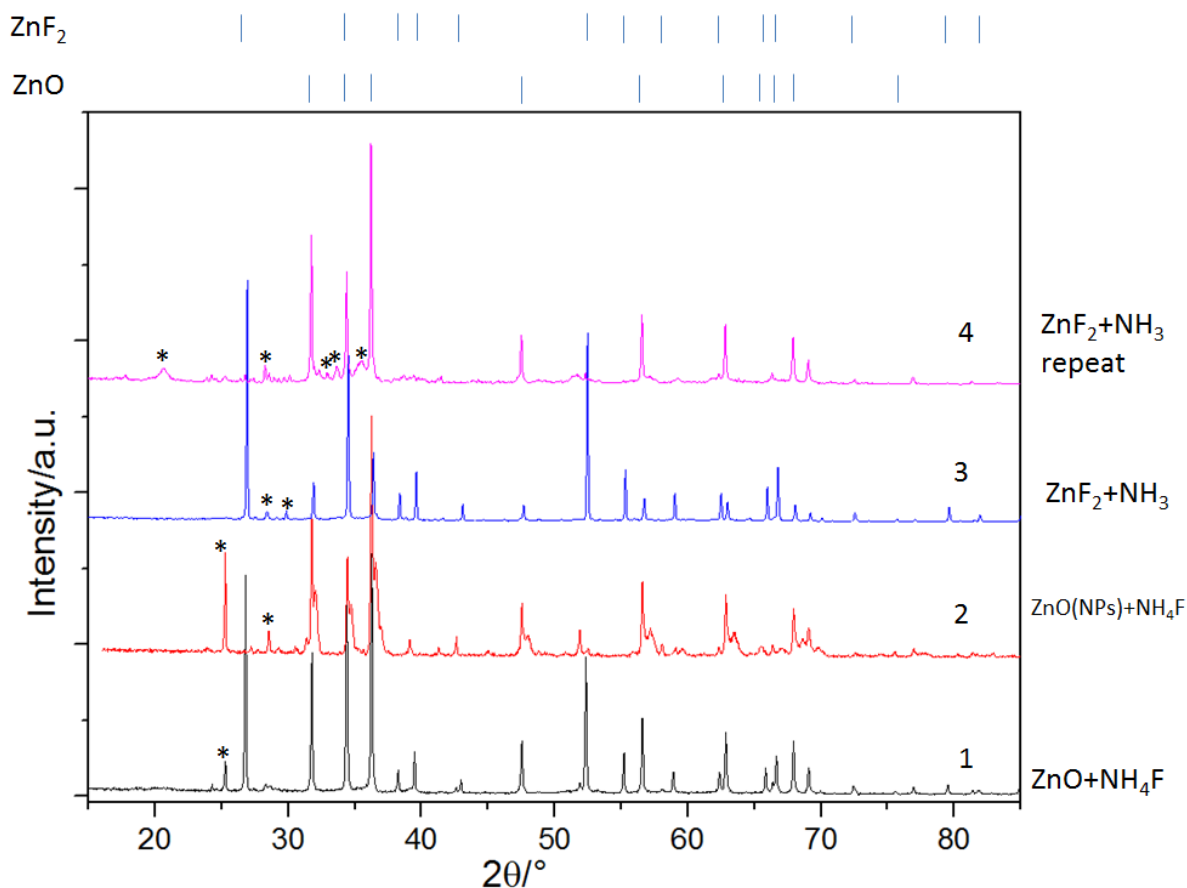


Figure 5. 1 Powder XRD comparative analysis for the products of ZnO doping experiments, using ZnO and ZnF₂ as precursors

Considering the doping reactions which involved ZnO and ZnF₂, each starting material is still present in the resulting products. However, the presence of broader peaks and/or shoulders indicates the existence of different structures and/or additional phases depending on the different reaction precursors and conditions. The use of bulk ZnO powder vs ZnO nanoparticles had a different effect on the structure of the resulting products, with an apparent lower relative intensity of the ZnO and ZnF₂ PXD peaks when nanoparticles were used (sample 2).

The ammonolysis reaction of ZnF₂ resulted in the formation of ZnO peaks, despite the absence of oxygen in the precursors and its limited presence in the reaction atmosphere (sample 3). In order to increase the efficiency of nitrogen doping, the same reaction was cycled a second time using the first cycle

products under the same reaction conditions (sample 4). Sample 4 contained ZnO but ZnF₂ become almost absent. The origin of the oxygen source was unclear. Further investigation on the reaction conditions was not fully developed due to limited time scale of the project.

Figure 5.2 shows the colour of the final products of the two syntheses previously described (sample 2 and 4). Both precursors (ZnO and ZnF₂) appear as pure white powder. After the reaction, both products show a similar homogenous brown colour. The two doping procedures caused a chromatic alteration of the material, despite the principal crystalline phase being ZnO by PXD. The colour change and the preservation of the original crystalline structure are a first indication of the efficient insertion of nitrogen and fluorine atoms into ZnO structure. Further characterisation of the elemental composition of the sample by EDX was performed (see section 5.2).

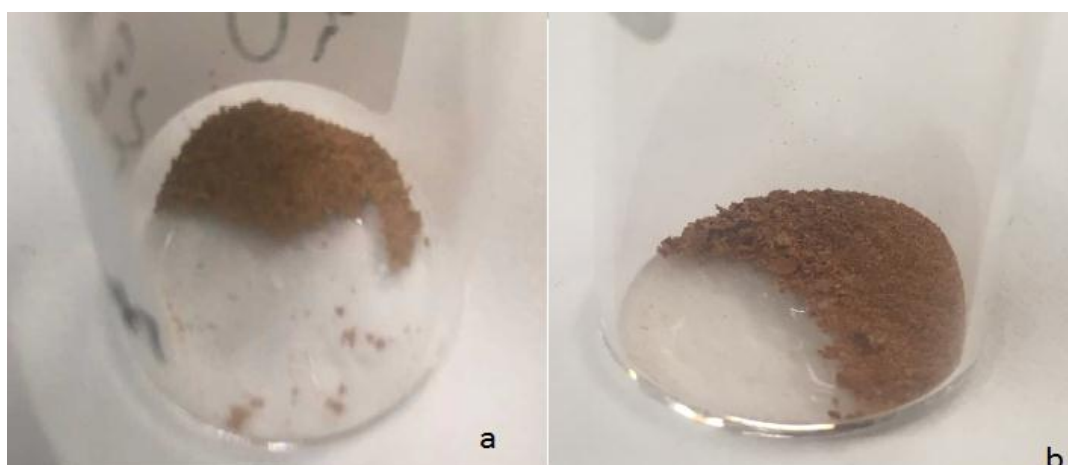


Figure 5.2: Images of the final products of the zinc oxide-ammonium fluoride synthesis (a) sample 2 and the ammonolysis of ZnF₂ reaction product (b) sample 4

Similar to the doping procedures using ZnO and ZnF₂ as starting material, Zn powder appeared not to be a successful precursor, with all the tested reactions leading to almost total conversion to ZnO according to PXD patterns (Figure 5.

3). However, the structure of the ammonolysis product of Zn powder showed some similarities with the structure obtained by ammonolysis of ZnO nanoparticle in presence of NH_4F .

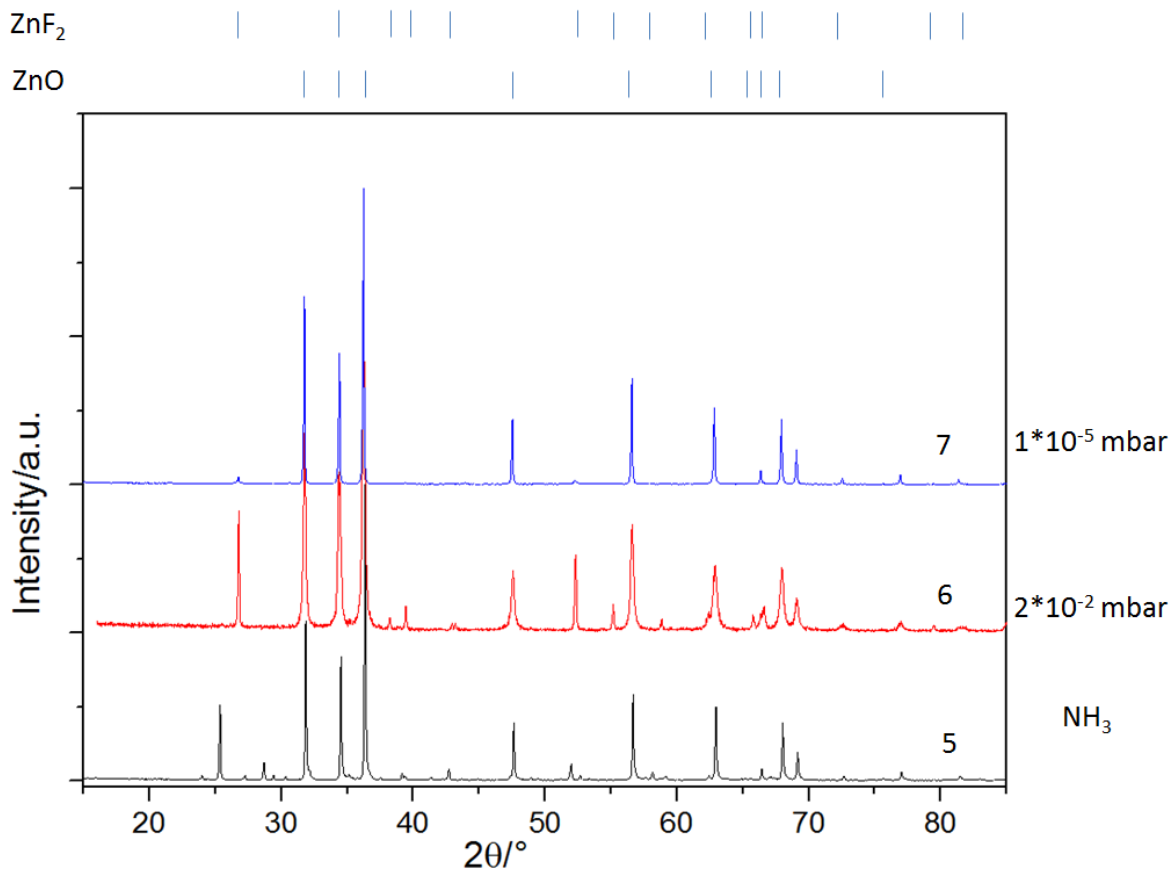


Figure 5. 3 ZnO doping experiments using Zn powder as precursor sample 5-7

The role of the NH_3 in the $\text{Zn}+\text{NH}_4\text{F}$ reactants affect to be essential for successful doping, with the reactive NH_3 atmosphere providing the main source of nitrogen according to the PXD results. Comparing the PXD pattern of the reactions performed under NH_3 atmosphere and vacuum, the only sample to contain reflections in addition to those of ZnO and/or ZnF_2 was sample 3 (where all the ZnF_2 appeared to have been consumed). Another interesting observation is the total absence of Zn_3N_2 after the ammonolysis of Zn powder in presence of NH_4F . The same temperatures and experimental conditions used

for the synthesis of zinc nitride from Zn and NH_3 (as reported in the previous sections). Hence the presence of NH_4F appears to have an important effect.

The final product of Zn ammonolysis in presence of NH_4F showed a dark orange colouration (Figure 5.4). This is striking considering the grey colour of the mixture composed of Zn powder and ammonium fluoride. There is some similarity in colour, therefore, with the products of ZnF_2 ammonolysis (Figure 5.2).



Figure 5.4: Final product of Zn+ NH_4F reaction under NH_3 flow

5.2 Doped-ZnO materials: SEM and EDX analysis

The products from the different ZnO doping reactions were further characterised by SEM and EDX analysis in order to understand the effect of the doping procedures on the morphology and the elemental composition of the products. All reactions (ZnO or Zn powder with NH_4F samples 1, 2, 5 or simply ZnF_2 samples 3, 4) resulted in brown or orange products, with colours that appeared darker than that observed for Zn_2NF and were very different from the starting materials. All these products are mainly composed of ZnO, according to their PXD patterns (Figure 5.1).

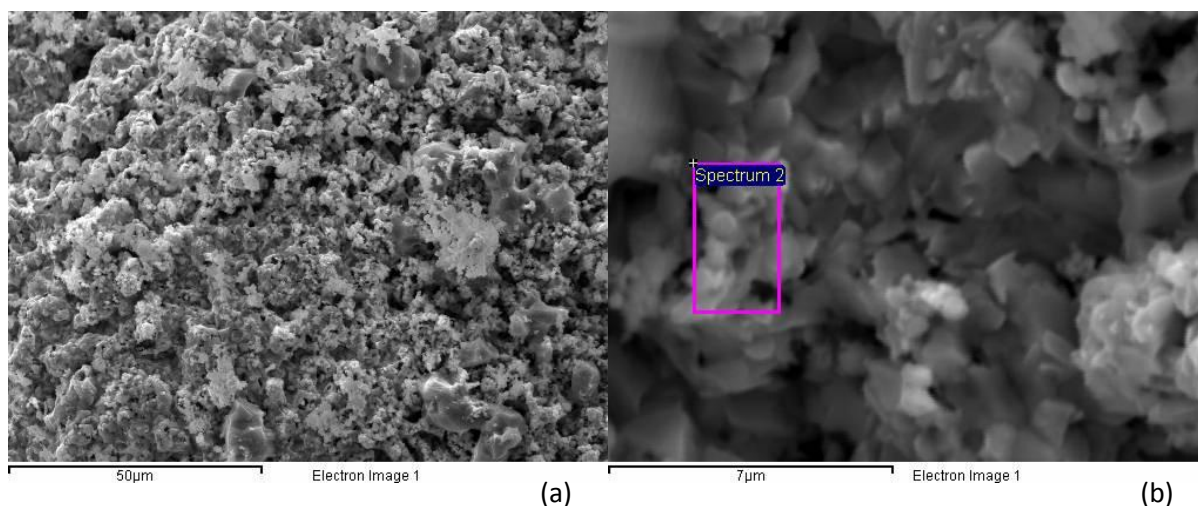


Figure 5.5 SEM image of the product resulting from the ammonolysis of ZnO and NH_4F at (a) low magnification and (b) higher magnification images.

SEM images of the products of the ammonolysis of ZnO/ NH_4F (Figure 5.5) revealed a morphological structure composed of irregular blocks with smaller particles distributed on the block surfaces.

The other two ammonolysis reactions (using Zn and ZnF_2 , samples 4 and 5) showed similar morphologies to the one observed for sample 2 (Figure 5.6). However, the formation of almost cubic blocks is more evident in these

products. The samples were also more crystalline, as witnessed by the shape of powder PXD patterns. The cubic blocks resulting from the ammonolysis of Zn in presence of NH_4F (sample 5) showed an average size of *ca.* 530 nm (estimated measuring 20 particles randomly selected across the SEM images). The smaller particles on the surface may also correspond as well to the formation of doped ZnO, perhaps with a different composition compared to the cubic blocks. These structures could result from the incorporation of nitrogen and fluorine on the oxidizing surface of the metal during the reaction under an ammonia flow.

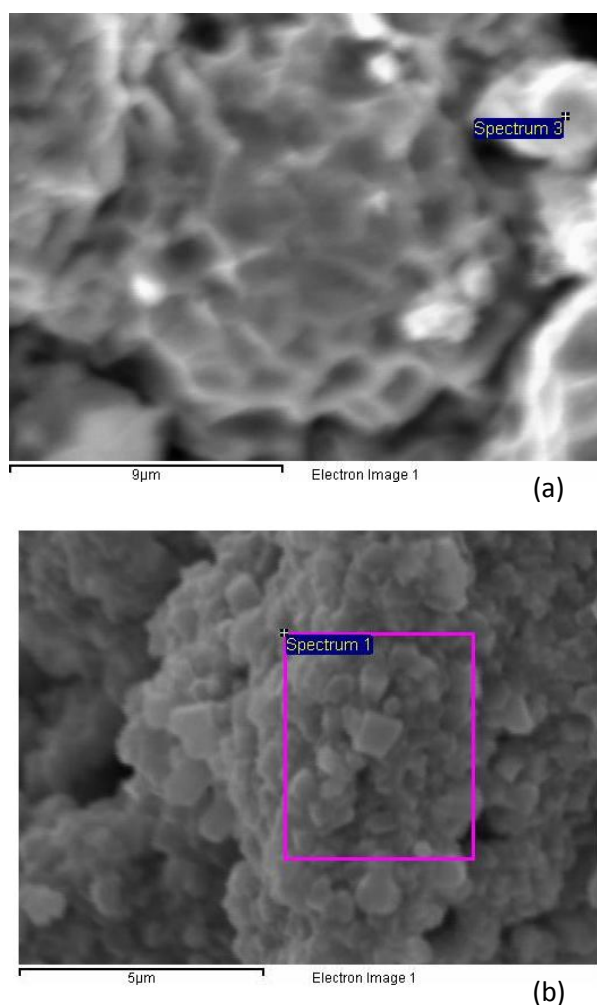


Figure 5. 6 SEM images of ZnF_2 ammonolysis reaction product ((a) for sample 4) and $\text{Zn}+\text{NH}_4\text{F}$ ammonolysis reaction product ((b) for sample 5)

The elemental composition by EDX analysis for the products of the three different doping methods is reported in Table 5.3. The analysis cannot be considered totally accurate due to the low sensitivity of EDX towards lighter elements of the periodic table; i.e. all three of the constituents of the materials examined. Considering the atomic concentration, ammonolysis of Zn powder ($\text{Zn}+\text{NH}_4\text{F}+\text{NH}_3$) showed the highest nitrogen and fluorine incorporation. Conversely, as was apparently the case during the synthesis of Zn_3N_2 (Chapter 3), since Zn powder is liquid at 500 °C, vaporization would occur during the reaction. The constant ammonia flow should act as a carrier gas, taking away Zn vapour from the reaction zone. Comparing the At% values of the products of the ammonolysis of ZnO (sample 2) and ZnF_2 (sample 4), the later contained more nitrogen and fluorine, which might be enhanced by cycling the reaction. Although the PXD pattern of this material showed mainly the presence of “ZnO”, the material appeared to be highly fluorinated. Conversely, ammonolysis of ZnO led to the lowest amount of N and F among the three series of reactions. This can probably be attributed to the high thermal stability of ZnO and the thermal decomposition of NH_4F during the reaction. The reactive atmosphere provided by the ammonia flow should encourage the NH_4F decomposition, with the resulting molecules (NH_3 and HF) carried away, preventing their reaction with ZnO.

Table 5.3: Average atom concentration in different ammonolysis products

Atom/% Reaction	Zn	N	O	F
$\text{ZnO}+\text{NH}_4\text{F}+\text{NH}_3$	35.10 ± 6	3.91 ± 1	39.08 ± 5	21.90 ± 5

ZnF ₂ +NH ₃ (2 nd)	42.54 ± 17	4.53 ± 4	23.97 ± 6	27.11 ± 9
Zn+NH ₄ F+NH ₃	17.76 ± 5	6.32 ± 4	25.67 ± 5	42.66 ± 9

Further characterization was performed in order to assess the optical properties of these materials, focusing on influence of nitrogen and fluorine on the band gap values. The ultimate aim of the doping process is indeed the narrowing of ZnO band gap to extend its photoactivity in the visible-light region.

5.3 Doped ZnO materials: band gap

The band gap measurement should clarify the relationship between the effect of nitrogen and fluorine doping on ZnO structure and the resulting optical properties. The band gap energy values for the ammonolysis reaction products were calculated using the Kubelka-Munk functions, applied to the reflectance spectra of the powdered materials, similar to the analysis previously performed on Zn₃N₂ and Zn₂NF (Chapter 3, section 3 and Chapter 4, section 4).

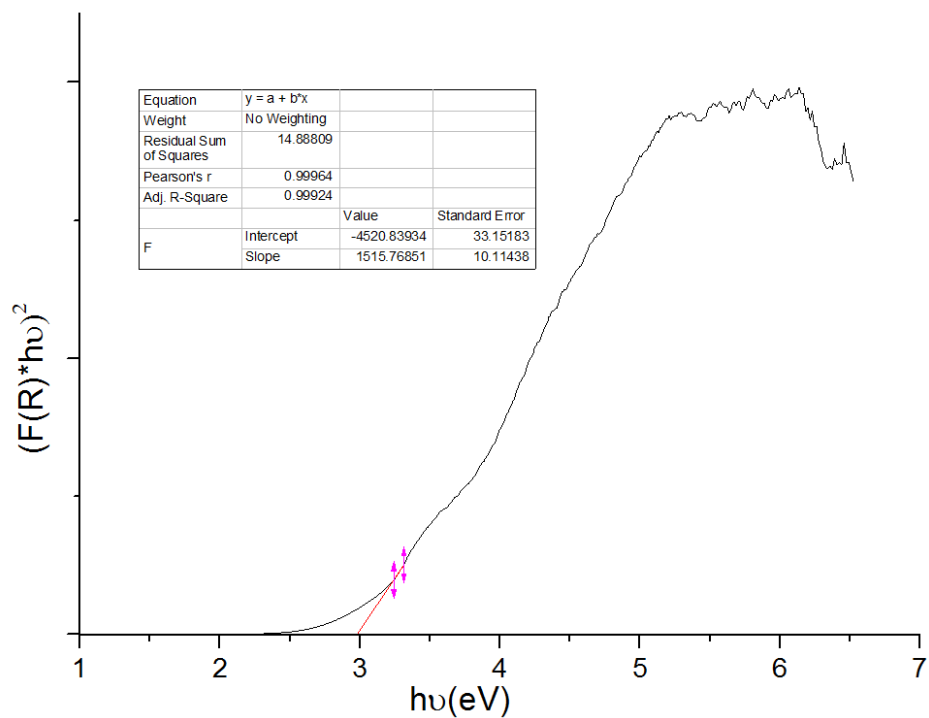


Figure 5.7: Calculation of the direct optical band gap of the product of ZnO ammonolysis ($\text{ZnO} + \text{NH}_4\text{F} + \text{NH}_3$) using the Kubelka-Munk function transformation

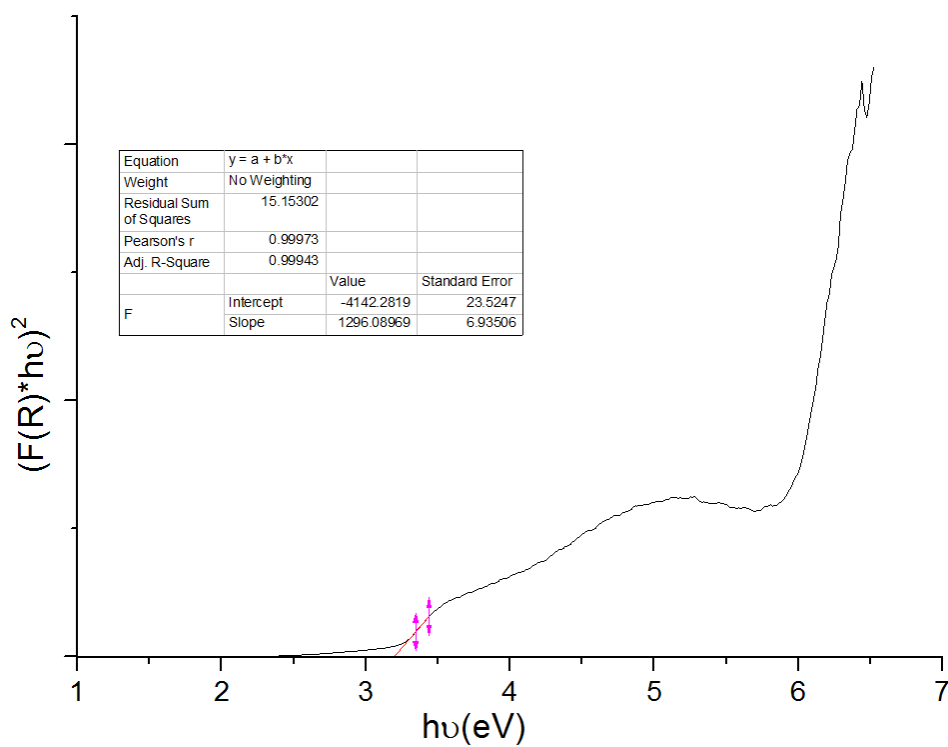


Figure 5.8: Calculation of the direct optical band gap of the product of ZnF_2 ammonolysis ($\text{ZnF}_2 + \text{NH}_3$, 2nd cycle)

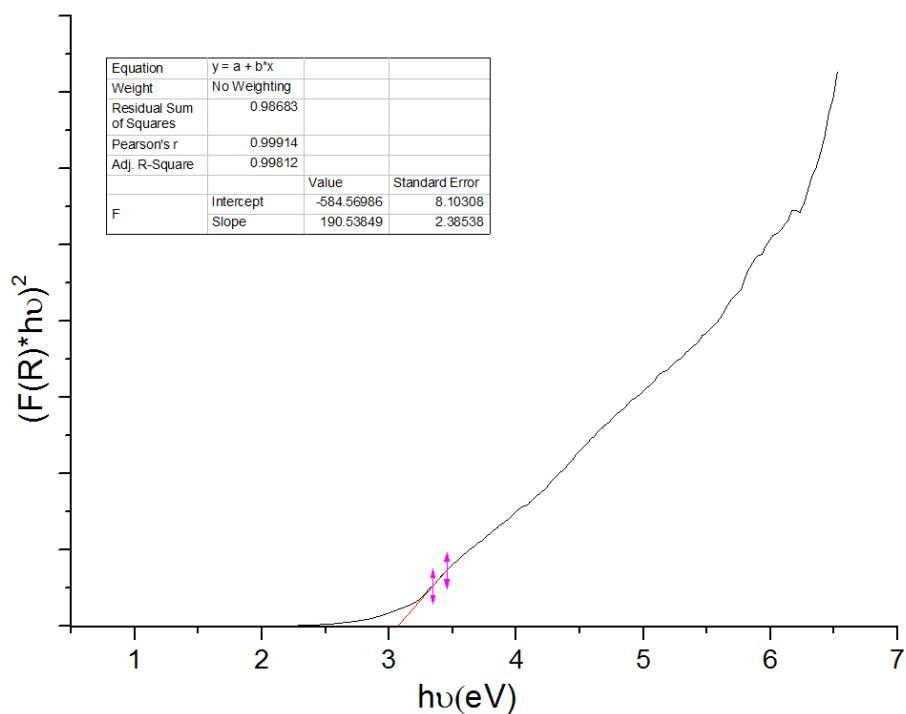


Figure 5. 9 Calculation of the direct optical band gap of the product of Zn powder ammonolysis (Zn+NH₄F+NH₃)

Table 5.4: Direct band gap of doped ZnO materials

Reaction	ZnO + NH ₄ F + NH ₃ (sample 2)	ZnF ₂ + NH ₃ (sample 4)	Zn + NH ₄ F + NH ₃ (sample 5)
Band gap			
Direct band gap	2.98 eV	3.20 eV	3.07 eV

The band gap values from samples 2, 4 and 5 are reported in Table 5.4, with the Kubelka-Munk function plots and calculations showed in Figure 5.7, Figure 5.8 and Figure 5. 9. Contrary to expectations, despite the lower concentration of dopants, the ammonolysis of ZnO resulted in a lower band gap compared to the other two materials. The highest band gap was achieved from the ammonolysis of ZnF₂, which was closest to the band gap of pure ZnO (3.37 eV). The three materials showed intermediate band gap values between that reported for ZnO and the one measured for pure Zn₂NF (2.8 eV, as reported in the previous chapter). The high band gap value resulting from the

ammonolysis of ZnF_2 can be explained considering the band gap of the original material, reported as 3.63 eV ^[97] and then higher than the ZnO band gap. The crystalline structure of ammonolysed ZnF_2 is closer to ZnO than the ammonolysis product of ZnO in presence of NH_4F . This last reaction led to a structure differing from the original ZnO crystalline structure more than any other doping products. The structural changes strongly affect the band gap, probably more than the insertion of the dopant with minor alteration of the lattice structure. The modification of the band gap is hence due to both structural changes and insertion of external atoms, as reported by EDX analysis, but it is very complicated to find an unequivocal correlation between all the parameters involved. Due to time limitations, morphology and atoms ratio factors are not illustrated in band gap differences.

Chapter 6: Conclusion and future work

6.1 Conclusion

Several different approaches towards improving the performance of ZnO in photocatalysis under visible light were investigated in this research project. Specifically, the effects of complete or partial substitution of O by N and F were evaluated. Synthesis methods for the partial nitridation and non-metal doping of ZnO were developed, with descriptions of the synthesis pathways and optimisation of the synthetic methods produced by using a full set of characterisation techniques (PXRD, SEM, EDX, UV-vis spectroscopy, thermal analysis). In particular, attention was focused on the synthesis of Zn₂NF, in which oxygen is completely substituted by nitrogen and fluorine, in order to create an isoelectronic compound with a reduced band gap.

The synthesis of Zn₂NF requires a high purity Zn₃N₂ precursor, even higher than those available commercially (1% of impurities). Nitrides of transition metal with filled d-shells are less common and more difficult to produce compared with the nitrides of metal with almost empty d-shells, such as TiN. The synthesis of Zn₃N₂ powder was improved using a quenched cooling method, minimising the formation of ZnO impurities. Furthermore, the origin of ZnO impurities was identified after several experiments testing different synthesis conditions and parameters, such as reaction time, cooling atmosphere and rate, precursor purity. Among all these parameters, cooling rate was shown to have a major influence on the purity of the final product. ZnO forms when molten Zn powder starts to solidify, generating a relatively large amount of oxide phase in the final nitride, even if the reactants contain a low amount of initial impurities. Quenching the Zn powder at the end of the ammonolysis process, with the reacted material brought to room temperature in about 3-5

minutes, successfully reduced the formation of ZnO to almost neglectable levels.

Moreover, SEM analysis showed the formation of faceted crystallites for Zn_3N_2 indicating high crystallinity. Morphology appeared to concentrate with nitrogen content, with higher nitride levels associated with a more crystalline material. The calculation of the band gap of Zn_3N_2 gave a value of 2.96 eV.

Synthesis of Zn_2NF was performed using a stoichiometric 1:1 ratio of a powder mixture of previously produced Zn_3N_2 and commercial ZnF_2 . Different reaction conditions were investigated including temperature, reaction duration and atmosphere, targeting the production of pure Zn_2NF and its two different polymorphs. Only the high-temperature Zn_2NF tetragonal phase could be obtained from the reaction. Low-temperature Zn_2NF phase was not achieved under any of the conditions tested, despite previously reported synthetic protocols being followed. The Zn_2NF morphology is similar to the one observed for Zn_3N_2 resulting in smoothed and rounded-edge faceted crystallites.

A band gap of as 2.82 eV was measured for Zn_2NF , confirming the possibility of narrowing the band gap energy compared to the corresponding oxide (ZnO , 3.37 eV) and extending the absorption capacity of the material into the visible light region. However, no photocatalytic activity was observed in dye degradation test in aqueous solution, with poor dispersibility of the material and apparent instability of Zn_2NF in water.

Doping experiments on ZnO targeted the identification of intermediate structures between the non-oxide and Zn_2NF by partial replacement of oxygen atoms with nitrogen and fluorine. Different doping procedures resulted in a change of the material colour and detection by EDX analysis of the dopant elements while preserving the original crystal structure of ZnO despite the minimal presence of secondary phases. Reaction of Zn powder in the presence

of NH_4F at high temperature in a closed system under vacuum resulted in a higher amount of fluorine in the product. Repeated ammonolysis reaction with ZnF_2 resulted in significant nitrogen content in the end materials. The measurement of the optical properties showed a reduction of the band gap associated with N and/or F doping, with intermediate values between the band gap of ZnO (3.37 eV) and Zn_2NF (2.82 eV). According to the work herein, it was not possible to achieve a band gap lower than that of Zn_2NF , as reported elsewhere. ^[46]

6.2 Future work

The synthesis of an efficient visible-light active photocatalyst based on the full or partial substitution of oxygen atoms in ZnO represented the ultimate target of this project. However, the efficient modification of the optical properties did not correspond to resultant photoactivity of the materials. The main cause of this failure was in the instability of the nitride fluoride in the aqueous environment, with partial reaction to form ZnO occurring. Our findings are in contrast with the seminal work of Lingampalli et al., who efficiently utilised the same material to generate hydrogen by water splitting. However, the amount of pure material available for testing was limited by the scale of the synthesis procedure, with a maximum of 20 mg $\text{Zn}_3\text{N}_2 + \text{ZnF}_2$ being available for reaction. Scaling up or improving the experimental setup for the production of Zn_2NF is essential for a detailed study of its interaction with an aqueous environment and its photocatalytic properties.

Further research should also target other applications for zinc nitride fluorides, such as exploitation of anti-bacterial properties, already reported for fluorine-doped ZnO.^[76] Doping experiments were not fully completed due to the short time scale of the project. Targeting the precise composition of dopants in the material by controlling the stoichiometric ratio of the precursors and the synthetic conditions (atmosphere, temperature) is critical. The correlation between nitrogen and fluorine content and band gap in ZnO requires further investigation. The use of more accurate characterization techniques, such as X-ray Photoelectron Spectroscopy (XPS), would shed light on the precise composition of the products and how this composition might vary from surface to bulk. The structure morphology relationships (such as the hexagonal layered structure observed in liquid N₂ cooling of Zn₃N₂ could be investigated in more detail using TEM and selected area electron diffraction).

As a last potential improvement, despite successfully reducing the ZnO impurity resulting from Zn₃N₂, its total elimination would require a significant modification of the design of the reaction setup or the application of completely different synthetic routes.

Bibliography

1. Brese, N. E. & O'Keeffe, M. in *Complexes, Clusters and Crystal Chemistry* 307–378 (Springer Berlin Heidelberg, 1992).
2. Disalvo, F. J. & Clarke-f, S. J. Ternary nitrides : a rapidly growing class of new materials. 241–249 (1996).
3. Schnick, B. W. Solid-state Chemistry with Nonmetal Nitrides. *Angew. Chem. Int. Ed. Engl.* **32**, 806–818 (1993).
4. Gregory, D. H. & Gregory, D. H. Structural families in nitride chemistry. *J.Chem.Soc.* 259–270 (1999).
5. Brauer, V. E. Z. B. KONSTITUION DES LITHIUMNITRIDES. *Ztachr. Elektrochem.* **63**, 102–107 (1935).
6. Fischer, D. & Jansen, M. Synthesis and Structure of Na₃N. 1755–1756 (2002).
7. Tapia-ruiz, N., Segalés, M. & Gregory, D. H. *The chemistry of ternary and higher lithium nitrides. Coordination Chemistry Reviews* **257**, (Elsevier B.V., 2014).
8. Niewa, R. & Jacobs, H. Group V and VI Alkali Nitridometalates : A Growing Class of Compounds with Structures Related to Silicate Chemistry. *Chem. Rev.* **96**, 2053–2062 (1996).
9. Heyns, A. M. The Vibrational Spectra and Decomposition of α - Calcium Nitride (α -Ca₃N₂) and Magnesium Nitride (Mg₃N₂) The Vibrational Spectra and Decomposition of -Calcium Nitride (-Ca₃N₂) and Magnesium Nitride (Mg₃N₂). *J. Solid State Chem.* **137**, 33–41 (1998).
10. Skapski, A. C. The Crystal Structure. **7**, 5–9 (1968).
11. Hansen, N. A. K. & Herrmann, W. A. Controlled Thermolysis of Nitrido- and Imidomolybdenum Complexes : A New Route to Phase-Pure Molybdenum Nitrides. **4756**, 1677–1679 (1998).
12. Zhang, J. *et al.* Electrochimica Acta Conductive bridging effect of TiN nanoparticles on the electrochemical performance of TiN @ CNT-S composite cathode. *Electrochim. Acta* **250**, 159–166 (2017).
13. Hwang, T. & Kim, D. Physica C : Superconductivity and its applications Variation of superconducting transition temperature by proximity effect in NbN / FeN bilayers. *Phys. C Supercond. its Appl.* **540**, 16–19 (2017).
14. Guo, H. *et al.* Microstructure and properties of VN / Ag composite films with various silver content. **137**, (2017).
15. J.F. Brice, J.P. Motte, R. Streiff, C. R. Sur un nouveau composé dans la série des nitrites ternaires contenant du lithium: LiBeN, Préparation et propriétés. *Compte Rendus l'Academie Sci.* **C269**, 910 (1969).
16. Langer, K. R. J. Ternary Nitrides, Phosphides, and Arsenides of Lithium. *Angew. Chem. Int. Ed.* **7**, 360–370 (1968).

17. Gregory, D. H. Nitride chemistry of the s-block elements. **215**, 301–345 (2001).
18. MING Y. CHERN, D. A. VENNOS, F. J. D. Synthesis , Structure , and Properties of Anti-perovskite Nitrides CaZrM_2N_4 , $M = \text{Pb, As, Sb, Bi, Ge, Sn}$, and Pb . *J. Solid State Chem.* **96**, 415–425 (1992).
19. Elder, H.;Doerrler, L.H.;DiSalvo, F. J.; Parise, J.B.; Guymard, D.;Tarascon, J. M. LiMoN_2 : The First Metallic Layered Nitride. *Chem. Mater.* **4**, 928–937 (1992).
20. Marchand, R., Tessier, F. & Disalvo, F. J. New routes to transition metal nitrides : preparation and characterization of new phases. *J. Mater. Chem.* **9**, 297–304 (1999).
21. Ronald, k. Roland, W. Ternary Nitrides of Calcium and Strontium with Molybdenum and Tungsten. *Inorg. Chem.* **5**, 1849–1852 (1970).
22. Yang, M., Wang, Q., Lv, M. & Zhu, H. Journal of the European Ceramic Society Synthesis and sintering of silicon nitride nano-powders via sodium reduction in liquid ammonia. *J. Eur. Ceram. Soc.* **36**, 1899–1904 (2016).
23. Yao, S. & Su, L. The tribological potential of CrN and Cr (C , N) deposited by multi-arc PVD process. *Wear* **2**, 85–94 (1997).
24. Kojima, R. & Aika, K. Cobalt molybdenum bimetallic nitride catalysts for ammonia synthesis Part 1 . Preparation and characterization. *Appl. Catal. A* **215**, 149–160 (2001).
25. Moriya, Y., Takata, T. & Domen, K. Recent progress in the development of (oxy) nitride photocatalysts for water splitting under visible-light irradiation. *Coord. Chem. Rev.* **257**, 1957–1969 (2013).
26. Rizzo, A., Signore, M. A., Mirengi, L. & Dimaio, D. Deposition and properties of ZrN x films produced by radio frequency reactive magnetron sputtering. **515**, 1486–1493 (2006).
27. Nakamura, Shuji, and S. F. C. *Introduction to nitride semiconductor blue lasers and light emitting diodes.* (2000).
28. Kimura, C. *et al.* Field emission characteristics of BN / GaN structure Field emission characteristics of BN O GaN structure. **4533**, 1–4 (2013).
29. Reckeweg, O. & Disalvo, F. J. Alkaline earth metal nitride compounds with the composition $M_2\text{NX}$ ($M = \text{Ca, Sr, Ba}$; $X = \text{, H, Cl or Br}$). *Solid State Sci.* **4**, 575–584 (2002).
30. Andersson, S. Magnesium Nitride Fluorides. **309**, 306–309 (1970).
31. Nr, P. *et al.* Untersuchungen an Erdalkalimetall-Erdalkalimetallhalogenid-systemen. *Z. Chem* **2**, 3–4 (1962).
32. Bowman, A., Smith, R. I. & Gregory, D. H. Ternary and quaternary layered nitride halides , $\text{Ca}_2\text{N}(\text{X}, \text{XO}) (\text{X}, \text{XO} \frac{1}{2} \text{Cl, Br, I})$: Evolution of structure with composition. **178**, 1807–1817 (2005).
33. Seibel, H., and T. R. W. Preparation and crystal structure of Ba_2NF . *J. Solid State Chem.* **177**, 2772–2776 (2004).
34. Baj, N. *et al.* Uber die Systeme $\text{Ba}_2\text{N}_2/\text{BaCl}_2$, $\text{Ba}_3\text{N}_2/\text{BaBr}_2$, $\text{Ba}_2\text{N}_2/\text{BaI}_2$. *Z. Anorg. Allg. Chem.* **58**, 243 (1964).

35. Bailey, A. S. *et al.* New Ternary and Quaternary Barium Nitride Halides ; Synthesis and Crystal Chemistry. *Inorg. Chem.* **50**, 9545–9553 (2011).
36. Originalmitteilungen, K. & Natur-, D. Kurze Originalmitteilungen. *Die Natur-wissenschaften* **22**, 534–535 (1964).
37. P. Hartwig, W. Weppner, and W. W. FAST IONIC LITHIUM CONDUCTION IN SOLID LITHIUM NITRIDE CHLORIDE. *Mater. Res. Bull.* **14**, 493–498 (1979).
38. Ehrlich, Grant M., et al. New cerium nitride chlorides : *J. Alloys Compd.* **235**, 133–134 (1994).
39. Meyer, H. & Corbett, J. D. A New Yttrium Sesquichloride Nitride , @ -Y₂C₁₃N , That Is Isostructural with the Binary Yttrium Sesquichloride. *Inorg. Chem.* 2635–2637 (1989).
40. Hwu, S., Dudis, D. S. & Corbett, J. D. Synthesis, Structure, and Properties of the Infinite-Chain Compounds Sc₅C₁₈C and ScSCl₃N. *Inorg. Chem.* **26**, 1–5 (1987).
41. Schwanitz-schüller, U. & Simon, A. . Synthese und Kristallstruktur von Gd₂ NCl₃/Synthesis and Crystal Structure of Gd₂ NCl₃. *Zeitschrift für Naturforsch. B* **40**, 705–709 (1985).
42. Molybdannitridchlorid, D. K. Von & Joachim, V. Die Kristallstruktur von Molybdannitridchlorid, MoNCl₃. *Zeitschrift für Anorg. und Allg. Chemie* **375**, 238–254 (1970).
43. R. Juza und J. Heners. Über Nitridhalogenide des Titans und Zirkons. *Z. Anorg. Allg. Chem.* **332**, (1964).
44. R. Marchand, J. L. C. R. Sur la préparation d'halogénonitrides de zinc. *Seances Acad. Sci., Ser. C Sci. Chim.*, **270**, 540–542 (1970).
45. Liu, X., Wessel, C., Pan, F. & Dronskowski, R. Synthesis and Single-Crystal Structure Determination of the Zinc Nitride Halides Zn₂ NX (X = Cl , Br , I). *J. Solid State Chem.* **203**, 31–36 (2013).
46. Lingampalli, S. R., Manjunath, K., Shenoy, S., Waghmare, U. V. & Rao, C. N. R. Zn₂NF and Related Analogues of ZnO. *J. Am. Chem. Soc.* **138**, 8228–8234 (2016).
47. Liu, X., Wessel, C., Pan, F. & Dronskowski, R. Journal of Solid State Chemistry Synthesis and single-crystal structure determination of the zinc nitride halides Zn₂ N X (X ¼ Cl , Br , I). *J. Solid State Chem.* **203**, 31–36 (2013).
48. Kimball, G. M., Müller, A. M., Lewis, N. S. & Atwater, H. A. Photoluminescence-based measurements of the energy gap and diffusion length of Zn₃ P₂. *Appl. Phys. Lett.* **95**, 11–13 (2009).
49. Juza, R. & Hahn, H. Über die Kristallstrukturen von Zn₃N₂, Cd₃N₂ und Ge₃N₄. *Z. Anorg. Allg. Chem.* **244**, 125–132 (1940).
50. Wells, A. F. *Structural Inorganic Chemistry*. (Clarendon Press, 1984).
51. Partin, D. E., Williams, D. J. & Keeffe, M. O. The Crystal Structures of Mg₃ N₂ and Zn₃ N₂. **59**, 56–59 (1997).
52. Juza, R. & Hahn, H. Über die Nitride der Metalle der ersten Nebengruppen des periodischen Systems. *Z. Anorg. Allg. Chem.* **244**, 133–148 (1940).
53. Sakamoto, T., Sake, R., Moriga, T., Ichiro, K. E. I. & Nakabayashi, I. Characterizations of Zinc

- Oxynitride Powders Prepared Under Ammonia Gas Flow. *Int. J. Mod. Phys. B* **17**, 1523–1526 (2003).
54. Paniconi, G. *et al.* Synthesis, stoichiometry and thermal stability of Zn₃N₂ powders prepared by ammonolysis reactions. *J. Solid State Chem.* **181**, 158–165 (2008).
 55. Zong, F. *et al.* Synthesis and thermal stability of Zn₃N₂ powder. *Solid State Commun.* **132**, 521–525 (2004).
 56. Zong, F. *et al.* Structural properties of zinc nitride empty balls. *Mater. Lett.* **60**, 905–908 (2006).
 57. Khan, W. S. *et al.* Solvo-solid preparation of Zn₃N₂ hollow structures; Their PL yellow emission and hydrogen absorption characteristics. *Mater. Lett.* **65**, 2127–2129 (2011).
 58. Futsuhara, M., Yoshioka, K. & Takai, O. Structural, electrical and optical properties of zinc nitride thin films prepared by reactive rf magnetron sputtering. *Thin Solid Films* **322**, 274–281 (1998).
 59. Zou, C. W., Chen, R. Q. & Gao, W. The microstructures and the electrical and optical properties of ZnO:N films prepared by thermal oxidation of Zn₃N₂ precursor. *Solid State Commun.* **149**, 2085–2089 (2009).
 60. K.Kuriyama, Takahashi, Y. Optical band gap of Zn₃N₂ films. *Phys. Rev. B* **48**, 2781–2782 (1993).
 61. Zong, F. *et al.* Structural characterization of Zn₃N₂ nanowires prepared by nitridation technique. **59**, 2643–2646 (2005).
 62. Suda, T. & Kakishita, K. Band-gap energy and electron effective mass of polycrystalline Band-gap energy and electron effective mass of polycrystalline Zn₃N₂. **76101**, 1–4 (2016).
 63. Long, R., Dai, Y., Yu, L., Huang, B. & Han, S. Atomic geometry and electronic structure of defects in Zn₃N₂. **516**, 1297–1301 (2008).
 64. Li, Y., Liu, X. & Dronskowski, R. Synthesis and Structure Determination of the Quaternary Zinc Nitride Halides Zn₂NX_{1–y}X'_y (X, X' = Cl, Br, I; 0 < y < 1). *Inorganics* **4**, 29 (2016).
 65. Lan, R. M. J. & C, L. D. C. M. PREPARATION DE NOUVEAUX HALOGENONITRURES DE ZINC. *Mater. Res. Bull.* **6**, 845–852 (1971).
 66. Xu, H. Y. *et al.* F-doping effects on electrical and optical properties of ZnO nanocrystalline films. *Appl. Phys. Lett.* **86**, 1–3 (2005).
 67. Yang, X. *et al.* Nitrogen-doped ZnO nanowire arrays for photoelectrochemical water splitting. *Nano Lett.* **9**, 2331–2336 (2009).
 68. Qin, H., Li, W., Xia, Y. & He, T. Photocatalytic activity of heterostructures based on ZnO and N-doped ZnO. *ACS Appl. Mater. Interfaces* **3**, 3152–3156 (2011).
 69. Saha, R. *et al.* Remarkable properties of ZnO heavily substituted with nitrogen and fluorine, ZnO_{1–x}(N,F)_x. *ChemPhysChem* **14**, 2672–2677 (2013).
 70. Di, A., García-López, E., Marci, G. & Palmisano, L. A survey of photocatalytic materials for environmental remediation. *J. Hazard. Mater.* **211–212**, 3–29 (2012).

71. Pignatello, J. J. Evidence for a Surface Dual Hole- Radical Mechanism in the TiO₂ Photocatalytic Oxidation of. **29**, 2065–2072 (1995).
72. Fujishima A, H. K. Electrochemical photolysis of water at a semiconductor electrode. *Nature* **238**, 37 (1972).
73. Singh, J., Khan, S. A., Shah, J., Kotnala, R. K. & Mohapatra, S. Applied Surface Science Nanostructured TiO₂ thin films prepared by RF magnetron sputtering for photocatalytic applications. *Appl. Surf. Sci.* **422**, 953–961 (2017).
74. Shi, D. *Nanomaterials and Devices*. (Tsinghua University, 2015).
75. Marien, C. B. D., Cottineau, T., Robert, D. & Drogui, P. Applied Catalysis B : Environmental TiO₂ Nanotube arrays : Influence of tube length on the photocatalytic degradation of Paraquat. "*Applied Catal. B, Environ.* **194**, 1–6 (2016).
76. Podporska-Carroll, J. *et al.* Antibacterial properties of F-doped ZnO visible light photocatalyst. *J. Hazard. Mater.* **324**, 39–47 (2015).
77. Atkins, P. *Shriver and Atkins' Inorganic Chemistry*. (OUP Oxford, 2010).
78. H.M.Rietveld. Line profiles of neutron powder-diffraction peaks for structure refinement. *Acta Crystallogr.* **22**, 151 (1966).
79. Toby, B. H., Toby, B. H. & Toby, B. H. EXPGUI , a graphical user interface for GSAS EXPGUI , a graphical user interface for GSAS. 210–213 (2001).
80. Hafner, B. Scanning Electron Microscopy Primer. *Charact. Facil. Univ. Minnesota-Twin Cities* 1–29 (2015).
81. J.Tauc, R. Grigorovici, and A. V. Optical Properties and Electronic structure of Amorphous Germanium. *Phys. Status Solidi* **15**, 627 (1966).
82. V. Džimbeg-Malčić, Ž. Barbarić-Mikočević, K. No Title. *Itrić, Teh. Vjesn.* **18**, 117–124 (2011).
83. Wooten, F. *OPTICAL PROPERTIES*. (1972).
84. Xiong, Z. *et al.* Applied Catalysis B : Environmental Photocatalytic CO₂ reduction over V and W codoped TiO₂ catalyst in an internal-illuminated honeycomb photoreactor under simulated sunlight irradiation. "*Applied Catal. B, Environ.* **219**, 412–424 (2017).
85. Gallagher, P. K. *Handbook of thermal analysis and calorimetry*. (Elsevier Science B.V., 1998).
86. Khan, W. S. *et al.* Evolution of Zn based high purity phases under NH₃ gas atmosphere and their PL properties. *Appl. Surf. Sci.* **257**, 7314–7319 (2011).
87. Khan, W. S. & Cao, C. Synthesis, growth mechanism and optical characterization of zinc nitride hollow structures. *J. Cryst. Growth* **312**, 1838–1843 (2010).
88. Sutton, W. H. Microwave processing of ceramic materials. *Am.Ceram.Soc. Bull.* **68**, 376–386 (1989).
89. Liu, X. S. T. and L. L. Synthesis and Structural Characterization of Zn₃N₂ powder. *J. Chem. Pharm. Res.* **45**, 905–909 (2014).
90. Djebaili, K., Mekhalif, Z., Boumaza, A. & Djelloul, A. XPS , FTIR , EDX , and XRD Analysis of Al₂

- O 3 Scales Grown on PM2000 Alloy. **2015**, (2015).
91. Paniconi, G. Novel precursors for the synthesis of zinc nitride, copper nitride and nickel nitride. (University of Nottingham, 2011).
 92. Kaschner, A. *et al.* Nitrogen-related local vibrational modes in ZnO:N. *Appl. Phys. Lett.* **80**, 1909–1911 (2002).
 93. Núñez, C. G. *et al.* Sub-micron ZnO:N particles fabricated by low voltage electrical discharge lithography on Zn₃N₂ sputtered films. *Appl. Surf. Sci.* **285**, 783–788 (2013).
 94. Gonzalez-Hernandez, R. *et al.* Study of the properties of undoped and fluorine doped zinc oxide nanoparticles. *Mater. Lett.* **64**, 1493–1495 (2010).
 95. Lingampalli, S. R. & Rao, C. N. R. Remarkable improvement in visible-light induced hydrogen generation by ZnO/Pt/Cd_{1-y}Zn_yS heterostructures through substitution of N and F in ZnO. *J. Mater. Chem. A* **2**, 7702–7705 (2014).
 96. Harun, K., Mansor, N., Ahmad, Z. A. & Azmin, A. Electronic properties of ZnO nanoparticles synthesized by Sol- gel method : A LDA + U calculation and experimental study. *Procedia Chem.* **19**, 125–132 (2016).
 97. Jian-bang, W., Xin-lu, C., Hong, Z. & Zheng-wei, X. First-principles study of structural , electronic and optical properties of ZnF₂. **23**, 1–7 (2014).

Appendix

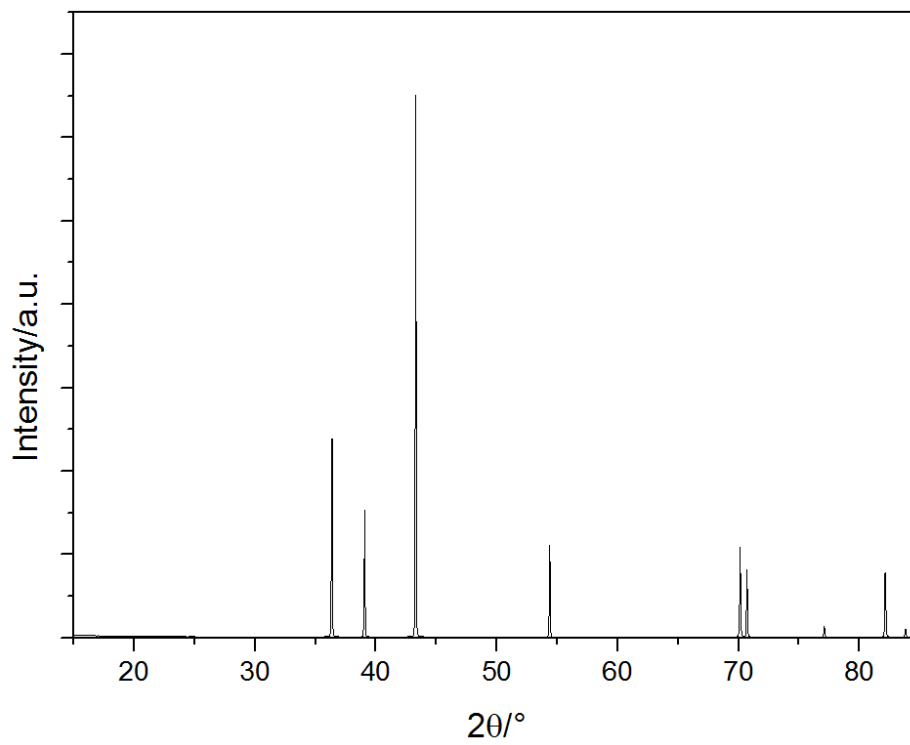


Figure 1: Zinc powder PXD pattern

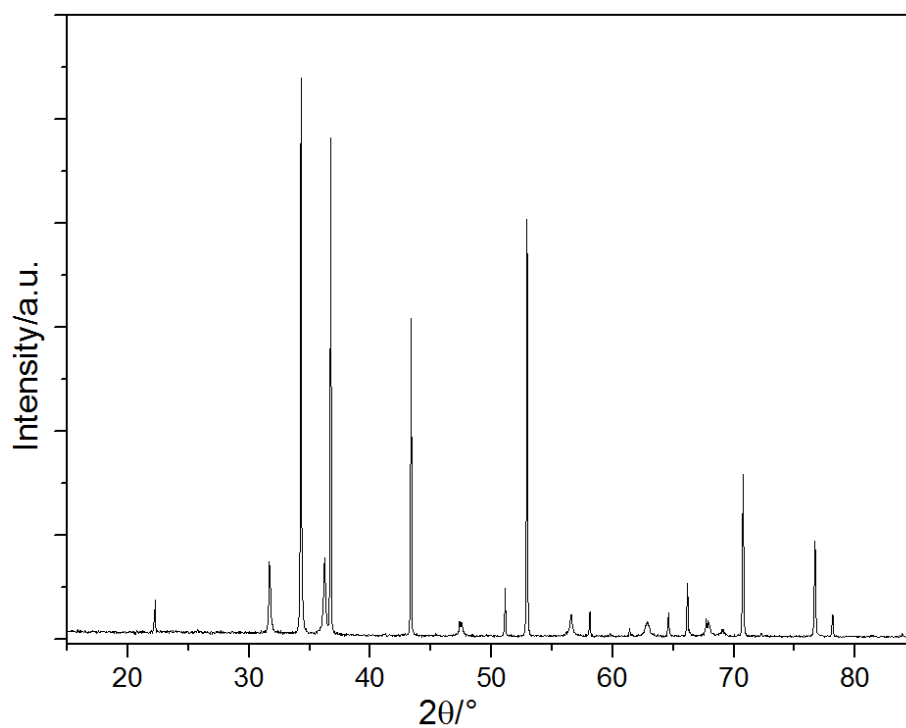


Figure 2: Zn₃N₂ powder synthesised with 5°C/min ramp under 600°C, 12 hours, Ar cooling.

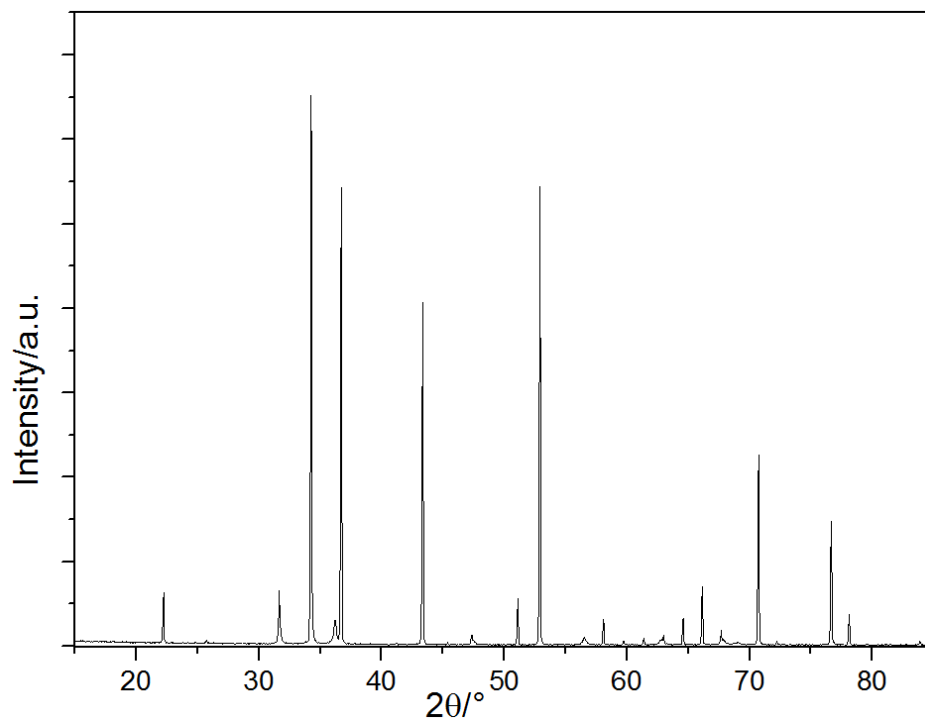


Figure 3: Zn₃N₂ powder synthesised under 600°C, 10 hours, cooling with Ar passed by molecular sieves

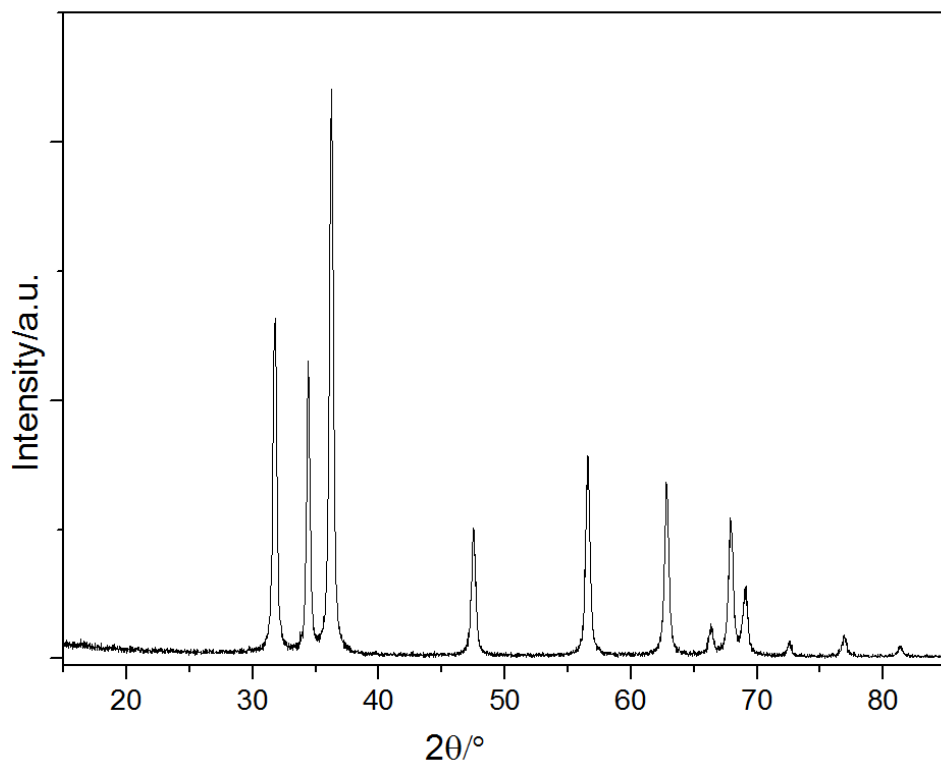


Figure 4: ZnO nanoparticles synthesised by sol-gel method for doping experiment

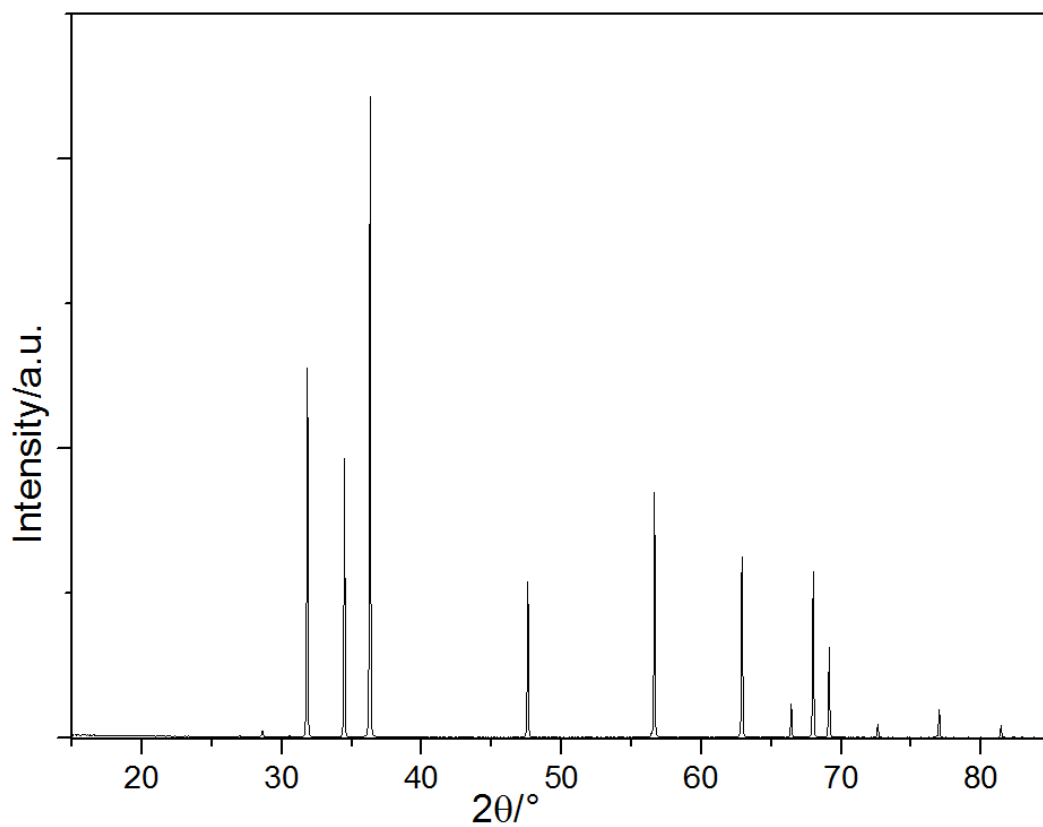


Figure 5: ZnO ammonolysis reaction product PXD pattern (under 600°C with 3 hours)

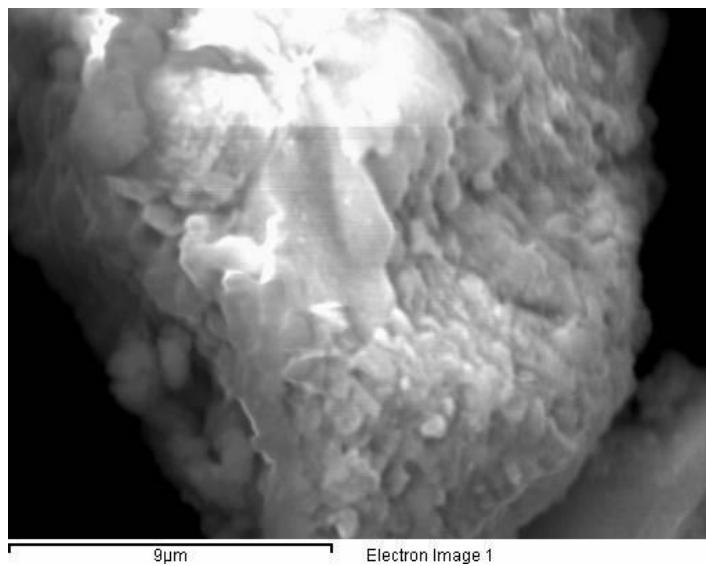


Figure 6: SEM image for ZnF₂ ammonolysis reaction 1st cycle product